Spring 5-15-2015

Polarization Sensor Design for Biomedical Applications

Timothy York
Washington University in St. Louis

WASHINGTON UNIVERSITY IN ST. LOUIS

School of Engineering and Applied Science
Department of Computer Science and Engineering

Dissertation Examination Committee:
Viktor Gruev, Chair
Shantanu Chakrabartty
Roger Chamberlain
Spencer Lake
Barani Raman
William Richard

Polarization Sensor Design for Biomedical Applications

by
Timothy York

A dissertation presented to the
Graduate School of Arts & Sciences
of Washington University in
partial fulfillment of the
requirements for the degree
of Doctor of Philosophy

May 2015
St. Louis, Missouri

Table of Contents

List of Figures

List of Tables

Acknowledgments

I would like to thank Viktor for all of his encouragement and guidance through my entire graduate career. He always had an answer for everything, especially things which caused me undue amounts of stress. The example he has set for how to be a researcher will be near impossible to replicate in my own career, but it is an example I will no less strive to achieve.

I would also like to thank my lab mates Raphael, Shengkui, Sam, Missael, Meenal, and Rado for the many fun times and great discussions in lab. Without their support, this would not have been possible. I would also like to thank the research collaborators whose expertise in their field helped broaden my own, and whose patience and excitement provided me with ample motivation to solve the many diverse problems we shared.

I would like to thank my committee for their time and patience, as well as the valuable feedback and comments. They have helped strengthen my body of work.

Finally, I would like to thank my family. My parents for valuing my education, and the full support they have given as I have pursued it. I thank my wife Christina, for her support and understanding during the whole of my graduate career and beyond.

Timothy York

Washington University in St. Louis

May 2015

ABSTRACT OF THE DISSERTATION

Polarization Sensor Design for Biomedical Applications

by

Timothy York

Doctor of Philosophy in Computer Engineering

Washington University in St. Louis, 2015

Professor Viktor Gruev, Chair

Advances in fabrication technology have enabled the development of compact, rigid polarization image sensors by integrating pixelated polarization filters with standard image sensing arrays. These compact sensors have the capability for allowing new applications across a variety of disciplines, however their design and use may be influenced by many factors. The underlying image sensor, the pixelated polarization filters, and the incident lighting conditions all directly impact how the sensor performs.

In this research endeavor, I illustrate how a complete understanding of these factors can lead to both new technologies and applications in polarization sensing. To investigate the performance of the underlying image sensor, I present a new CMOS image sensor architecture with a pixel capable of operation using either measured voltages or currents. I show a detailed noise analysis of both modes, and that, as designed, voltage mode operates with lower noise than current mode. Further, I integrated aluminum nanowires with this sensor post fabrication, realizing the design of a compact CMOS sensor with polarization sensitivity. I describe a full set of experiments designed as a benchmark to evaluate the performance of compact, integrated polarization sensors. I use these tests to evaluate for incident intensity, wavelength, focus, and polarization state, demonstrating the accuracy and limitations of polarization measurements with such a compact sensor. Using these as guides, I present two novel biomedical applications that rely on the compact, real-time nature of compact integrated polarimeters. I first demonstrate how

these sensors can be used to measure the dynamics of soft tissue in real-time, with no moving parts or complex optical alignment. I used a 2 megapixel integrated polarization sensor to measure the direction and strength of alignment in a bovine flexor tendon at over 20 frames per second, with results that match the current method of rotating polarizers. Secondly, I present a new technique for optical neural recording that uses intrinsic polarization reflectance and requires no fluorescent dyes or electrodes. Exposing the antennal lobe of the locust Schistocerca americana, I was able to measure a change in the polarization reflectance during the introduction of the odors hexanol and octanol with the integrated CMOS polarization sensor.

Chapter 1: Introduction

The path of digital polarization image sensors has seemed to mirror the path taken for digital color image sensors. Initial designs were based around time-multiplexed images captured with different optical filters. For color, these were red, green, and blue filters; for polarization these were different orientations of a linear polarizer. While time multiplexing proved effective for static scenes, it wasn't until color filters were integrated directly onto the image sensor array that digital color photography became ubiquitous [1]. High-resolution, compact color sensors have now found tremendous use in scientific and medical applications, enabling new discoveries because of their reliability and ease of use. Recent advances in nanofabrication techniques have allowed the development of similar, compact, integrated, high-resolution polarization sensors [2]. These *division-of-focal-plane polarization sensors* mate pixelated nanowire polarization filters designed for operation in the visible spectrum directly to an underlying image sensor. In the same vein as digital color sensors, these compact polarization sensors also have the potential to enable new discoveries in many diverse fields due to their rigid integration, reliability, and ease of use.

There are multiple considerations taken, however, when designing such polarimeters, perhaps none more important than the type of underlying image sensor used for capture. CCD image sensors have typically exemplified low noise combined with highly linear capture, and prove excellent candidates for scientific and industrial polarization sensors [3]. CCDs, however, typically have lower frame rates and higher power consumption than CMOS based image sensors. As new applications for integrated polarimeters develop, some of these applications may

require higher frame rates or lower power than CCDs can offer, thus necessitating a move towards CMOS based imaging arrays.

Even among CMOS arrays, a choice remains as to which architecture to use for pixel readout. Sampling the pixel value as a voltage is the most common choice of CMOS pixel architectures [4], [5]. Alternatively, the pixel value can be output as a current [6]. The optimality of either mode is subject to debate, with voltage mode purporting lower noise and higher linearity, while current mode potentially having higher speeds and lower power consumption. Direct comparison of the two modes has remained difficult, as many sensors use different fabrication processes, pixel architectures, and readout structures. Developing a sensor capable of operation in either mode, at the flip of a switch would allow for a direct comparison of the advantages and disadvantages of either. To date, such design has not been realized leaving out a fair comparison between these two imaging sensor modalities.

The recent development of compact, integrated polarimeters also leads to the challenge of how to accurately assess such a sensor's performance. The direct integration of the filters with pixels requires understanding of both the optical performance of the filters combined with the electrical properties of the sensor. The performance of the filters may be limited by wavelength, integration alignment, nanowire grating construction, and incident viewing angle [7], [8]. The underlying image sensor itself will have hard limits set by the SNR at various light intensities, as well as the dynamic range and quantum efficiency of the photosensitive element [3]. A full systematic testing methodology is needed to help comprehend all of these limitations and their impact on the sensor's polarization accuracy. Such a methodology can even potentially serve as a standard for evaluation of these types of sensors.

A thorough characterization of the sensor's electrical and optical performance can also help guide the design of applications of the sensor's use. Understanding the limitations of the sensor guides choosing the correct optics for a particular application, from incident illumination sources, to lenses, to any additional filters needed in the input or output path. Can we develop new applications that take advantage of the compact, rigid nature of the polarization sensor?

In this dissertation I propose to address the following questions:

1. Can we directly and fairly evaluate the advantages and disadvantages of CMOS voltage mode and current mode sensors?
2. Can we design, fabricate and test a compact, integrated, division-of-focal-plane CMOS polarization sensor?
3. Can we develop a systematic testing methodology for division-of-focal-plane polarimeters to evaluate their optical and electrical performance?
4. Can we use division-of-focal-plane polarimeters to solve biomedical research problems where real-time acquisition of polarimeteric information is critical?

1.2 Contributions of this Dissertation

To answer the above questions,

1) I have fabricated a custom CMOS image sensor that can operate in either voltage or current mode. I fabricated the sensor a 180-nanometer CMOS process specifically optimized for image sensors. I have evaluated the noise equations of the sensor in both modes, and I have tested the fabricated sensor for operation in current mode and voltage mode. A theoretical model has been developed to capture the various noise contributions in either imaging modality and is in a good agreement with experimental data.

2) I have realized the first CMOS polarization imaging sensor by depositing pixel-pitch matched, aluminum nanowire polarization filters on an array of imaging elements using flip chip bonding technique.

   I have developed a systematic method for evaluating the optoelectronic performance of the CMOS polarization sensor operating in the current mode domain. The test bench evaluates the performance of the polarization sensor over a large space including: incident illumination intensity, degree of polarization, angle of polarization, wavelength evaluation, and optical divergence.

3) The first CMOS polarization imaging sensor has enabled the following novel biomedical applications:

   a. Measure for the first time the real-time dynamics of soft tissue using standard optics without requiring the use of rotating polarization elements

   b. Optically record neural activity using the intrinsic polarization reflectance without the use of any fluorescent probes or contact electrodes

1.3 Organization of the Dissertation

The dissertation is organized as follows: Chapter 2 provides the details of the dual mode CMOS image sensor. It includes the full schematic of the pixel and readout structure, as well as a noise analysis with simulations, and finally measurements from the fabricated chip. Chapter 3 gives a background on polarization image sensor architectures, as well as the physics of how light is polarized. It then includes measurements of the CMOS image sensor fabricated in Chapter 2 operating in current mode. Chapter 4 contains a complete measurement methodology for division-of-focal-plane polarimeters. The sensor is a CCD division-of-focal-plane polarimeter which underwent multiple optical tests to evaluate the polarization accuracy for various

intensities, wavelengths, and incident optical angles. Chapter 5 contains two biomedical applications using division-of-focal-plane polarimeters. The first uses a CCD division-of-focal-plane polarimeter to measure the strength of alignment of dynamically loaded tissue in real-time. The second application uses the CMOS current mode image sensor to observe the intrinsic optical polarization change during neural activation in a locust.

Chapter 2: Dual-Mode CMOS Imager: Current vs. Voltage Mode Imaging

2.1 Overview of Voltage and Current Mode Image Sensors

The inception of MOS imaging sensors can be traced back to the late 1960's, when the first 10 by 10 imaging array was reported in the literature [9]. The pixel's schematic in this groundbreaking work was composed of five transistors: two reset transistors and two address transistors for individually resetting and accessing pixels in the 2-D array respectively. The fifth transistor was utilized as a source follower and buffered the integrated photodiode voltage on an output bus. Due to the large voltage threshold variations in the source follower as well as the large dark currents, the quality of the captured images was poor. In order to improve the image quality, double sampling was introduced as well huge effort into improving the fabrication process of CMOS circuits.

The basic pixel circuitry of today's imaging sensor has not changed for more than 50 years. Cellphone manufactures are the leading force in miniaturizing the pixel size down to ~$1\mu m^2$ primarily due to the benefits of Moore's law – as the transistors sizes decrease with smaller feature technology, the pixel pitch in imaging sensors decreases as well. The challenges for imaging sensors fabricated in small feature technologies are maintaining high sensitivity and low noise performance. Some of these challenges are mitigated by optimizing the fabrication steps of the photodiodes, which are becoming very complex in order to preserve sensitivity, high quantum efficiency and high pixel well depth [10].

Current mode imagers have been widely recognized as computational sensors [11]–[13]. The pixel in a current mode imager provides a current proportional to the incident light flux on

the pixel and due to Kirchhoff current law and current mirrors simple arithmetic operations such as addition, subtraction, multiplication and division are implemented with little or no power consumption. Another niche for current mode imagers is higher frame rates compared to voltage mode imaging sensor. Due to the fact that the read-out buses in a current mode imager are kept at constant voltages while only currents are varied along the bus, higher frame rate can be achieved compared to voltage mode sensors due to minimized charging and discharging of the readout bus [14].

One of the shortcomings in current mode imagers has been higher spatial and temporal noise compared to voltage mode imagers. Many research efforts have been focused on reducing the spatial and temporal noise in current mode imaging sensors [6], [14]. Although the noise performance of current imagers has drastically improved over the last five years, drawing a fair comparison against the noise performance in voltage imagers has been difficult to do. The main reasons has been that voltage mode imagers are fabricated in CMOS process optimized for imaging sensors – they enjoy the benefits of double well process which allows for isolation of digital and analog circuits, pinned photodiode for CDS implementation and low noise read-out transistors with channel doping in order to push the channel formation away from the Si-SiO2 interface. In this technology the photodiode coupled with a charge transfer transistor and read-out transistor are carefully designed in order to: 1) have a complete charge transfer between the photodiode and the floating diffusion node and 2) maximize the capacitance on the floating diffusion node [15]. Since current mode imaging sensors have been implemented in a regular CMOS process, the noise performance will always be lower compared to voltage mode imager implemented in a CMOS imager optimized process.

In this chapter, we have designed a pixel that can operate in both current or voltage mode and will allow for a fair comparison between the spatial and temporal noise performance of voltage and current mode imagers. The pixel is implemented in 180nm CMOS process for imaging sensors (CIS). The pixel's charge transfer transistor and read-out transistor are optimized for full charge transfer and low noise on the read-out transistor by pushing the channel formation away from the Si-SiO2 interface and optimizing the pixels layout.

2.2 Dual Mode Sensor Design

The pixel contains four transistors that enable dual mode operation. Transistor M1 is for charge transfer, M2 is the readout transistor, M3 is a switch to reset the photodiode, and M4 is the column selector. The power bus connects to analog multiplexers to choose among V_{dd}, ground, or another preset voltage. The pixels share a row-parallel output bus.

2.2.1 Current Mode Operation

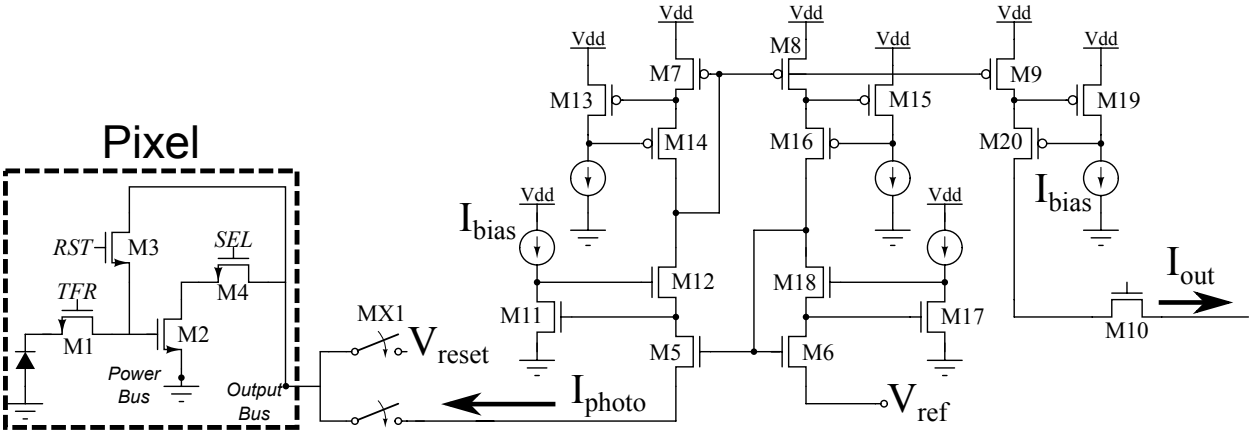

Figure 2.1: Current Mode Schematic

Operation in current mode takes place according to Figure 2.1. The M1 switch is connected to ground through analog multiplexer MX1. The pixel is reset by connecting the Output Bus to either V_{dd} or to another reset voltage at least one threshold below the supply through the analog multiplexer. With M3 turned on, the floating diffusion node, common for

transistors M1, M2, and M3 is pulled to this voltage, while the charge transfer, M1, is active. To enable readout, the floating diffusion is reset, while the output bus is pre-charged to a voltage equal to the reference voltage set on the current conveyor. The photovoltage is then transferred to the floating diffusion via M1 transistor, followed by turning off transistor M1. If the reference voltage present on V_{ds} is low enough, transistor M2 operates in the triode region, and the output current is linear with respect to the photovoltage. The row is then sampled one pixel at a time, after which the pixel is reset, and readout proceeds to the next column. On the periphery, the bus is connected to a current conveyor designed using a regulated cascode structure. The constant bias current fixes V_{ds} on the mirroring transistors in the conveyor, drastically reducing channel length modulation. Hence, the mirrored current flowing through transistors M8 and M9 has minimal error compared to the current flowing through transistor M13.

2.2.2 Voltage Mode Operation

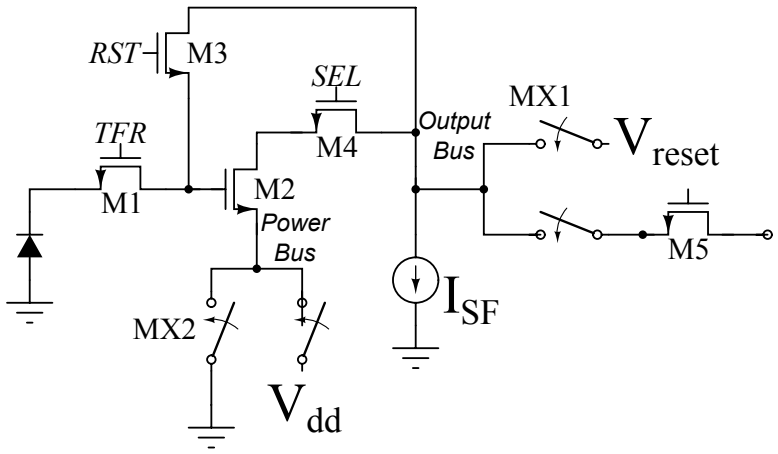

Figure 2.2: Voltage Mode Readout

Operation in voltage mode takes place according to Figure 2.2. To reset the pixel, the power bus connects to ground using analog multiplexer MX2, while the output bus connects to the reset voltage through M3. A low *RST* turns off M3 to complete the reset of the floating diffusion, after which the power bus connects to V_{dd}, and the output bus connects to a bias

current. M1 then transfers the photovoltage to the floating diffusion node, after which it turns off while the row is read out. The output bus is once again connects to the reset voltage, and M1 then turns on to reset the photodiode. Finally, M2 turns off, and readout proceeds to the next column.

The doping of M1 is tightly controlled, as well as the layout of the pixel, to allow complete charge transfer from the photodiode to the floating diffusion node, while the floating diffusion itself is optimized to reduce leakage currents. The pixel's layout was designed using Cadence Virtuoso tools and Taurus Medici simulation tools from Synopsys to ensure complete charge transfer. This allows the floating diffusion to be used essentially as a memory, holding the photovoltage until that row can be read. The floating diffusion is weakly photosensitive, as discharge of the photodiode results in a positive bias of the TFR signal with respect to the photovoltage. This, in turn, limits the capability of charge storage on the floating diffusion, as rows read later will have some voltage decay.

To test the charge storage capabilities on the FD node, the floating diffusion and pixel are driven to the reset potential, V_{reset}. M1 is then turned off to allow integration, and *Signal* is connected to the output bus. After a delay, M1 transfers the photovoltage to the floating diffusion, which is held for another delay before the pixel is reset. Changing the light intensity illustrates that the floating diffusion is light sensitive, with a different rate of change for different intensities. The decrease in voltage happens more rapidly as light intensity increases, however it shows little dependence on the reset voltage. In terms of error, with a reset voltage of 3.3 V, the worst case change is -5 mV/ms, which results in an error of only 0.3 %

2.3 Noise Analysis

Understanding the contributions of noise for both operations in current and voltage mode are key to determining the advantages or disadvantages of one mode over the other. Finding approximate solutions of the input referred noise during reset and readout will aid in determining the dominant sources, and guide the design of both the pixel and readout to minimize the noise contributions of either mode.

2.3.1 Noise During Reset

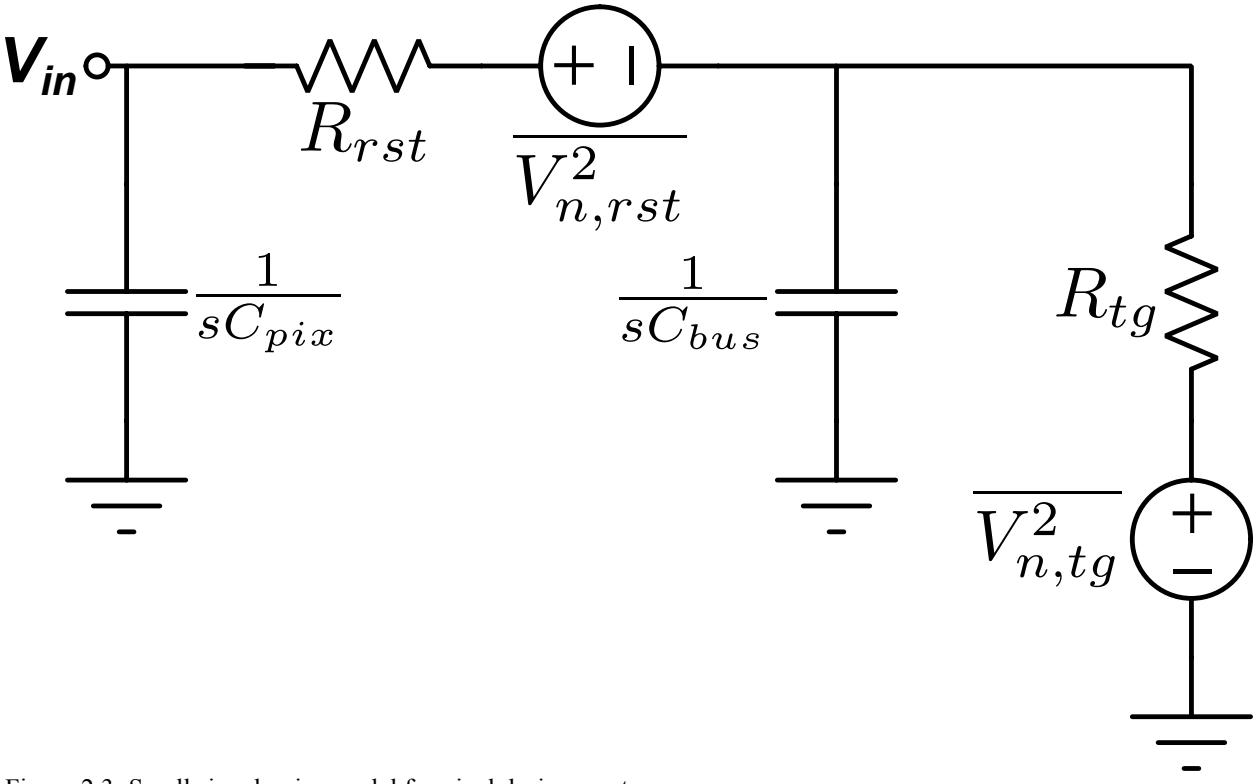

Figure 2.3: Small signal noise model for pixel during reset

In the Dual Mode pixel, shown in Figure 2.1, the reset noise is contributed by the on resistance of the PMOS transmission gate MUX transistor, R_{tg}, and the on resistance of the reset transistor, R_{rst}. There are two capacitances, C_{pix}, which is the combined capacitance of the photodiode and floating diffusion (the transfer transistor is specially designed to allow for

complete charge transfer, and thus is assumed to contribute no noise during reset), and C_{bus}, which is the bus capacitance shared by all pixels in the row. The equivalent circuit is shown in Figure 2.3. To solve for the noise contribution during reset, the sources are assumed to be uncorrelated, and thus the total noise contribution from each source during reset is computed from equation (2.1), where N is the total number of noise sources, and H is the transfer function for v_{in} over the ith source, with all others turned off

$$S_{out}(f) = \sum_{i=0}^{N} S_i(f)\left|H_i(f)\right|^2 \qquad (2.1)$$

Using (2.1) to compute the PSD and integrating the frequency from 0 to infinity, the approximate noise power during reset is then which is similar to the case of a 3T pixel [16],

$$\overline{V_{n,rst}^2} \approx \sqrt{\pi}\frac{kT}{C_{pix}} \qquad (2.2)$$

however having to include the analog multiplexer does increase the reset noise due to the additional internal resistance of the transmission gates.

2.3.2 Noise During Readout – Current Mode

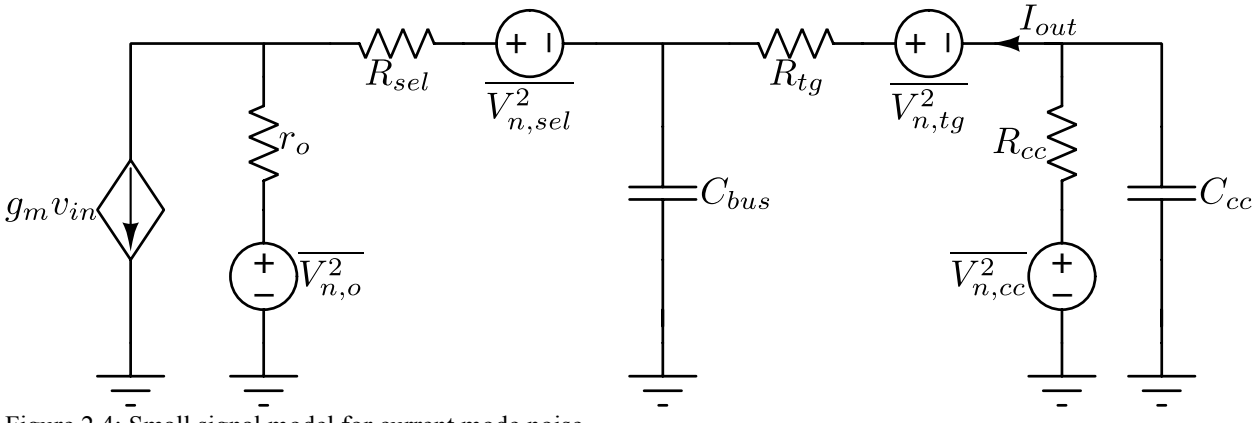

Figure 2.4: Small signal model for current mode noise

Figure 2.4 shows the small signal equivalent circuit of the current mode readout. The current conveyor is approximated as a single pole system comprised of a resistance, R_{cc}, and capacitance C_{cc}. Solving for the input referred noise requires a two-step process, as illustrated in [14], where first the transfer function of the input voltage over the output current is computed using the noiseless small signal model. Next, the contribution of each noise source from the small signal models is referred to the output, using superposition to compute the entire output referred noise. The total output noise is then referred back to the input via the noiseless transfer function. Doing so gives the input referred noise voltage during current mode readout, shown in (2.3).

$$\overline{V}_{in,current}^2 = \frac{\dfrac{4kT\left(r_o + R_{sel} + R_{cc}\right)}{\left(g_m r_o\right)^2} f_d + \dfrac{16\pi^2 kTR_{cc}\left(r_o + R_{sel}\right)^2\left(C_{bus} + C_{cc}\right)^2}{\left(g_m r_o\right)^2}\dfrac{f_d^3}{3}}{} \qquad (2.3)$$

2.3.3 Noise During Readout – Voltage Mode

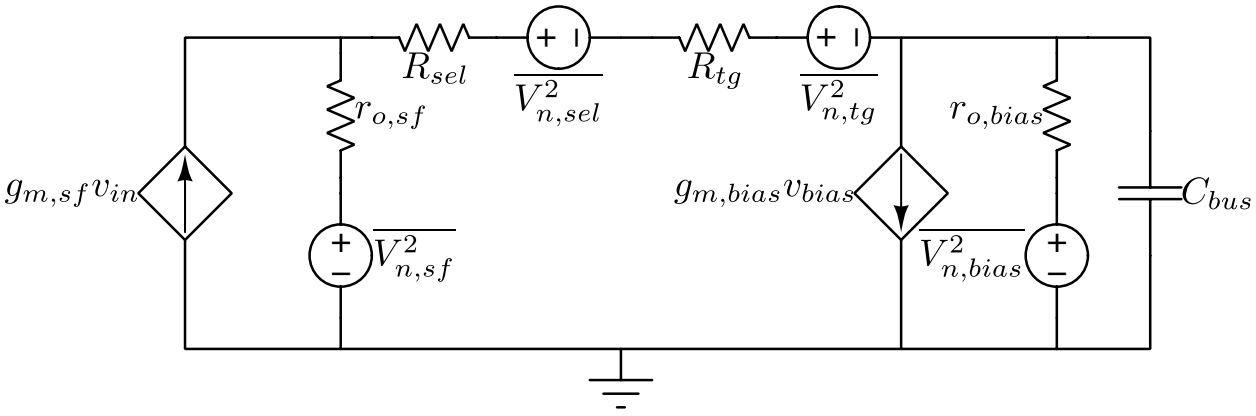

Figure 2.5: Small signal model of voltage mode readout

Figure 2.5 shows the small signal model for voltage mode readout. The noise during readout for voltage mode is derived from the readout source follower, select transistor, and the

biasing current source. Both the readout and biasing source operate in saturation, and thus the PSD of their noise currents is $4kT(2/3)g_m$. The select switch operates in linear mode, and thus the PSD of its noise current is $4kT/R_{on}$. Using an analysis similar to [16], the input referred noise of the readout in voltage mode is computed in (2.4).

$$\overline{V}_{in,voltage}^2 = \left[\begin{array}{c} \dfrac{8kT}{3g_m} + \dfrac{4kTR_{sel}}{(g_m r_o)^2} \\ + \dfrac{8kT}{3} \dfrac{g_{m,bias}(r_o + R_{sel})^2}{(g_m r_o)^2} \end{array} \right] f_d \qquad (2.4)$$

2.4 Simulations and Measurements from the Fabricated Sensor

Equations (2.3) & (2.4) show the output noise of the circuit in dual mode is inversely proportional to the intrinsic gain of the readout source follower, indicating that a readout with higher gain and output resistance would reduce the overall readout noise in the voltage mode.

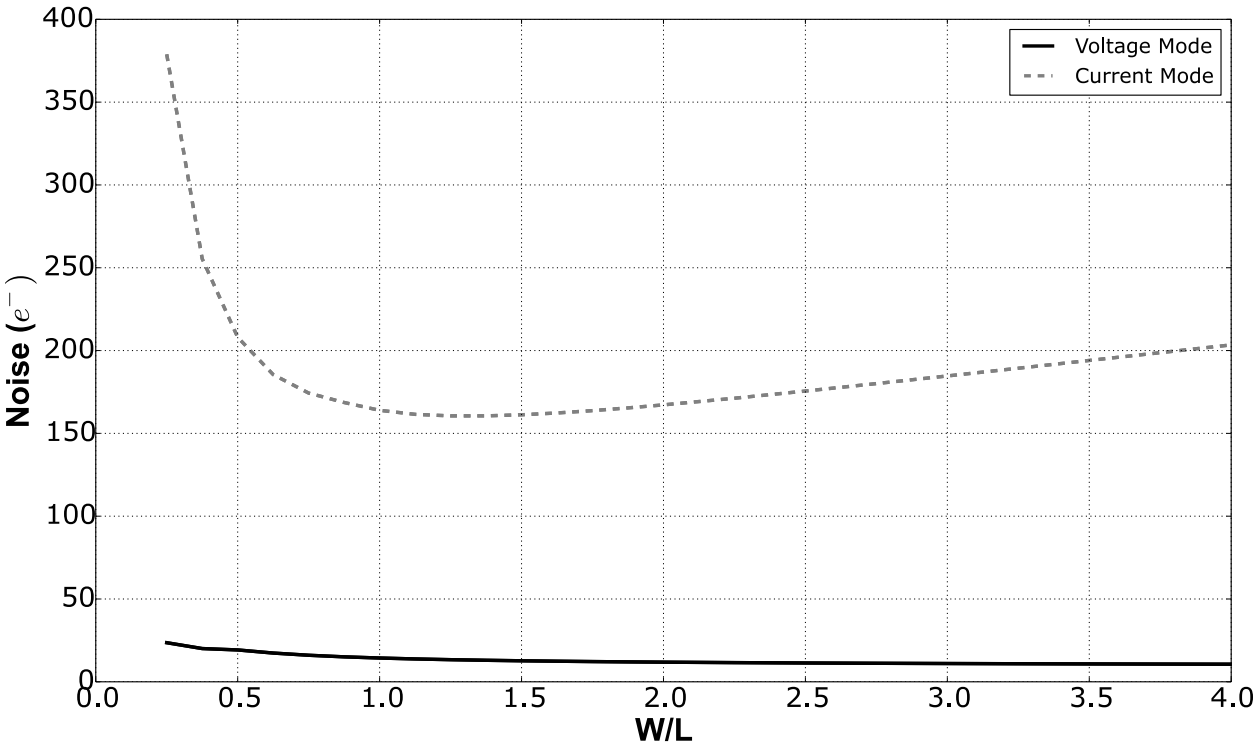

Figure 2.6: Readout noise as a function of aspect ratio

To evaluate this effect, noise simulations using Spectre were run for both the current and voltage mode readout circuitry from Section 2.1. The simulations show this is indeed the case with voltage mode, as Figure 2.6 indicates increasing the aspect ratio decreases the readout noise, as the larger aspect ratio increases the intrinsic gain of the readout transistor. This is not the case with current mode noise. While the noise in current mode sensors is a function of the intrinsic gain, the readout also operates in linear mode instead of saturation. This causes the formation of an optimal point in sizing the readout transistor of a current mode sensor. Using too low of an aspect ratio causes a decrease in the transconductance of the readout, resulting in an increase in noise. Increasing the aspect ratio increases the transconductance, however it also decreases the on resistance with the readout transistor operating in linear mode. From (2.3), this decreased on resistance will increase the readout noise.

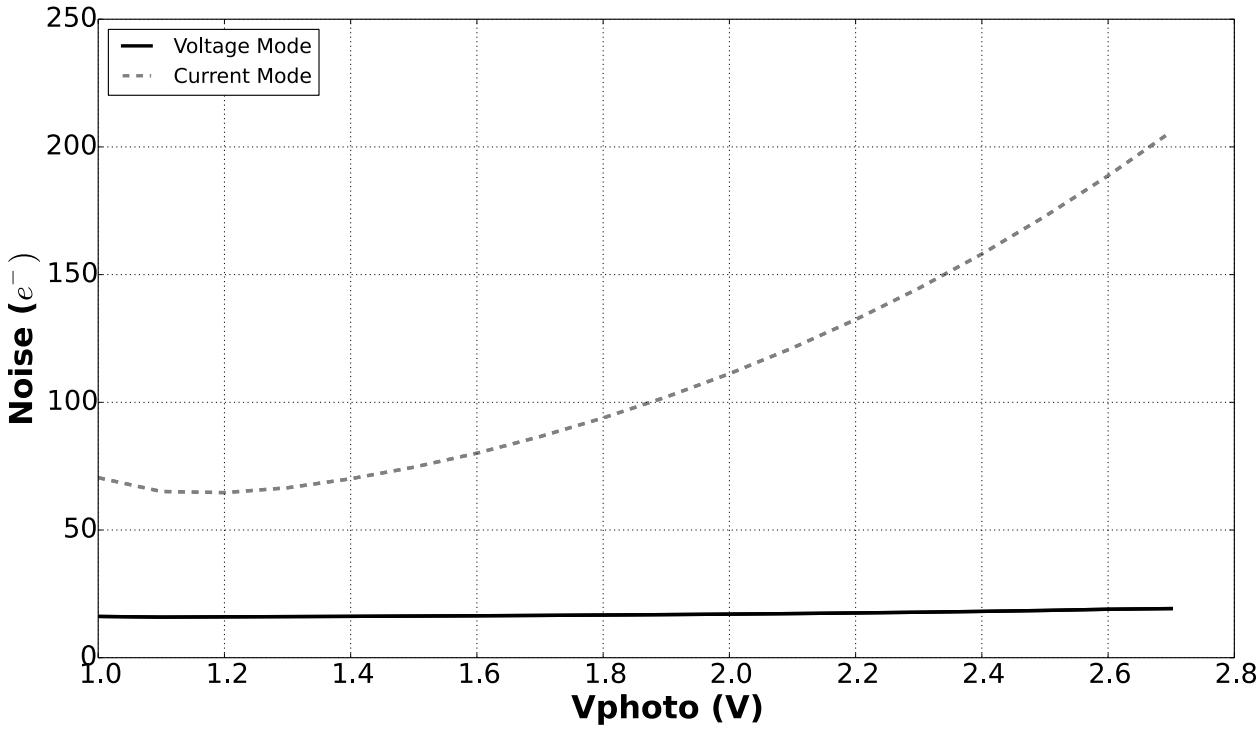

Figure 2.7: Readout noise as a function of the photovoltage

Figure 2.7 presents simulated noise from the imager. It shows the readout noise in current mode also depends on the input photovoltage, whereas voltage mode is relatively constant. This is due to the fact that gm is not constant when a transistor operates in linear mode, and thus the noise becomes a function of the input photovoltage. In both simulations, the input referred readout noise is nearly an order of magnitude higher for current mode than voltage mode. This is potentially due to the fact that the frequency response of the current conveyor introduces higher order noise components, emphasizing the importance of designing a low noise current conveyor.

Measurements were taken with the fabricated sensor. Figure 2.8 shows the measured signal-to-noise ratio of the sensor operating in both voltage and current mode. The voltage mode SNR is indeed always higher than the current mode SNR. This is expected from both the noise analysis and simulations, and seems to confirm that in terms of temporal noise, voltage mode does perform better than current mode. In terms of fixed-pattern-noise, measurements from the

sensor indicate that current mode has a lower uncompensated FPN at 0.9% compared to 4.8% for voltage mode.

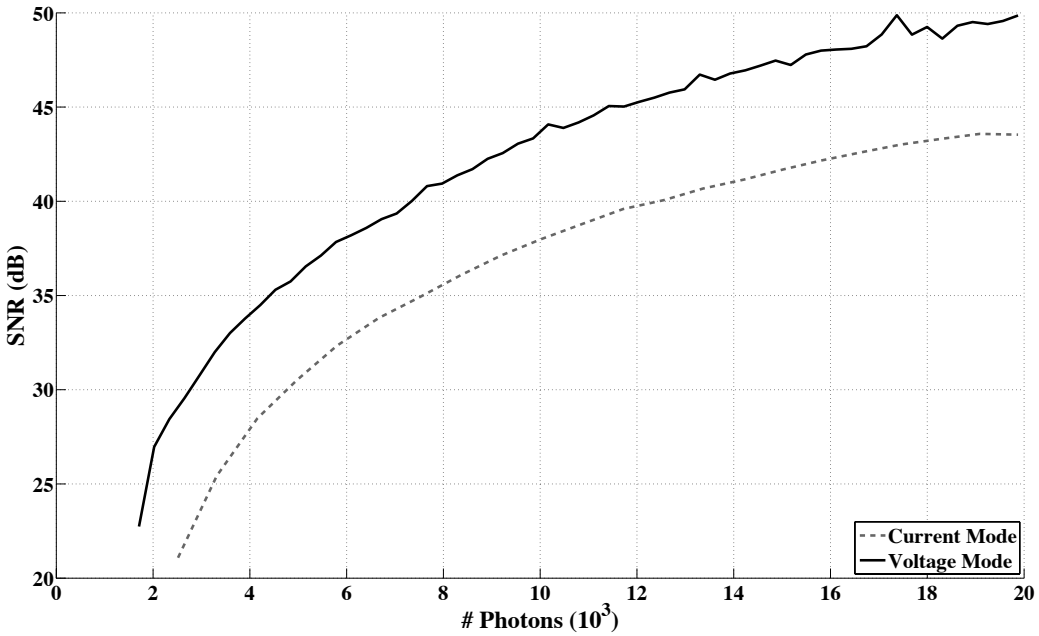

Figure 2.8: Measured SNR from the dual-mode image sensor

2.5 Conclusion/Discussion

The debate over the comparative advantages of voltage or current mode image sensors is ongoing. In an attempt to resolve some aspects of this debate, we have presented an image sensor capable of operating in both modes. We have shown through a thorough analysis equations for the noise introduced during reset and readout for both modes. We have further complemented the analysis with simulations that confirm that voltage mode does indeed have lower temporal noise than current mode. Finally, we have attempted to verify the simulations with measurements taken from a dual-mode image sensor fabricated in a 180 nm CMOS Image Sensor process. These initial measurements confirm that voltage mode has a lower SNR than current mode over the operating range.

Chapter 3: CMOS Polarization Image Sensor[11]

The design of division-of-focal-plane polarimeters necessitates an understanding of the fundamentals of polarization. This includes how light is polarized in the environment, how it is mathematically modeled, and how to measure the polarization state of light. In terms of measurement, taking hints from biological evolution shows that integration of polarizers directly to the photosensitive element results in a robust, compact design. This chapter presents a compact, division-of-focal-plane polarimeter based on this idea. The sensor integrates aluminum nanowire polarization filters with a custom designed CMOS current mode image sensor. Measurements from the fabricated sensor are included.

3.1 Theory of Polarization

Polarization is a fundamental property of electromagnetic waves. It describes the phase difference between the *x* and *y* components of the electromagnetic field when it is viewed as a propagating plane wave:

$$\mathbf{E} = E_{0,x}\cos\left(\omega t - kz + \delta_x\right)\hat{\mathbf{x}} + E_{0,y}\cos\left(\omega t - kz + \delta_y\right)\hat{\mathbf{y}} \quad (3.1)$$

where $E_{0,x}$ and $E_{0,y}$ are the respective amplitudes of the *x* and *y* fields, ω is the frequency, *t* is the time, *k* is the wavenumber, *z* is the direction of propagation, and δ_x and δ_y are the respective phases.

From (3.1), the type of polarization is characterized from $\delta_x - \delta_y$, because the difference in the phases is what shapes the wavefront of the propagating waves. If the phase difference is random, the light is *unpolarized*; if the phases are the same, the light is *linearly polarized*; if the phases are unequal but constant, the light is *elliptically polarized*. A special case of elliptical

polarization is observed when the phase difference is exactly $\pi/2$, which transforms the wavefront into a circle, and so the propagating light is termed *circularly polarized*. Most of the light waves encountered in nature are *partially polarized*, a linear combination of unpolarized light waves and completely polarized light waves.

3.1.1 A Mathematical Treatment of Light Properties via the Stokes-Mueller Formalism

The classic treatment of incoherent polarized light uses the Stokes-Mueller formalism [17]. The mathematical framework for polarized light is derived mostly from the seminal work by Sir Gabriel Stokes. From his work, the intensity of light measured through a linear polarizer at angle θ and a phase retarder, ϕ, can be mathematically represented by as

$$I(\theta,\phi) = \frac{1}{2}\left(S_0 + S_1\cos 2\theta + S_2 \sin 2\theta \cos\phi + S_3 \sin 2\theta \sin\phi\right) \qquad (3.2)$$

The terms S_0 through S_3 are called the *Stokes parameters*, and each describes a polarization property of the light wave. The S_0 parameter describes the total intensity; S_1 describes how much of the light is polarized in the vertical or horizontal direction; S_2 describes how much of the light is polarized at ±45° to the x/y-axis along the direction of propagation; and S_3 describes the circular polarization properties of the light wave. The Stokes parameters are commonly expressed as a vector, which relates these parameters to the electromagnetic wave equation (3.1):

$$\begin{bmatrix} S_0 \\ S_1 \\ S_2 \\ S_3 \end{bmatrix} = \begin{bmatrix} E_{0,x}^2 + E_{0,y}^2 \\ E_{0,x}^2 - E_{0,y}^2 \\ 2E_{0,x}E_{0,y}\cos\delta \\ 2E_{0,x}E_{0,y}\sin\delta \end{bmatrix} \qquad (3.3)$$

In equation (3.3), δ is the phase difference between the two orthogonal components of the light wave, $\delta_x - \delta_y$.

Treating the Stokes parameters as a vector allows for the easy superposition of many incident incoherent beams of light, which allows for an elegant mathematical treatment of light properties, ranging from unpolarized to partially polarized and completely polarized light. This is achieved by expressing the light as the weighted summation of a fully polarized signal and a completely unpolarized signal. Furthermore, Mueller matrices can be used to model the change in polarization from interaction with optical elements (reflection, refraction, or scattering) during light propagation in a medium, such as lenses, filters, or biological tissue [18]. A Mueller matrix is a 4-by-4 real-valued matrix that mathematically represents how an optical element changes the polarization of light. The change in polarization is computed from the matrix-vector product of an incident Stokes vector, **S**, with the matrix for a component **M**.

Two additional parameters are typically computed from the four-element Stokes vector. The first parameter is the degree of polarization (DoP), which estimates how much of the light is polarized. The DoP is computed from (3.4a) and is measured on a scale from 0 to 1, with 0 being completely unpolarized and 1 being completely polarized. The DoP can be further expressed in two components, the degree of linear polarization (DoLP) and the degree of circular polarization (DoCP). The DoLP (3.4b) measures how linearly polarized the light is, with 0 being no linear polarization and 1 being completely linearly polarized. Similarly, the DoCP (3.4c) measures how circularly polarized the light is, with 0 being no circular polarization and 1 being completely circularly polarized.

$$DoP = \frac{\sqrt{S_1^2 + S_2^2 + S_3^2}}{S_0} \quad (3.4a)$$

$$DoLP = \frac{\sqrt{S_1^2 + S_2^2}}{S_0} \quad (3.4b)$$

$$DoCP = \frac{S_3}{S_0} \quad (3.4c)$$

The second metric is the angle of polarization (AoP), which gives the orientation of the polarization wavefront. This is the angle of the plane that the light wave describes as it propagates in space and time and is computed as

$$AoP = \frac{1}{2}\tan^{-1}\left(\frac{S_2}{S_1}\right). \quad (3.5)$$

3.1.2 Polarization of Light Through Reflection and Refraction

Because polarization is a fundamental property of light, many organisms have evolved the capability to detect it in the natural world. To understand how this capability is useful, it helps to understand how light becomes polarized. In nature, light becomes polarized usually through reflectance or refractance of light off of an object, or through scattering as it encounters particles as it propagates through space. The DoP of the emerging light wave, after interacting with a surface, is based on the relative index of refraction between the reflecting material and medium of propagation, as well as the angle of reflection. The Mueller matrix for light reflection from a surface is

$$\mathbf{M}_{\mathbf{reflect}} = \frac{1}{2}\left(\frac{\tan\theta_-}{\sin\theta_+}\right)\times\begin{pmatrix} \cos^2\theta_- + \cos^2\theta_+ & \cos^2\theta_- - \cos^2\theta_+ & 0 & 0 \\ \cos^2\theta_- - \cos^2\theta_+ & \cos^2\theta_- + \cos^2\theta_+ & 0 & 0 \\ 0 & 0 & -2\cos\theta_+\cos\theta_- & 0 \\ 0 & 0 & 0 & -2\cos\theta_+\cos\theta_- \end{pmatrix} \quad (3.6)$$

where θ_- is the incident angle, θ_i, subtracted from the refracted angle, θ_r; and θ_+ is the addition of θ_i and θ_r. Equation (3.7) presents the Mueller matrix of the light refracted through the surface:

$$\mathbf{M}_{\mathbf{refract}} = \left(\frac{\sin 2\theta_i \sin 2\theta_r}{2\left(\sin\theta_+\cos\theta_-\right)^2}\right)\times\begin{pmatrix} \cos^2\theta_- + 1 & \cos^2\theta_- - 1 & 0 & 0 \\ \cos^2\theta_- - 1 & \cos^2\theta_- + 1 & 0 & 0 \\ 0 & 0 & 2\cos\theta_- & 0 \\ 0 & 0 & 0 & 2\cos\theta_- \end{pmatrix} \quad (3.7)$$

The incident and refracted angles are related by Snell's law, which relates the index of medium 1 (n_1) and the incident angle (θ_i) to the index of medium 2 (n_2) and the refracted angle (θ_r):

$$n_1 \sin\theta_i = n_2 \sin\theta_r \quad (3.8)$$

The Stokes vector for light reflected from a surface can be computed by multiplying the incident Stokes vector with the Mueller matrix of reflection from the surface (3.6). Assuming an incident unpolarized light (i.e., $S_{\text{in}}=[1\ 0\ 0\ 0]^{\text{T}}$), computing the reflected light, $\mathbf{S_{out}}=\mathbf{S}\cdot\mathbf{M_{reflect}}$, for all possible incident angles (0° to 90°) results in a graph like Figure 1, which is an example using air (n_1 = 1) and glass (n_2 = 1.5) as the two indices of refraction. In Figure 1, the black line represents

reflection and the gray line represents refraction of light. As can be seen in Figure 3.1, the DoLP for glass has a maximum value of 1 for an incident angle of 56.7°. This angle is known as the *Brewster angle*, and it is often used to determine the index of refraction of a material in instruments such as ellipsometers.

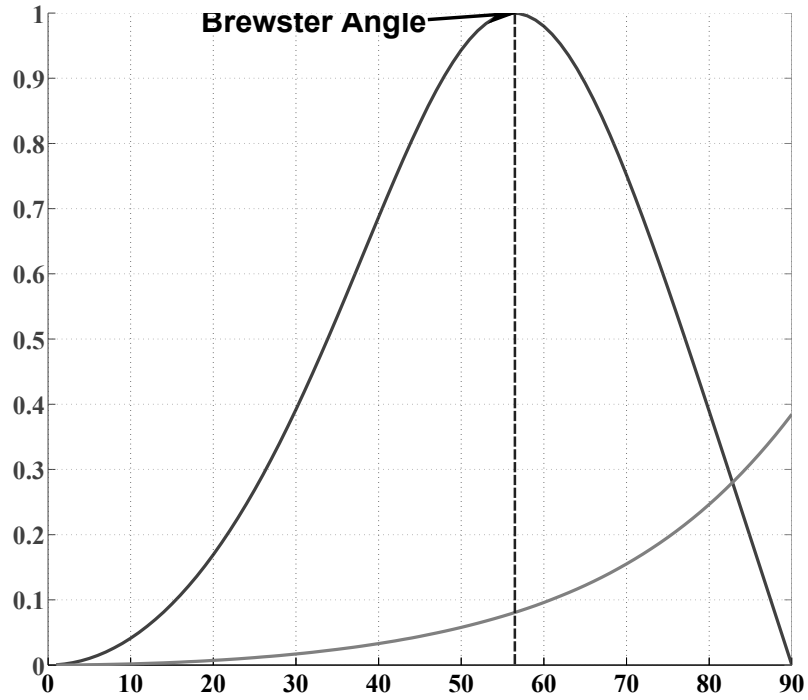

Figure 3.1: Degree of linearly polarized light for both reflected and refracted light as a function of incident angle. In this example, air (n1 = 1) and glass (n2 = 1.5) are the two indices of refraction. The maximum degree of linear polarization occurs at the Brewster angle, information that can be used to identify the index of refraction of a material.

This same concept has been utilized in nature. For example, water beetles, which are attracted to the horizontally polarized light that reflects off of the surface of water, typically land on the water surface at 53°, which is the Brewster angle of water [19]. By measuring the maximum polarization signatures of the reflected light as a function of incident/reflected angle, water beetles estimate the Brewster angle of the water surface and possibly uniquely determine the location of water surfaces.

3.1.3 Polarization of Light Through Scattering

Light scatters when it encounters a charge or particle in free space. The charge or particle impacts the electric field as the field propagates through space, and this influence can affect the polarization state of the light. An example is the Rayleigh model of the sky In the Rayleigh model, light scattered from a particle in a direction orthogonal to the axis of propagation becomes linearly polarized. This ballistic scattering from the many particles in the atmosphere creates a polarization pattern in both the DoLP and AoP across the sky based on the position of the sun. In nature, the desert ant *Cataglyphis fortis* uses this polarization pattern of the sky to aid its navigation to and from home [20]. Honeybees also use sky polarization as part of their "waggle dance" to indicate the direction of food [21]. There is even increasing evidence that birds combine magnetic fields and celestial polarization for navigation purposes [22], [23].

Optical scattering is present in biological tissue as well. The scattering agents for light as it propagates through tissue include cells, organelles, and particles, among others. Because many of these components can be on the order of the wavelength of the propagating light, the Mie approximate solution to the Maxwell equations, which is typically referred to as the *Mie scattering model*, can be used to describe the effects of scattering on polarization. Absorption by tissue attenuates the intensity of light, while scattering causes a depolarization of light in the general direction of propagation. The density of the scattering agents in a tissue influences the depolarization signature of the imaged tissue. For example, high-scattering agents are typically found in cancerous tissue, which leads to depolarization of the reflected or refracted light from a tissue. Hence, there is a high correlation of light depolarization with cancerous and precancerous tissue, and detecting polarization of light can aid in early detection of these tissues [24].

3.2 Polarization Image Sensors

Natural biological designs have served as the motivation for many unique sensor topologies. Real-time (i.e., 30 frames-per-second), full-frame image sensors [4] are a simple approach to a visual system, capturing all visual information at a given time. However, this typically creates bottlenecks in data transmission, as well as non-real-time information processing due to the large volume of image data presented to a digital processor such as computer, digital signal processors (DSP), or field programmable gate arrays (FPGA). Signal processing at the focal plane, as it is typically performed in nature, can lead to significant reduction of data that are both transmitted and processed off-chip. Hence, sparse signal processing, as is found in the early visual processing in many species, such as the mantis shrimp, can serve as inspiration for efficient, low-power artificial imaging systems [25].

In the mid-1980s a new sensor design philosophy emerged, where engineers looked at biology to gain understanding in developing lower-power visual, auditory, and olfactory sensors. Some early designs [26] attempted a complete silicon model of the retina, using logarithmic photoreceptors with resistive interconnects to produce an array whose voltage at a location is a weighted spatial average of neighboring photoreceptors. Other designs sought to replicate neural firing patterns by asynchronously outputting only when detecting significant changes from each photosensitive pixel [27]–[29] or significant color changes from color-sensitive pixels [30], [31]. Some designs have even sought to directly mimic the compound eye of insects [32].

One of the main benefits of these systems has been a low-power and real-time realization of information extraction at the sensor level. These sensors have found a niche in various remote-sensing applications where power is a major constraint for sensor development [33].

Furthermore, in these applications, extracting information at the sensor level and transmitting preprocessed data can greatly reduce bandwidth and overall power consumption.

3.2.1 Classical Polarization Sensors

The polarization selectivity depends on the ability to measure the Stokes parameters. From (3.2), the intensity of light measured with a linear polarizer with a retarder depends on the angle of the linear polarizer (θ), the phase retardance (ϕ), and the four Stokes parameters. A unique solution for the Stokes parameters in (3.2) thus requires a number of measurements equal to the number of desired Stokes parameters.

To determine all four Stokes parameters, four distinct measurements are made with linear polarization filters and quarter-wave retarders. Hence, the four Stokes parameters can be determined as follows:

$$\begin{bmatrix} S_0 = I(0^\circ,0^\circ) + I(90^\circ,0^\circ) \\ S_1 = I(0^\circ,0^\circ) - I(90^\circ,0^\circ) \\ S_2 = I(45^\circ,0^\circ) - I(135^\circ,0^\circ) \\ S_3 = S_0 - I(45^\circ,90^\circ) \end{bmatrix} \quad (3.8)$$

In these equations, I(0°,0°) is the intensity of the e-vector filtered with a 0° linear polarization filter and no phase retardation; I(45°,0°) is the intensity of the e-vector filtered with a 45° linear polarization filter and no phase retardation; and so on. The fourth Stokes parameter is computed with a 45° linear polarization filter and a quarter-wave retarder.

The most predominant method of Stokes measurement solves these equations by rotating a linear polarization filter and retarder in front of the sensor, capturing a static image at each rotation. This type of sensor is called a division-of-time polarimeter [34], since it requires capturing the same scene at multiple steps in time. This simple design suffers from a reduced

frame rate, as each complete set of measurements requires multiple frames. It also requires a static scene for the duration of the measurement, since any change in the scene between rotations would induce a motion blur. As this is the simplest method for measuring static scenes, Division-of-Time polarimeters have realized a number of applications, from 3D shape reconstruction [35], haze reduction [36], mapping the connectome [37], and many others.

An alternate method with static optics projects the same scene to multiple sensors. Each sensor uses a different polarizer and/or retarder in front of the optical sensor to solve for the different Stokes parameters. This type of modality is called division of amplitude [34] since the same optical scene is projected full frame multiple times at reduced amplitude per projection. The drawback to this system can be the bulk and expense of having a large array of optics and multiple sensors. Maintaining a fixed alignment of the optics so all sensors see the same co-registered image also poses a challenge to this polarization architecture, which typically requires image registration in software. These types of instruments have found some use in UAV applications [38], [39], target detection in cluttered environments [40], and measuring the ocean radiance distribution [41]. A similar optically static method uses optics to project the same scene to different subsections of a single sensor. Each subsection contains a different analyzer to solve for the Stokes parameters. This type of sensor is called a division-of-aperture polarimeter [34], since the aperture of the sensor is subdivided for polarization measurement of the same scene. The advantage is that it requires only one sensor, but the disadvantage is that it is prone to misalignment and can contain a long optics train. Multiple scene sampling on the same array also reduces the effective resolution of the sensor, without the possibility of upsampling through interpolation. The system complexity, from maintaining the optical alignment to the image processing, have precluded them from wider use.

3.2.2 Bio-inspired Polarization Imaging Sensors

Taking a cue from nature, however, would mate the polarization analyzers directly to the photosensitive element. Figure 3.2 (left) shows an example of how nature has evolved polarization-sensitive vision. The compound eye of the mantis shrimp contains a group of individual photocells called an ommatidium. Each ommatidium has a cornea that focuses external light. The focused light is filtered through a pigment cell for color sensitivity and passes through a series of photosensitive retinular cells (R-cells). In the mantis shrimp, these cells contain an array of microvilli that can act as polarization filters. The photosensitive R-cells will signal the brain via the optic nerve, and the brain extracts visual information based on input from the array of ommatidia.

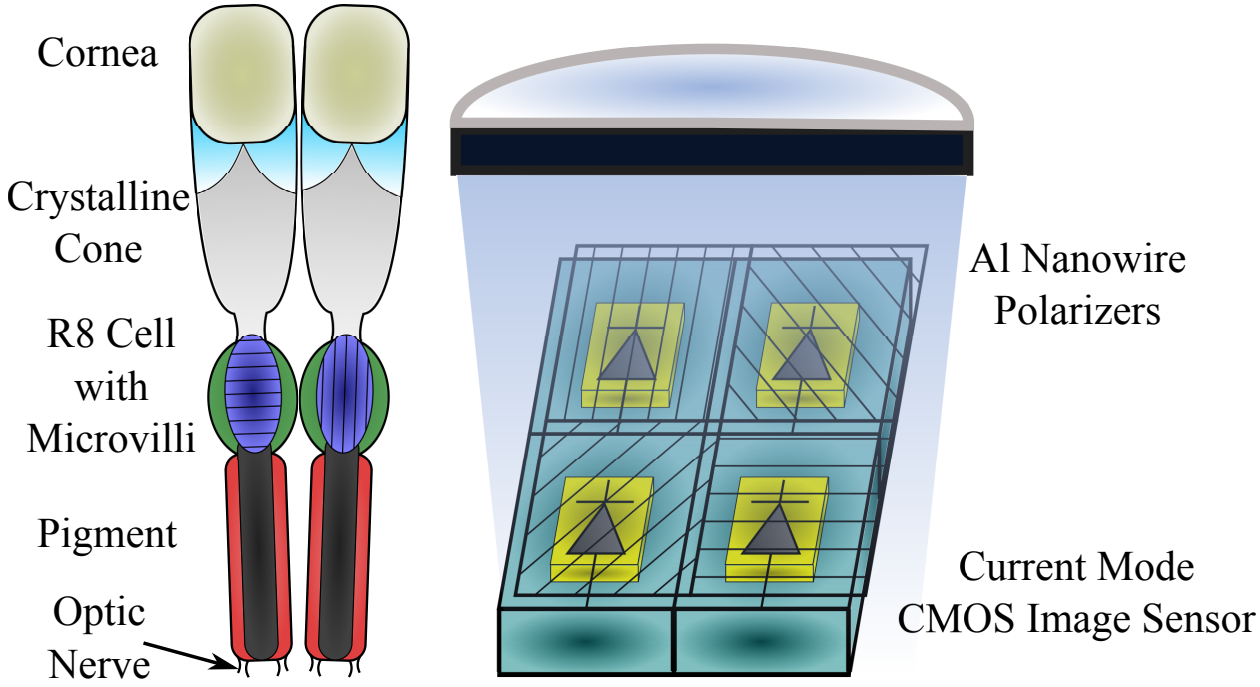

Figure 3.2: Left, The compound eye of the mantis shrimp, where ommatidia combine polarization-filtering microvilli with light-sensitive receptors. Right, a bio-inspired CMOS imager constructed with polarization sensitivity, where aluminum nanowires placed directly on top of photodiodes act as linear polarization filters.

Biomimetic approaches have also attempted to replicate the polarization sensitivity present in certain species. Early designs integrated liquid crystals [42] or birefringent crystals [43] directly to pixels. These sensors allowed for full-frame polarization contrast imaging. More advanced polarization sensors integrated filters at multiple orientations, which enabled capture of the first three Stokes parameters [7], [8], [44].

Further advances in nanotechnology and monolithic integration of nanowires with CMOS technology have enabled high-resolution versions of this paradigm [2]. The use of liquid crystal polymers and dichroic dyes has allowed a full Stokes polarimeter [45], [46] These sensors are capable of capturing polarization information at video frame rates, and their compact realization has allowed them to pertain to remote-sensing applications, such as underwater imaging [47].

Other polarization sensor designs have attempted alternate, more biologically pertinent designs. As octopuses are known to have polarization-sensitive vision [48], a design based on polarization contrast with a resistive network sought to replicate the octopus vision system in silicon [49]. Polarization sensor designs have been developed that utilize asynchronous address event mode to output only when there are large enough changes in polarization contrast [50]. In this work, both the ommatidia functionality and neural processing circuitry have been efficiently implemented in CMOS technology.

Analogous to the microvilli in the mantis shrimp vision system [51], which function as polarization-filtering elements, bio-inspired polarization sensors use pixel-matched aluminum nanowire polarization filters at 0°, 45°, 90°, and 135°, arrayed in a 2-by-2 grid called a superpixel [2], [52] (see Figure 3.2, right). These filters are fabricated to be 70 nm wide and 200 nm tall and have a horizontal pitch of 140 nm. The filters are deposited post fabrication of the

CMOS imager through an interference lithography process, matching the pixel pitch of the imager array of 7.4 μm by 7.4 μm. Maintaining an air gap between these filters allows for a higher extinction ratio than does embedding the filters within a layer of silicon dioxide [53].

With the maturity of nanofabrication techniques, many interesting optical designs have become feasible. For example, metamaterial surfaces acting as achromatic quarter-wave plates [54] or as high-extinction ratio polarization filters [55] can further advance the field of polarization imaging when integrated with an array of imaging elements. These advances will bring the complete imaging system design closer to biology in terms of sensitivity and selectivity to both spectral and polarization information. Foundries such as TowerJazz Semiconductor (Migdal Haemek, Israel), Dongbu HiTek (Bucheon, Korea), LFoundry (Avezzano, Italy), and TSMC (Hsinchu, Taiwan) already offer specialized CMOS fabrication processes explicitly optimized for image sensors. However, polarization-filtering capabilities are not included in regular image sensor fabrication. The key would be to integrate these emerging optical fabrication techniques with these specialized CMOS fabrication technologies at the foundry level for optimal optical performance and high yield. With such an integrated solution, future polarization imaging designs could incorporate low-power analog circuitry that mimics neural circuitry, leading to sparse on-chip computation.

3.3 Current Mode CMOS Polarization Image Sensor

We have designed a bio-inspired polarization imaging sensor by combining CMOS imaging technology with nanofabrication techniques to realize linear polarization filters. In this bio-inspired vision system, the photosensitive elements are monolithically integrated with aluminum nanowires, or microvilli, acting as linear polarization filters. The bio-inspired photosensitive element is based on a current-mode CMOS imaging paradigm. The signal from

the diode is linearly converted into a current inside the pixel, and the image is then formed from each of the independent pixels.

Circuitry on the pixel and for readout is presented in Figure 2.1. The pixel consists of a charge transfer transistor (M1), reset transistor (M2), transconductance amplifier (M3), and select transistor (M4). Through a series of switching multiplexers, the output of the pixel connects either to a reset voltage, V_{reset}, or to the readout current conveyor. This bus-sharing methodology eliminates the need for two separate buses to separately connect the drain of the readout transistor and the output current bus, which reduces the pixel pitch. The transconductance amplifier (M3), also known as the readout transistor, is biased to operate in the linear mode. This ensures a linear relationship between an output drain current and input photovoltage applied at the gate of transistor M3. The linearity is critical in correcting threshold offset mismatches between readout transistors via a technique known as *correlated double sampling* (CDS).

Current-mode image sensors rely on current conveyors to copy currents from the pixels to the periphery while providing a fixed reference voltage to the input node, that is, to the drain node of the pixel's readout transistor (M3). The classic current conveyor design [56] uses four transistors, two n-channel (NMOS) and two p-channel (PMOS) metal-oxide-semiconductor transistors, in a complementary configuration. The design is compact, but the output impedance is limited, and the transistors are subject to nonlinearity due to channel length modulation. Furthermore, the voltage at the input terminal of the current conveyor (i.e., the voltage at the drain node of the pixel's readout transistor) can vary as much as 20% for the typical input current from a pixel. A single transistor design [57] improves settling time and power consumption but decreases linearity of the output current.

Because the polarization information conveyed in the S_1 and S_2 parameters is based on the linear difference in pixel intensities, pixel linearity is crucial to accurate polarization measurement. Alternate current conveyor designs use an operational amplifier with a transistor in the feedback path. The conveyor has high linearity and can be used for novel current-mode designs [58], but at the cost of increased power consumption and area.

To improve the performance of the output current conveyor, a regulated cascoded structure for the current conveyor is used. Since all transistors in the current conveyor operate in the saturation mode, the potentials on the gates of transistors M13 and M14 are set by a biasing current. Since the gate potential of M13 (M14) and drain potential of M15 (M16) are the same, the channel length modulation effect is eliminated between the two branches, and the two drain currents are the same. Furthermore, the impedance of the output branch is increased due to the regulated cascode structure by a factor of $(g_m * r_o)2$, where g_m is the transconductance and r_o is the small signal output impedance. The high output impedance of the output branch is important when supplying a current to the next processing stage. This improved performance does come at a cost of increase in chip area compared with the aforementioned implementations.

The row-parallel current conveyors set the reference voltage on the output bus and copy the current from the pixel to the output branch, using transistor M20 to switch along the pixels in the column. The current conveyors are implemented by connecting two current mirrors in a negative feedback configuration. Transistors M11 through M16 form a PMOS-regulated cascode current mirror connected with an NMOS-regulated cascode current mirror composed of transistors M5 through M8. Transistors M13 and M14 operate in the saturation region, and the gate-to-source potentials are set by a reference current source of 1 μA. Hence, the drain nodes of transistors M15 and M16 are at the same potential. Transistors M11 and M12 provide negative

feedback to transistors M13 and M14, respectively, ensuring that all transistors remain in the saturation mode of operation. Since transistors M15 and M16 have the same source, gate, and drain potential, the drain currents flowing through these two transistors are the same.

Transistors M7 and M8 pin the drain voltage of transistors M5 and M6 because the bias current through these transistors sets the gate voltage on each, respectively. Since the currents are the same flowing through transistors M5 and M6, and since the gate and drain potentials are the same for these transistors, the drain potential is the same for these transistors. Therefore, the drain potential on transistor M5 is set to V_{ref}.

The readout transistor in the pixel (M3) is designed to operate in the linear current mode by ensuring that the drain potential of the M3 transistor is lower than the gate potential by a threshold during the entire mode of operation. This is achieved by setting the V_{ref} bias potential to 0.2 V and resetting the pixel, which sets the gate voltage of M3 to 2.7 V. Since the threshold voltage of the transistor is ~0.6 V, the lower limit on the gate of M3 transistor is set to 0.7 V in order to operate in the linear mode. The output current from transistor M3 is described by

$$I_{photo} = \mu_n C_{ox} \frac{W}{L}\left(\left(V_{photo} - V_{TH,M1}\right)V_{ref} - \frac{V_{ref}^2}{2}\right) \quad (3.9)$$

In equation (3.9), μ_n is the mobility of electrons, C_{ox} is the gate capacitance and V_{th} is the threshold voltage of the transistor. The current conveyor holds V_{ref} on the drain of the readout transistor M3. By keeping V_{ref} constant, the output current is linear with respect to the photovoltage.

The pixel timing is shown in Figure 3.4. During *FD Reset*, reset transistor M2 and select transistor M4 are activated. With these transistors activated, setting the voltage on the *Out* node

of the pixel to V_{reset} drives the floating diffusion node, V_{fd}, to the reset potential. After resetting the floating diffusion, the reset value can be read out during *Reset Readout* for difference double sampling. During the *Pixel to FD* stage the charge transfer transistor M1 activates, placing the integrated photovoltage onto the floating diffusion. After turning M1 off, readout of all the pixels in the row takes place. M1 reactivates during *Pixel Reset*, after which the *Out* switches back to V_{reset}, and M2 reactivates, pulling the photodiode up to the reset potential. All three switch transistors turn off, and the readout proceeds to the next column.

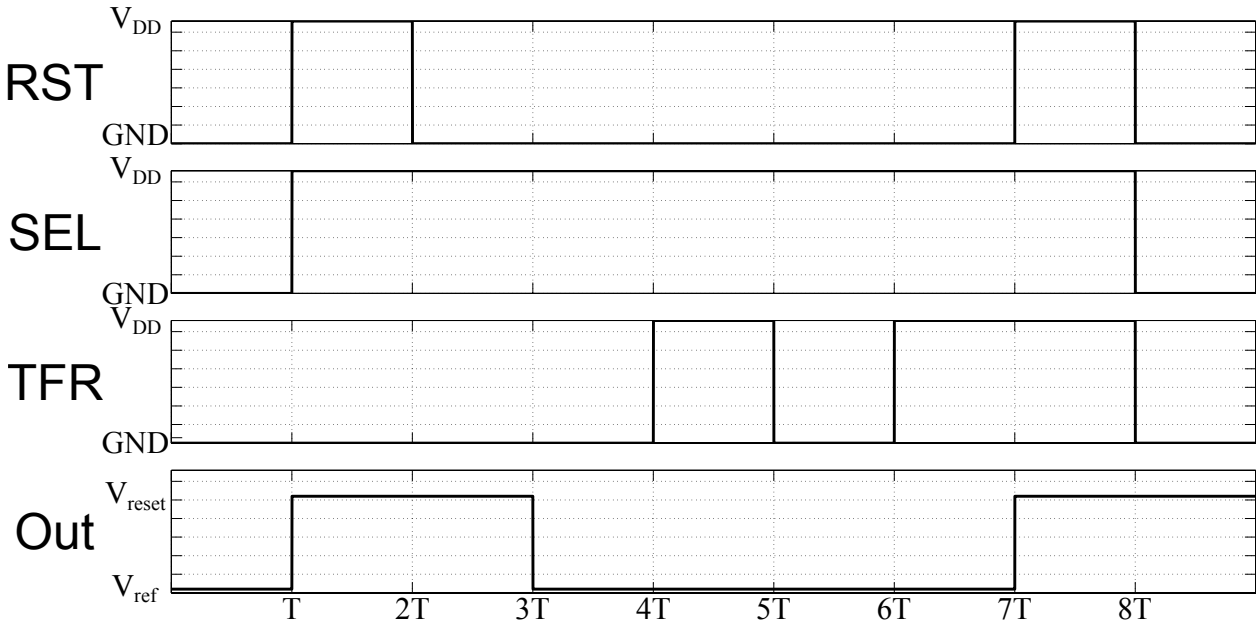

Figure 3.4: Timing diagram of current mode image sensor

The pixel's layout is implemented in a 180-nm-feature CMOS image sensor process with pinned photodiode capabilities. Figure 5 shows a schematic of the pixel. The charge transfer transistor is highly optimized to allow full transfer of all charges from the photodiode capacitance to the floating diffusion, with the node heavily shielded for light sensitivity. This node is capable of holding electron charges with no significant losses for over 5 ms at an intensity of 60 $\mu W/cm^2$.

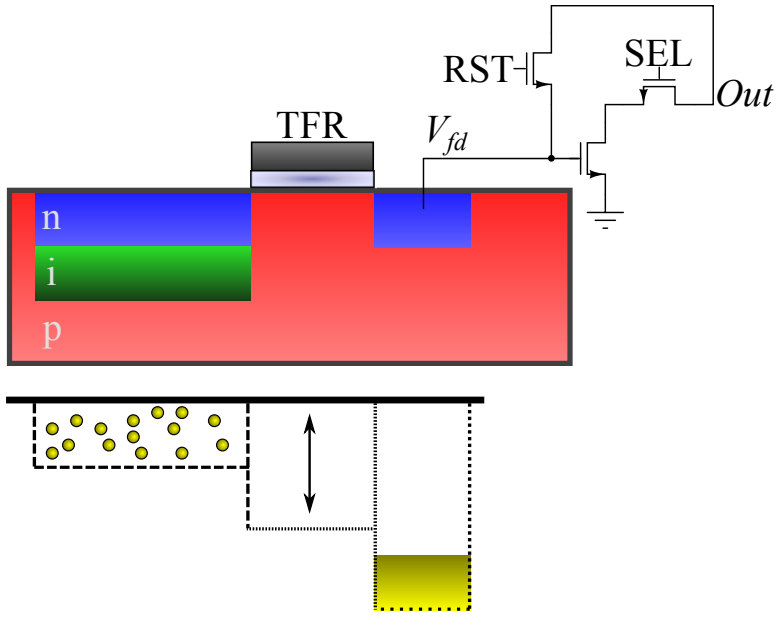

Figure 3.5: Cross section of the pinned photodiode together with the reset, transfer, readout, and select transistors. The diode is an n-type diode on a p-substrate with an insulating barrier between. The readout transistor operates as a transconductor, providing a linear relationship between accumulated photo charges and an output current

3.4 Electrical characterization of the CMOS image sensor

The current mode polarization sensor described in Section 3.3 was given a series of electrical and optical tests to characterize its performance. For the electrical tests, a set of narrowband LEDs (OPTEK OVTL01LGAGS) were placed flush to an integrating sphere (Thorlabs IS200). The light was then collimated with an aspheric condensing lens (Thorlabs ACL2520) before reaching the sensor. The intensity of the light was changed by altering the current through the LEDs with a DC constant-current power supply (Agilent E3631A). The reference optical intensity was measured at the focal plane of the sensor with a calibrated photodiode (Thorlabs S120VC). Figure 3.6a shows a diagram of the setup.

Figure 3.7 shows the output current measured as a function of the incident light intensity. The current shows a linear response with respect to the incident light, with 99% linearity in the range. This primarily results from the current conveyor. The regulated cascode structure helps

eliminate channel length modulation while also maintaining a steady voltage reference. Figure 3.8 shows the signal-to-noise ratio (SNR) of the current-mode sensor. The maximum SNR for our sensor is 43.6 dB, consistent with the shot noise limit based on the pixel well-depth capacity. Figure 3.9 shows a histogram of image intensities. The fixed-pattern-noise for room light intensity is 0.1% from the saturated level, comparable to voltage-mode imaging sensors. Also, due to the low currents and small array size, bus resistance variation remains minimal.

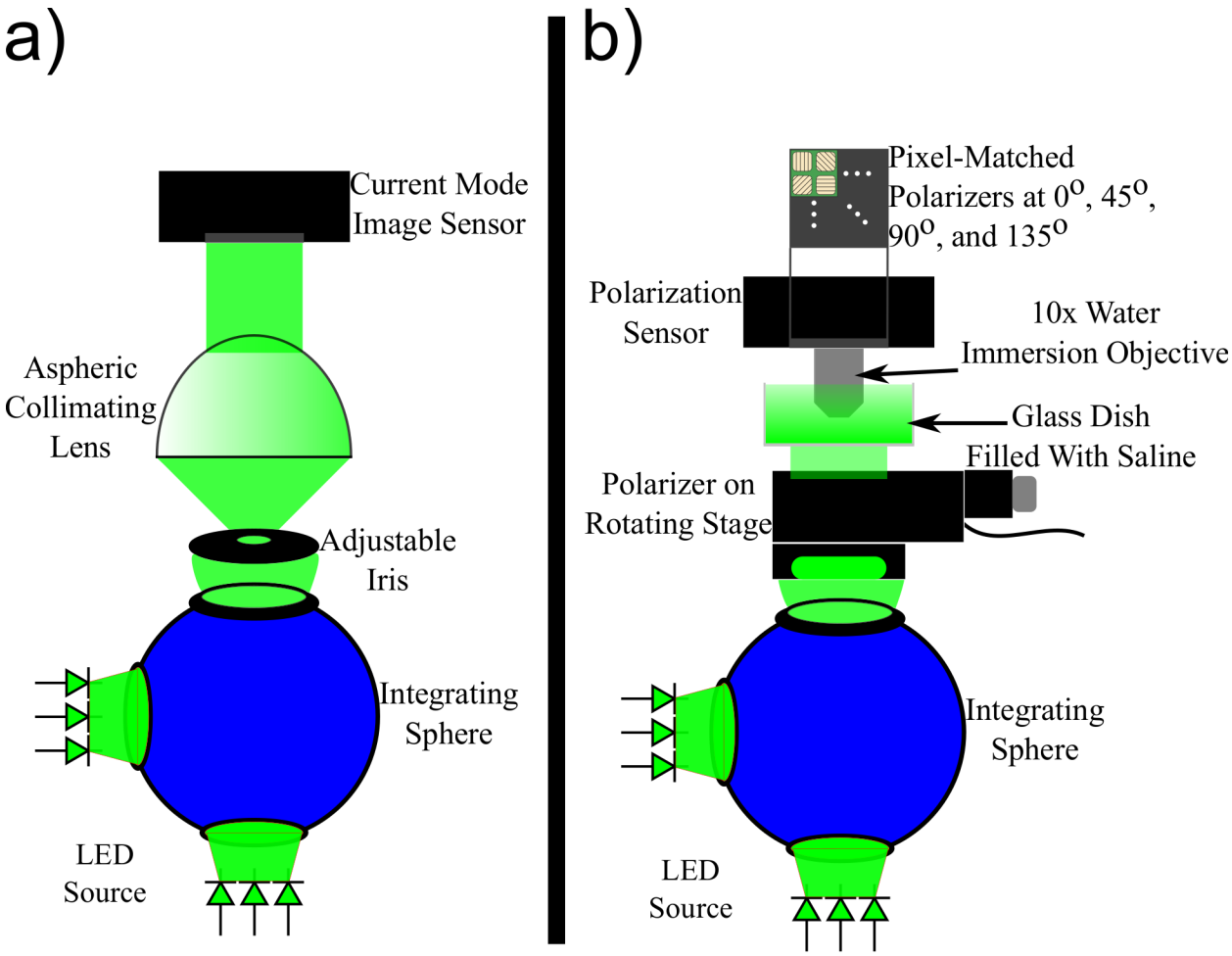

Figure 3.6: a) Setup for electrical characterization. The integrating sphere/aspheric lens combination creates a uniform field. b) Setup for polarization characterization, using the same water-immersion lens, submerged in saline, as used for neural recording experiments.

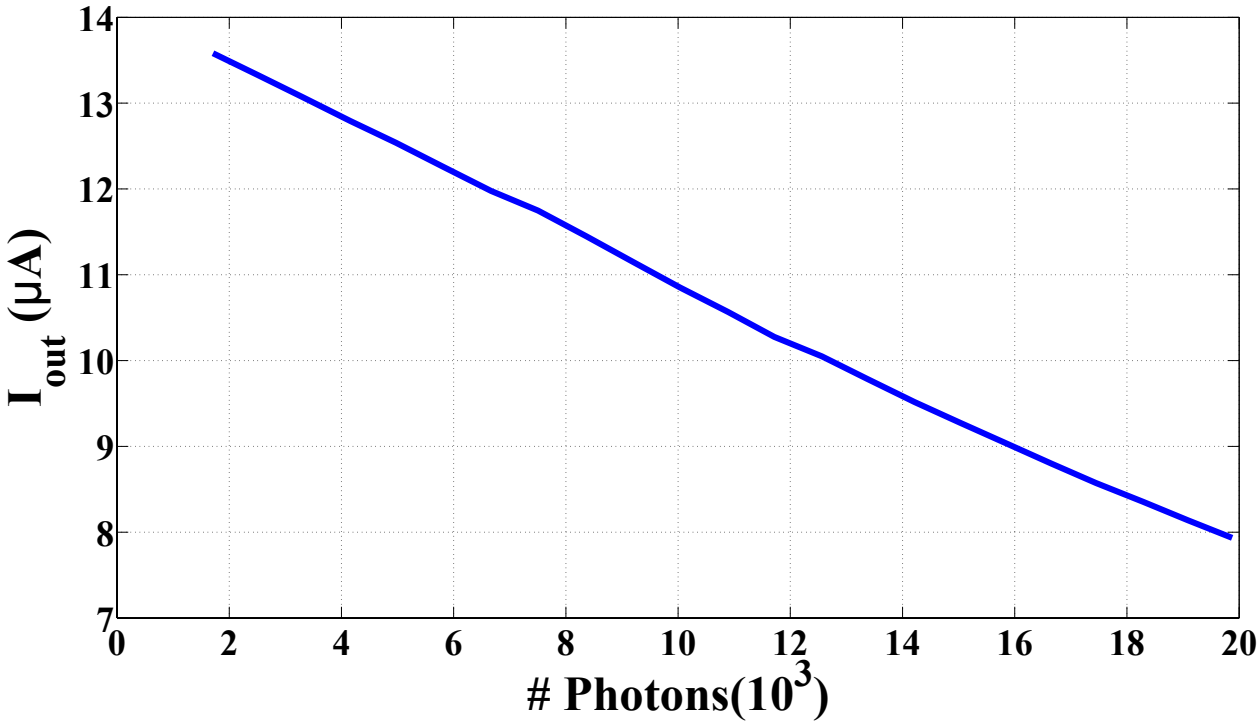

Figure 3.7: Measured output current from a pixel vs. number of incident photons on the photodiode.

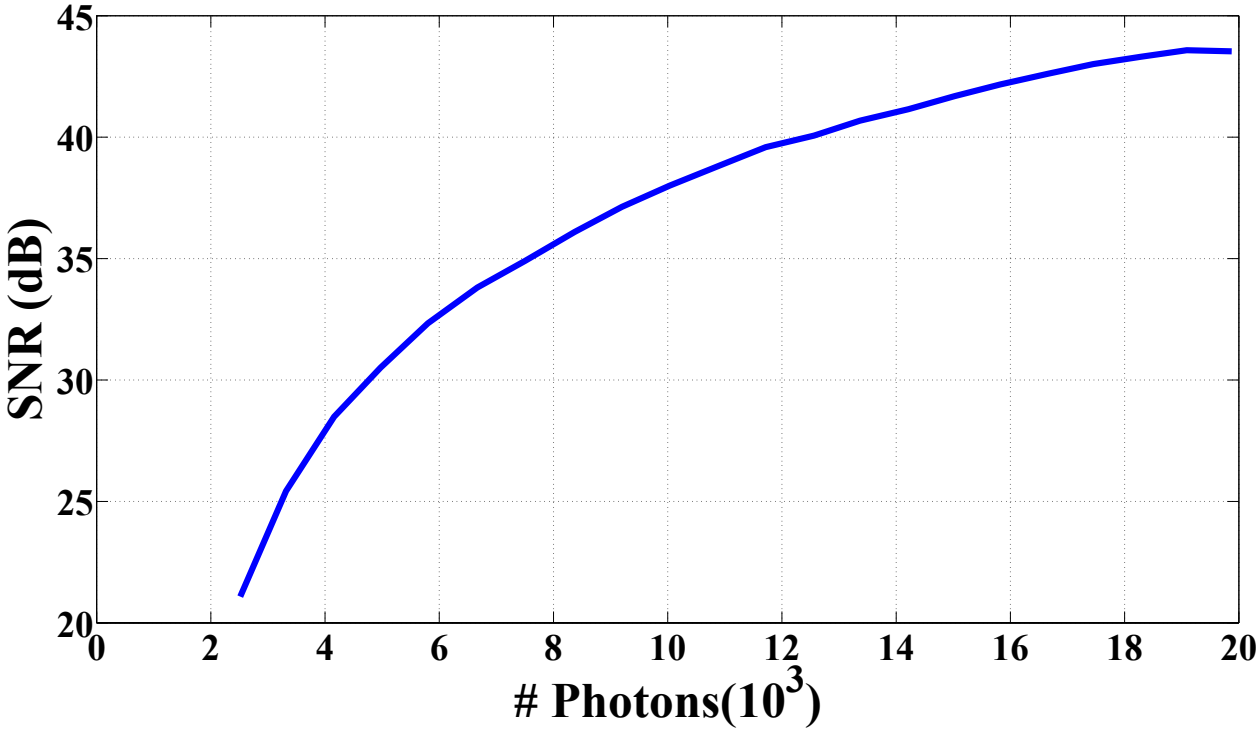

Figure 3.8: Signal-to-noise ratio of the current-mode imaging sensor as a function of number of incident photons.

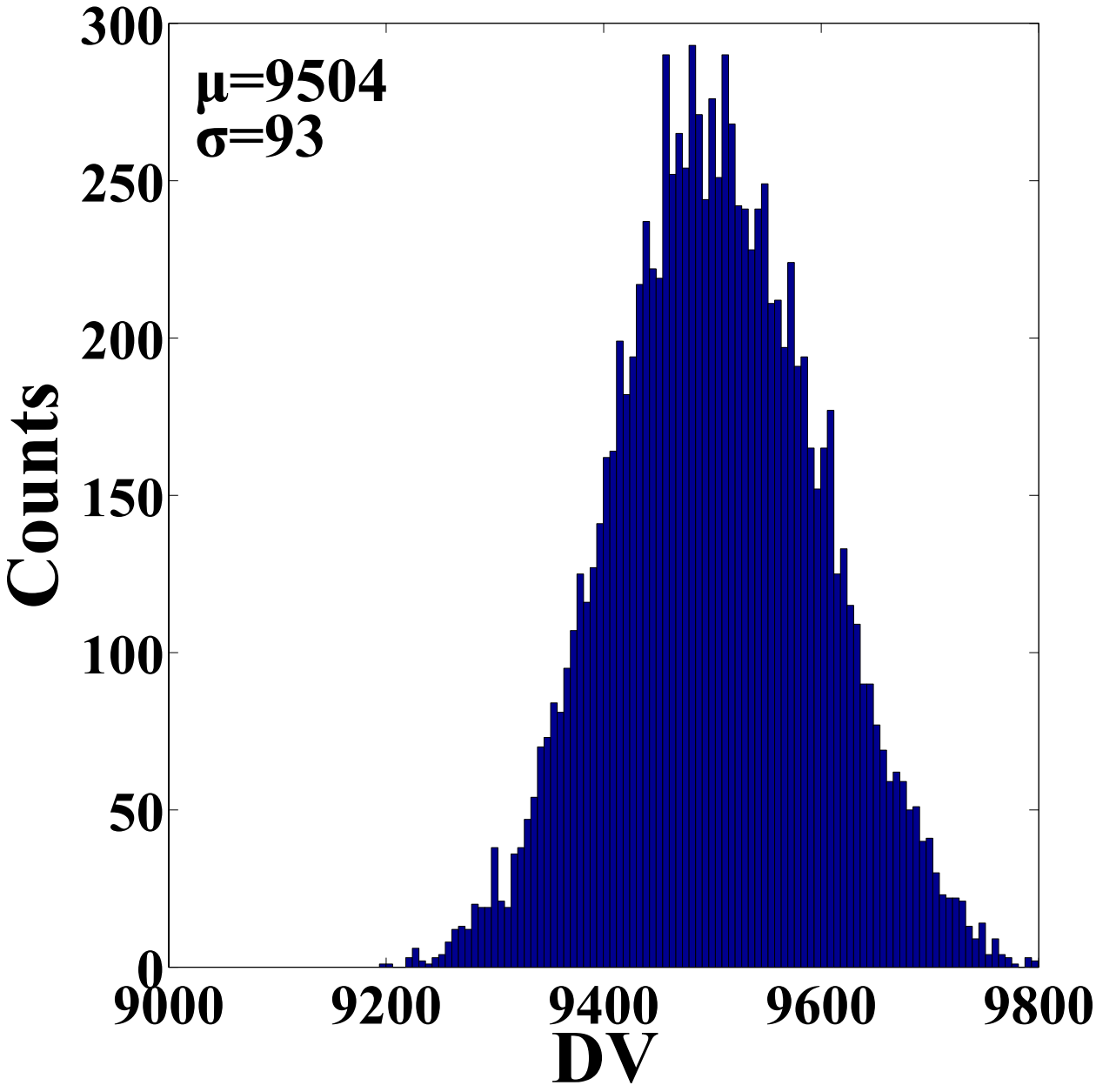

Figure 3.9: Histogram of all responses of pixels in the imaging array to a uniform illumination at room light intensity. The fixed pattern noise of the current-mode imaging sensor is 0.1% from the saturated value

3.5 Polarization characterization of the sensor

For the polarization characterization, to better calibrate for the optics used in the neural recording experiments presented in Chapter 5.2 below, the same integrating sphere/LED combination was used as the light source. A rotating polarization element (Newport 10LP-Vis-B

mounted in a Thorlabs PRM1Z8 stage) was used to generate input linearly polarized light of a known AoP. The sensor used a 10x water-immersion lens (Olympus UMPLFLN10XW) submerged in a glass dish of water to view the flat field generated from the light source. Figure 3.6b shows a diagram of the setup.

The sensor was tested for polarization sensitivity. To improve polarization sensitivity, a Mueller matrix calibration approach was used [59]. Figure 3.10 shows the pixel response to polarized light after calibration. Malus's law (3.10) describes the intensity of light seen through two polarizers offset at θ_i degrees:

$$I = I_0 \cos^2 \theta_i \qquad (3.10)$$

The pixels in the polarization sensor show nearly the same response. The more uniform response after calibration also manifests in a more linear AoP than the raw measurement, as depicted in Figure 3.11.

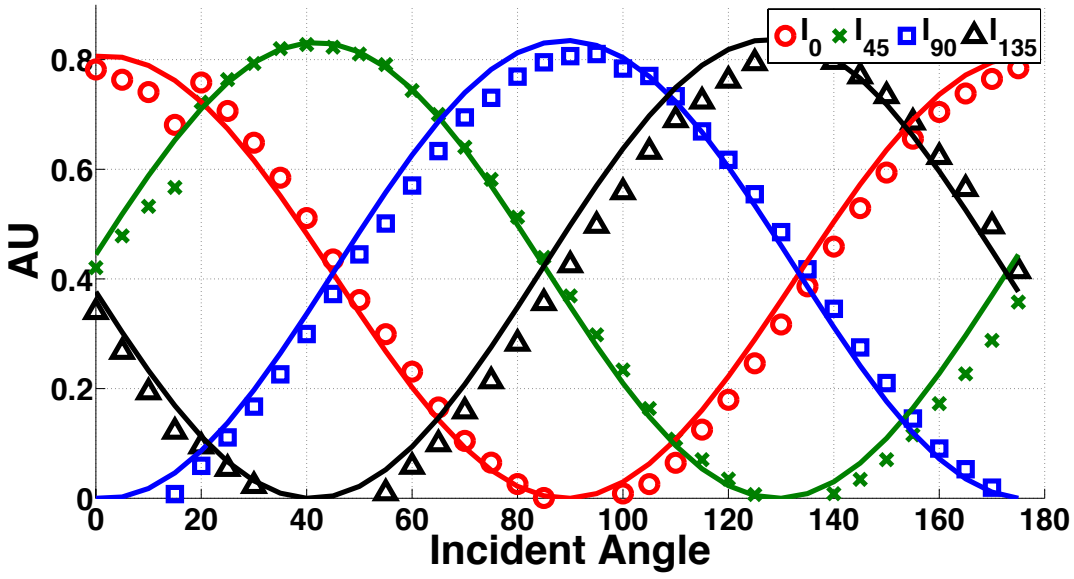

Figure 3.10: Optical response to four neighboring pixels to incident linearly polarized light. As the angle of polarization of the incident light is swept from 0° to 180°, the pixels follow Malus's law for polarization.

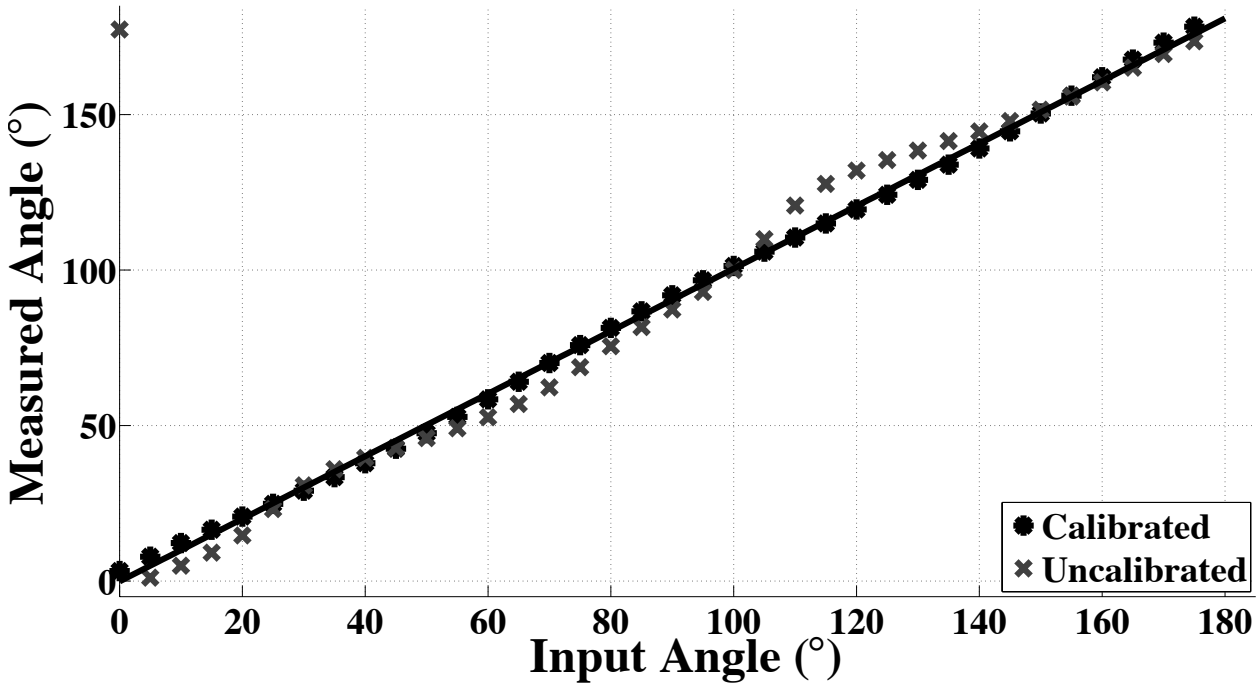

Figure 3.11: Measured angle of polarization as a function of the incident light angle of polarization for our bio-inspired polarization imager.

3.6 Conclusion

The polarization of light describes the orientation of the oscillation of light as it propagates through space. In nature, unpolarized sunlight becomes polarized through reflection and scattering. Detecting this polarized light has proved advantageous for many biological species. These species have shown the effectiveness of compact, integrated optics for polarization detection. We have mimicked their design with our own compact, division-of-focal-plane polarimeter that uses a custom designed CMOS current mode image sensor integrated with aluminum nanowire polarization filters. The sensor, fabricated in a specialized 180nm CMOS image sensor process, is 220x128 pixels. It demonstrates a linearity of 99%, a dynamic range of 56 dB, a peak signal-to-noise ratio of 43 dB, and a fixed pattern noise of 0.1%. The sensor retains a polarization response that closely matches the theoretical after applying calibration.

Chapter 4: Polarization Measurement Methodology [60]

Polarization is a fundamental property of the wave nature of light, describing the orientation of an electromagnetic wave as it oscillates through space and time. The interaction of light with materials can change its polarization state, from Rayleigh scattering in an atmosphere to Fresnel reflectance and transmission. Thus, development of many useful applications relies on the ability to accurately measure the polarization of light. Polarization provides a method for detecting skin cancers [61] and cervical cancers [62]. Observation of the polarization of light has also found use in material classification [63]–[65], fingerprint detection [66], and haze removal [36]. Detection of light's polarization state also makes possible three-dimensional shape recovery [35], [67].

Numerous methods of measuring the polarization state of light have been demonstrated [34], [68] for many ranges of wavelengths. In the visible spectrum, division-of-time, division-of-amplitude, or division-of-aperture polarimeters are commonly used. A division-of-time polarimeter utilizes a rotating linear polarizer in front of a standard image sensor. The sensor captures the scene at several orientations of the polarizer, combining them to compute a Stokes vector for each pixel of the sensor. A division-of-amplitude polarimeter projects the scene onto multiple sensors, each containing a uniquely polarized optical path [69]. The images are coregistered and combined from each sensor to also give a per-pixel Stokes vector representation of the scene. A division-of-aperture polarimeter contains optics that project an incident scene onto multiple locations of a single focal plane array [70], [71]. A unique polarization optic filters each projection, and they are then combined to compute the Stokes vector at each projected point in the imaged scene.

A division-of-focal-plane (DoFP) polarimeter is another variation. The focal plane array of a DoFP sensor is subdivided into blocks of superpixels, where each pixel in the superpixel contains a polarization optic matched to its pitch. Computation of the Stokes vector becomes possible at each superpixel location, much like computation of color images in a Bayer array [1]. Much research on this type of polarimeter, especially in the visible spectrum, is ongoing [2], [72]–[75] due to the promise of high resolution, real-time polarization imagery, with fixed, aligned optics. Analogous to color sensors, the loss of spatial resolution due to subdivision of the array can be mitigated through interpolation algorithms [76]–[79]. Also like color, future developments in the fabrication and integration of pixel matched polarization optics will lead to higher quality, higher resolution arrays.

The integration of pixel matched polarization optics to charge coupled device (CCD) or complementary metal oxide semiconductor (CMOS) arrays poses a unique set of challenges in evaluation of the quality of the sensor. Both underlying pixel technologies exhibit widely varying noise characteristics, spectral sensitivities, and image quality [3]. Further, each pixel matched optic has its own unique set of properties that influence the measured polarization parameters. The challenge is to evaluate how well the sensor performs in terms of incident wavelength, intensity, and polarization state.

4.1 Parameters of Interest

DoFP polarimeters use a spatially local neighbor- hood of polarizers to estimate the Stokes vector, often neglecting the last parameter in the vector, which deals with circular polarization. In the DoFP sensor under testing [2], a CCD is monolithically integrated with aluminum nanowire polarization filters. The imaging array is arranged in two-by-two blocks of superpixels. The four pixels within one superpixel are composed of nanowire polarization filters

with the transmission axis oriented at 0°, 45°, 90°, and 135°. The nanowires are 70 nm wide, 140 nm tall, and spaced 140 nm from center to center. A detailed description of the nanofabrication procedure for realizing pixelated polarization filters can be found in [2]. The intensity measured under each filter is modulated approximately according to Malus's law for linear polarizers [68]. The combination of measured intensities allows reconstruction of the Stokes vector, as shown in Eq. (4.1). The first parameter in the vector, S_0, describes the intensity of the superpixel, taken by averaging the intensity of the two orthogonal filter pairs 0° and 90°, and 45° and 135°. The second parameter, S_1, is a measure of the vertical and horizontal polarization, with a positive value indicating a more horizontal orientation and a negative value a more vertical orientation, in reference to the sensor's optical axis. The third parameter, S_2, identifies how close the incident light is to 45° (positive) or 135° (negative), again respective to the sensor's optical axis:

$$\mathbf{S} = \begin{bmatrix} S_0 \\ S_1 \\ S_2 \end{bmatrix} = \begin{bmatrix} \frac{1}{2}\left(I_0 + I_{45} + I_{90} + I_{135}\right) \\ I_0 - I_{90} \\ I_{45} - I_{135} \end{bmatrix} \qquad (4.1)$$

Computation of the Stokes vector in this configuration allows estimation of two other parameters of interest, the degree of linear polarization (DoLP), and the angle of polarization (AoP). The DoLP, computed in Eq. (4.2), calculates the magnitude of the incident light that is due to linear polarization, expressed in the S_1 and S_2 parameters, and divides by the total intensity:

$$DoLP = \frac{\sqrt{S_1^2 + S_2^2}}{S_0} \qquad (4.2)$$

The DoLP thus provides a normalized value from zero (no linear polarization) to 1 (all incident light is linearly polarized), which describes how much of the incident light contains linear polarization. The AoP, shown in Eq (4.3), details the orientation of the incident light with respect to the sensor's optical axis:

$$AoP = \frac{1}{2}\tan^{-1}\left(\frac{S_2}{S_1}\right) \quad (4.3)$$

Both values provide useful information of the contents of a scene.

4.2 Experimental Method

Correct estimation of the DoLP and AoP under various incident lighting states is crucial to evaluating the quality of a DoFP sensor. Accomplishing this requires careful optical testing that allows direct control of the incident intensity, wavelength, and state of polarization, since a typical scene contains a wide combination of these parameters. Further, as a DoFP sensor is commonly used with standard, off-the-shelf lenses, the effects of light divergence and the viewing angle need to be measured. Additionally, trying to capture a scene may involve changes of the integration time to maximize the dynamic range. Testing the interaction of these parameters is crucial to understanding the accuracy of the sensor, and thus presented here are three different optical experiments designed to evaluate the sensor under these changing optical conditions.

4.2.1 Optical Setup for Evaluating AoP Accuracy, Field-of-View, and Spectral Response

The design of the first experiment tested a sensor's capability to accurately measure the AoP under controlled spectra, fields-of-view, and incident photon counts. The setup, shown in Fig. 4.1, used three different wavelength LEDs for incident light: 460 nm (OVG01TLGABS),

515 nm (OVG01TLGAGS), and 625 nm (OVG01TLGARS). The LEDs were assembled on custom printed circuit boards and driven by a constant current fed from a controlled power source (Agilent E3631A). They were fed through an integrating sphere (Newport 819D-SF-4) to re- move any polarization from the LED light, as well as make the input source spatially uniform. An adjustable iris (Thorlabs SM2D25) was placed on the output port of the integrating sphere and was kept at the minimum setting (0.8 mm) to approximate a pinhole. The light passed through an aspheric condensing lens (Thorlabs ACL 7560) to provide collimation, which is important for measuring a sensor's response to divergent light. A computer controlled rotational stage (Thorlabs PRM1Z8) with a mounted, high extinction ratio (>350) wire-grid polarizer (Edmunds NT47-102) created linearly polarized light at an arbitrary incident AoP. This light finally impinged upon the sensor, which was mounted on a computer controlled rotating base that allowed changes in the orientation of the sensor with respect to the input light. Rotating the sensor in such a way allowed simulation in changes of the viewing angle, an important parameter when considering optical crosstalk. The sensor connected to a PC through a Camera Link interface, which provided unified control and data transfer for the camera.

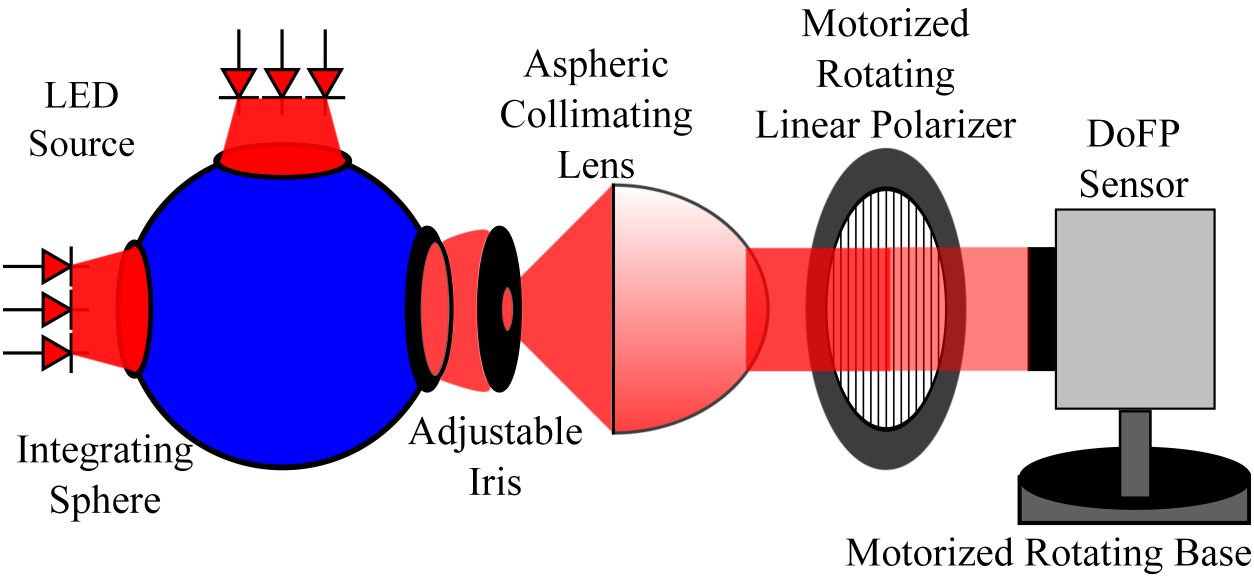

Figure 4.1: Optical setup to measure AoPs, fields-of-view, and spectra

For each LED wavelength, the sensor was positioned in direct line with the collimated input in an attempt to minimize optical crosstalk. The cur- rent through the LED boards was fixed, and the integration time of the sensor was altered from a shorter value to a longer value. The polarizer rotated from 0° to 180° in steps of 1°, with the sensor taking 1024 images at each orientation at each integration time. Finally, with the wavelength fixed at 625 nm, the sensor was moved from −5° off center to over 30° off center in increments of 2°. For each orientation, the linear polarizer rotated from 0° to 180° in increments of 1°. The integration time was also linearly cycled from low to high at each sensor orientation. The captured data are averaged over a 200×200 pixel window in the center of the imaging array.

4.2.2 Optical Setup for Measuring DoLP Accuracy

The second experiment, shown in Fig. 4.2, tested how accurately a sensor can estimate the DoLP of an incident light wave. The setup used a modified Thorlabs OSL1B halogen bulb connected directly to an Agilent N5746A DC source. This produced incoherent, broad spectrum, unpolarized light at an intensity adjusted by the computer controlled current through the bulb. An

IR blocking filter with a cutoff frequency near 700 nm (Edmund NT64-462) protected the optics from the heat of the bulb and attenuated any IR interference. The light was filtered spectrally by a Thorlabs FB450-10 for blue (450 nm), FB550-10 for green (550 nm), and FB650-10 for red (650 nm), each with an FWHM of 10 nm. Next, the light was linearly polarized at 45° using a Newport 20-LP-VISB mounted to a precision rotational stage (Thorlabs PRM1). With the light linearly polarized at 45°, the magnitudes of the $\vec{E}_x$ and $\vec{E}_y$ fields were nominally the same. The DoLP was then adjusted by varying the retardance of a Thorlabs LCV-1-VIS liquid crystal variable retarder. Adjusting the retardance to a quarter of the wavelength produced circularly polarized light, and thus the DoLP should be zero. Varying the voltage applied to the liquid crystal retarder changed the retardance, and thus the ellipticity of the incident wave. This allowed for the DoLP to be linearly changed from 0 (retardance = 0.25λ) to 1 (retardance = 0).

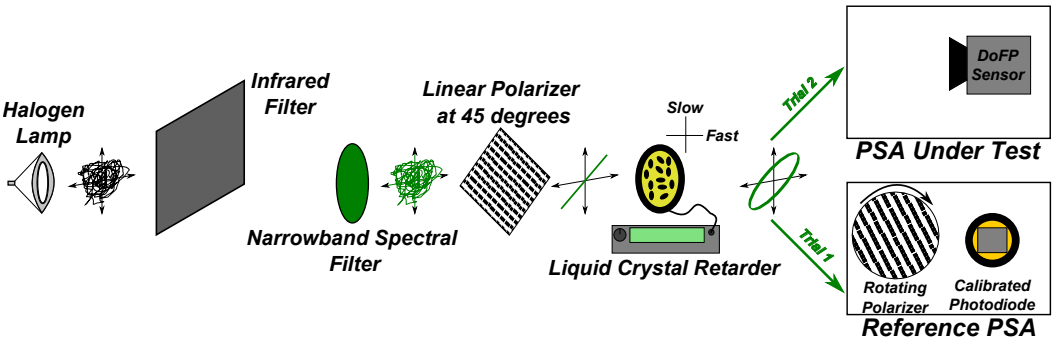

Figure 4.2: Experimental setup to measure degree of linear polarization (PSA is the polarization state analyzer)

The performance of the sensor must be compared to a reference measurement of the DoLP. This was realized through the use of a calibrated photodiode (Thorlabs S120VC) and a rotating linear polarizer (Newport 10-LP-VISB) mounted on a computer controlled rotational stage (Thorlabs PRM1Z8). Measurements were taken with the motorized stage rotating the polarizer to four states, 0°, 45°, 90°, and 135°, and sampling 2048 intensity measurements at

each orientation. The DoLP was then computed as in Section 4.2. The performance of the sensor was categorized as the root-mean-squared (RMS) error between the reference implementation with the photodiode and the measured values from the sensor.

In order to calibrate the polarization state generator, the input linear polarizer was set to be exactly 45° with respect to the optical axes of the retarder and motorized polarizer. The LCD voltage was swept over a broad range, using the motorized polarizer to sample at 45° offsets to compute the DoLP. After identifying the voltage that corresponds to the mini- mum DoLP, the voltage at which the retardance is nearest 0.25λ, the optical axis of the retarder was adjusted until the measured DoLP was zero. This off- sets the optical axes of the input linear polarizer and retarder by 45°. To align the motor, the retardance of the LCD was set to the minimal value, which corresponds to the highest LCD voltage with the Thorlabs retarder. This drives the ellipticity to zero, making the input light linearly polarized at 45°.

4.2.3 Measuring the Spectral Characteristics

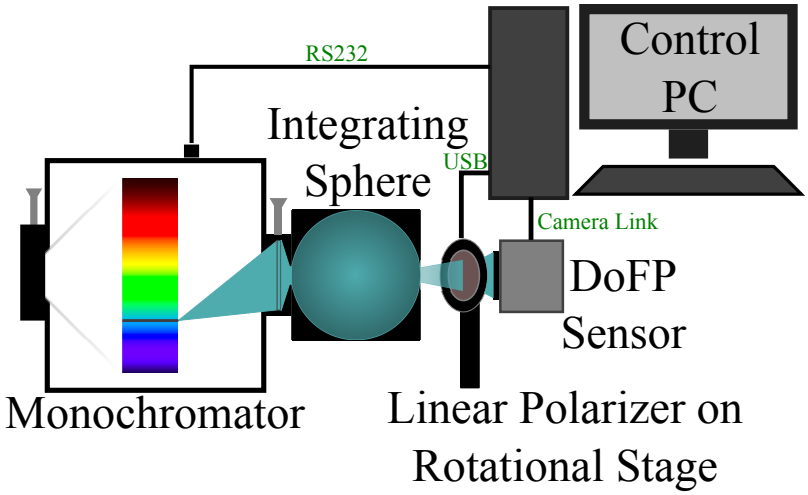

Figure 4.3: Experimental setup to measure spectral response

The third experiment, illustrated in Fig. 4.3, tested the sensor over the entire visible range at high spectral resolution. The input light source was a Princeton Instruments Acton SP2150 monochromator. A 1200 g/mm, 500 nm blaze grating was used. The output slit was adjusted to 2 mm, which corresponds to a FWHM of approximately 8 nm around the computer controlled central wavelength. To make the output of the monochromator uniform, as well as to compensate for any polarization, an integrating sphere was used. The input polarization state generator was a rotating polarizer (Newport 10-LP-VISB) on a controlled rotational stage.

The intensity of the tungsten–halogen bulb remained constant through the experiment. The monochromator changed the wavelengths from 400 to 800 nm in steps of 10 nm. At each wavelength, the input polarizer rotated from 0° to 175° in steps of 5°. The sensor then captured 64 images at each incident AoP and wavelength.

4.3 Analysis

4.3.1 Pixel Response

The average pixel response to the rotating polarizer is shown in Fig. 4.4, using the data taken at 570 nm with the monochromator setup from Subsection 4.2.3. The solid curve shows the reconstructed cosine, using the amplitude, phase, and offset computed from the Fourier transform over the 0° to 175° sweep. The dots show the average measured intensity at these sample points, and the error bars show the spatial deviation across the whole array at this point. The typical pixels at each orientation, 0°, 45°, 90°, and 135°, display a response consistent with Malus's law for crossed polarizers at those angles. The pixel responses are not matched across the array, as each orientation shows a different transmission and extinction ratio. Figure 4.5, computed as the phase of the Fourier transform of the input filter response, shows that 99.9% of all four filter orientations are within 1.5° of their expected value.

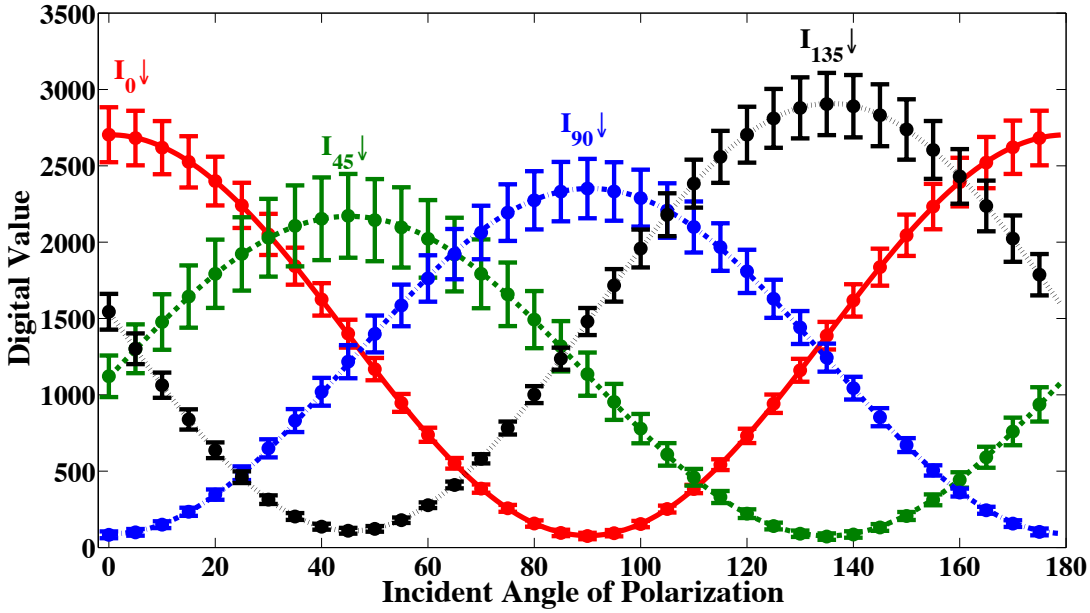

Figure 4.4: Average filter response across pixel array, λ = 570nm. Bars indicate spatial standard deviation.

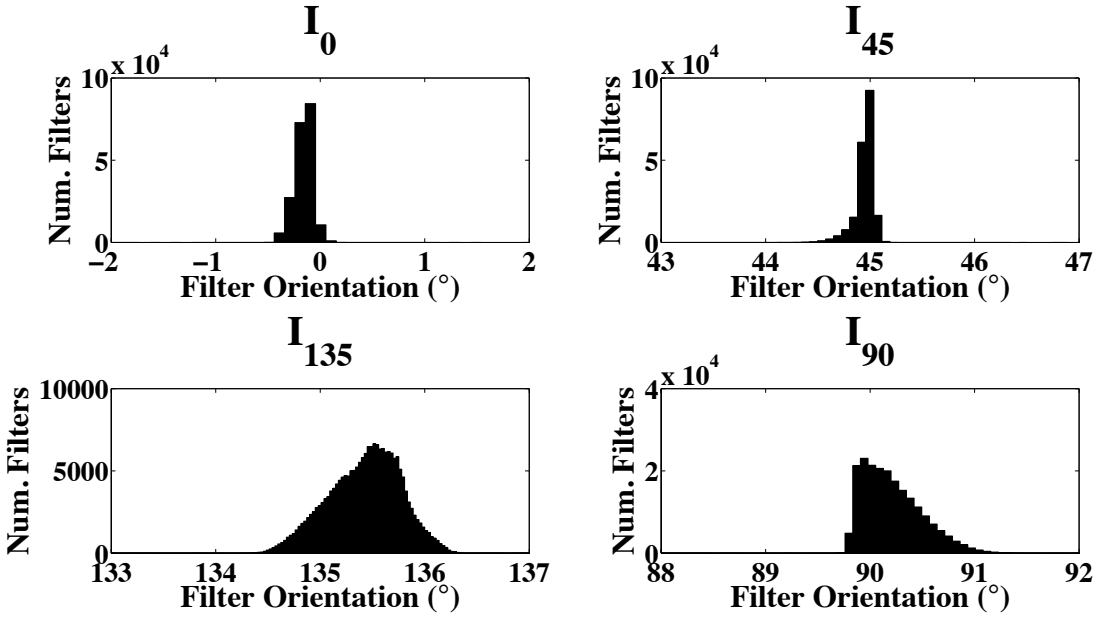

Figure 4.5: Filter orientations

The mismatch in the response results mostly from the fabrication process used for the filters. The nanowires, which are the basic building block of the filters, have variations in height due to uneven metal deposition, variations in the width and pitch due to variation in the

interference lithography, and variation in the height, width, and pitch from un- even etching during the RIE/ICP stage of fabrication. The variations are difficult to measure using SEM or TEM microscopy due to the large area occupied by the microgrid. The collective variation affects the optical response of the array, which is seen in the data presented here. In order to obtain accurate polarization information from this sensor in terms of the first three Stokes parameters, the DoLP, and/or the AoP, the individual response of all pixels should be calibrated. A method for calibrating this sensor is described in [80].

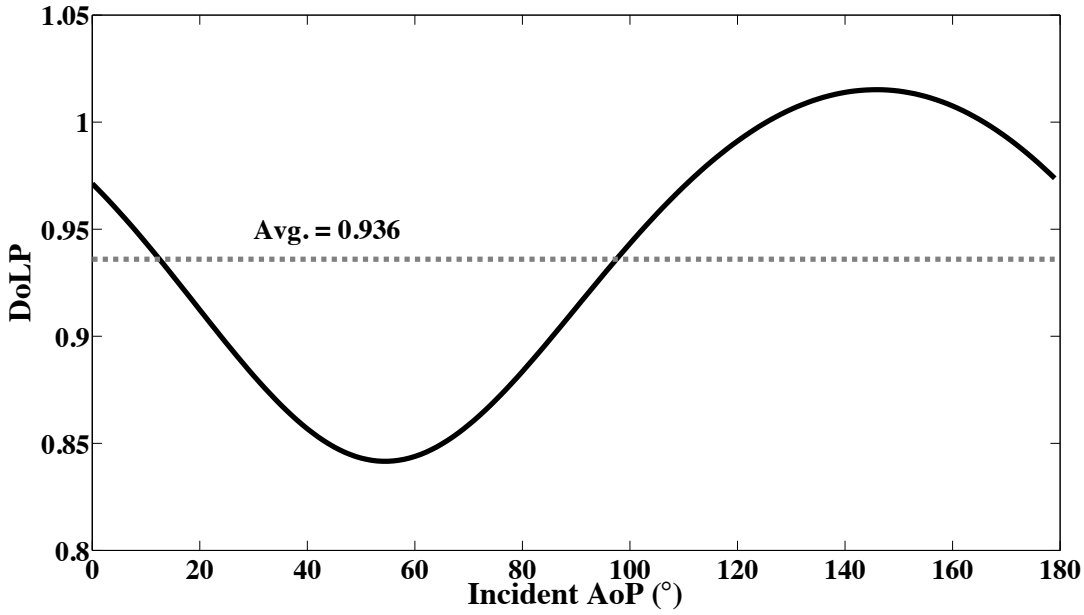

Figure 4.6: Computed DoLP for incident AoPs at $\lambda = 570$ nm.

Using the data from Fig. 4.4, the computed DoLP, shown in Fig. 4.6, exhibits a dependence on the incident AoP due to this mismatch. The phenomenon is illustrated greatly near 45°, since the 45° pixel has a peak transmission nearly $1/3$ lower than that for 135°, degrading S_2 and lowering the computed DoLP from its true value. Figure 4.7 is a sample frame taken from the setup described in Subsection 4.2.2. It was captured at 650 nm, with a DoLP at

roughly zero, and shows the frame split according to filter orientation. The black spots in Fig. 4.7 are dust specs that are introduced during the nanofabrication procedure of the pixelated polarization filter array. The filters at 45° clearly show more degradation than the other three, due to their fabrication. Figure 4.7 also illustrates why the sensor has more error for lower DoLPs, with a histogram of the measured intensities shown in Fig. 4.8. To measure a DoLP of zero, the four filters should show nominally the same intensity. The intensity measured with the 135° filters is brighter than that for both 0° and 90°, which are both brighter than that for 45°, causing nonzero S_1 and S_2 terms. Figure 4.9 is taken from the data in Subsection 4.2.1. It further illustrates the mismatch, showing the variation of the extinction ratios even in a small 200 × 200 pixel window. Both figures illustrate the usefulness of flat field correction for the transmission coefficients, a step not performed here.

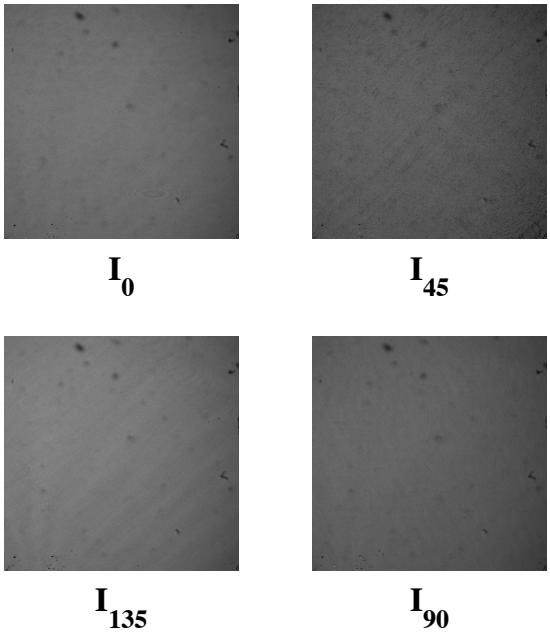

Figure 4.7: Captured frame at 650 nm, input DoLP at approx. 0.0.

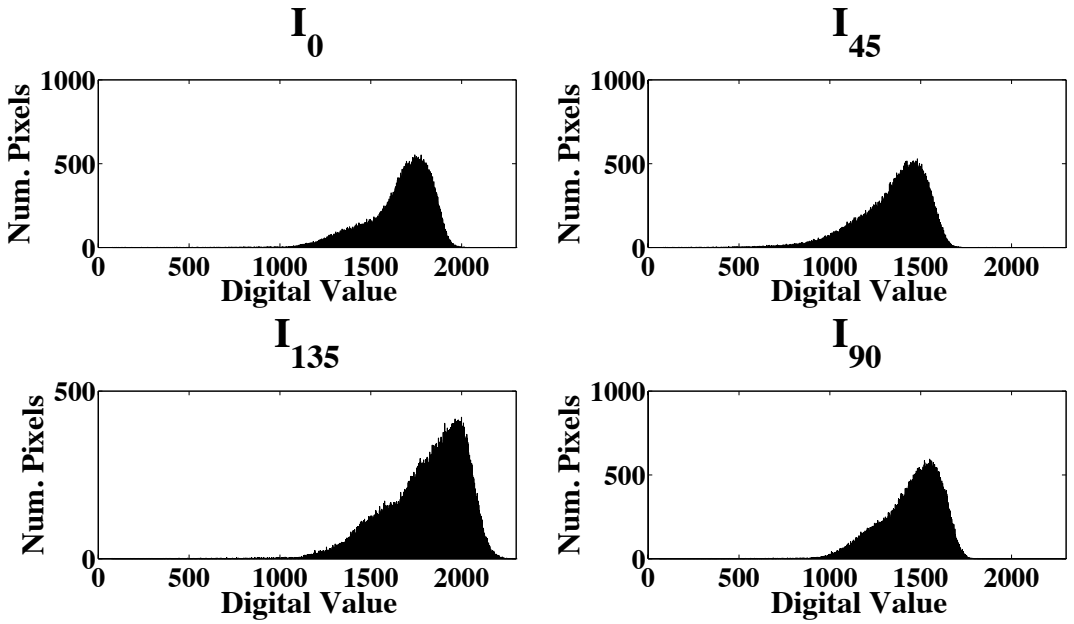

Figure 4.8: Histogram of intensities at DoLP of approx. 0.0

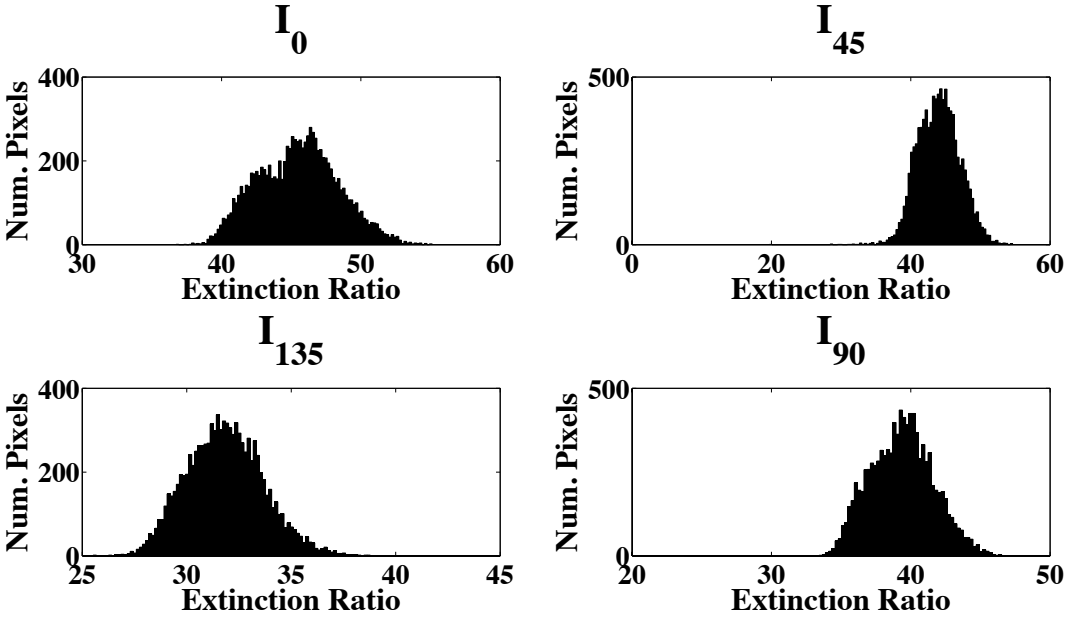

Figure 4.9: Histogram of extinction ratios in 200x200 pixel neighborhood

These effects influence the computed AoP as well. Figure 4.10 shows the linearity of the computed AoP for the same data. The measured AoP exhibits a mostly linear response, with a

linearity error of 1.977%. The RMS error of the AoP at this wavelength is 3.56°. Equation (4.4) explains the source of the error and is the computed AoP using the four analyzer filters.

$$AoP = \frac{1}{2}\left[\frac{\left(p_{x,45}^2 - p_{x,135}^2 + p_{y,45}^2 - p_{y,135}^2\right) + \left(p_{x,45}^2 + p_{x,135}^2 - p_{y,45}^2 - p_{y,135}^2\right)\sin(2\theta)}{\left(p_{x,0}^2 - p_{x,90}^2 + p_{y,0}^2 - p_{y,90}^2\right) + \left(p_{x,0}^2 + p_{x,90}^2 - p_{y,0}^2 - p_{y,90}^2\right)\cos(2\theta)}\right] \quad (4.4)$$

It assumes ideal, linearly polarized light at angle θ with no retardance, a close approximation to the experimental setup. The error in the computed AoP comes from the mismatch in the transmission coefficients of the analyzer filters. If they are matched, the $p_{x;\theta}$ and $p_{y;\theta}$ terms cancel, leaving the AoP of θ equal to θ. The mismatch may be corrected through the use of a calibration routine [80], [81], which is covered elsewhere. The AoP also shows no sensitivity to different light levels, as shown in Fig. 4.11, taken from the data in the experiment from Subsection 4.2.1.. Since Eq. (4.4) contains no intensity component, the AoP should show no dependence on the incident light value, up to the noise floor of the sensor. This is important, for as one observes the AoP of the scene, either changing the integration time to increase the dynamic range or decreasing the incident optical flux has virtually no impact on the estimated AoP.

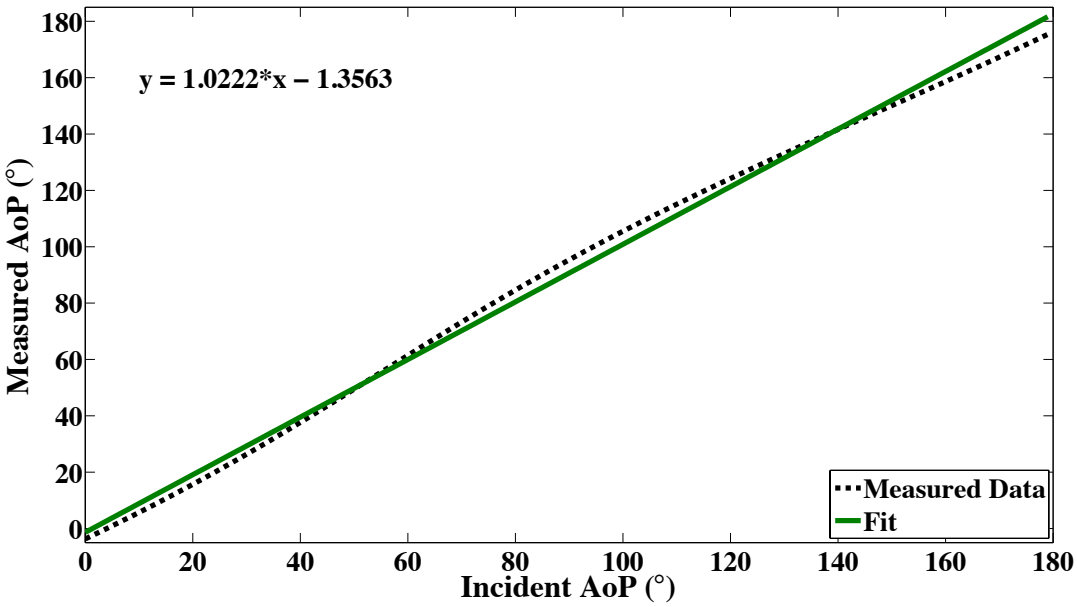

Figure 4.10: Linear fit of AoP at λ = 570 nm.

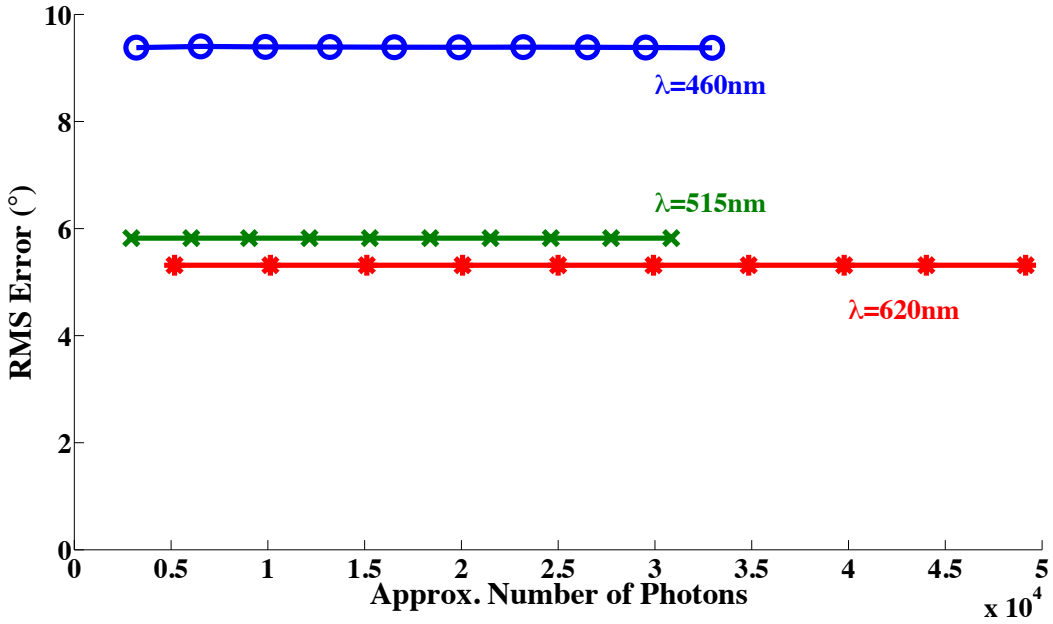

Figure 4.11: AoP RMS error for various photon counts.

4.3.2 Spectral Characteristics

Another property of the sensor is the extinction ratio of the polarizing filters, used here as the ratio of the maximum intensity (∥ polarized) over the minimum intensity (⊥ polarized). The higher the extinction ratio, the greater the range of contrast of the sensor, up to the limits of the pixel technology, mainly the dynamic range and signal-to-noise ratio (SNR). The extinction ratios of a wire-grid polarizer are dependent on the pitch and dimensions of the wire grid [53] and, thus, have a dependence on the incident wavelength of the light. Figure 4.12, taken from the monochromator experiment in Subsection 4.2.3, illustrates this effect for visible wavelengths. At lower wavelengths, near the UV regime (≤400 nm), the extinction ratios are roughly 10 or less. They nearly double as the wavelength increases to around 500 nm, and show a slight continued increase until 700 nm. The de- crease at 700 nm results from an antireflective coating applied as part of the filter fabrication, which attenuates IR wavelengths.

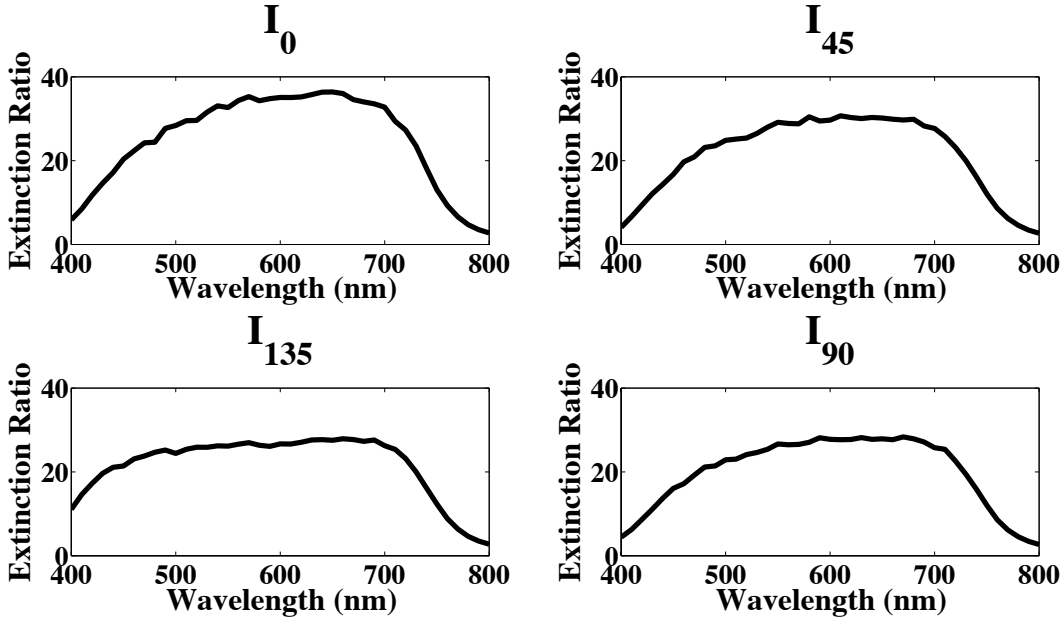

Figure 4.12: Extinction ratio versus wavelength

The extinction ratio sets a direct upper bound on the measured DoLP. Equation (4.5) shows a method to compute the DoLP of an individual filter, using the maximum and minimum intensities for crossed and parallel polarized light. A lower extinction ratio reduces the difference in the measured I_{max} and I_{min}, thus reducing the maximum attainable DoLP:

$$DoLP = \frac{I_{max} - I_{min}}{I_{max} + I_{min}} \qquad (4.5)$$

Figure 4.13 illustrates this phenomenon, showing the average computed DoLP at each wavelength, as per the dotted line in Fig. 4.6. The error bars indicate the spatial standard deviation across the sensor. As the extinction ratios decrease with wavelengths roughly below 450 nm and roughly above 700 nm, so to does the DoLP. The RMS error of the measured AoP, shown in Fig. 4.14 for the swept wavelengths, also indicates that the AoP exhibits a spectral dependence. Since the transmission coefficients depend on the wavelength [53], Eq. (4.4) explains how the AoP has this dependence.

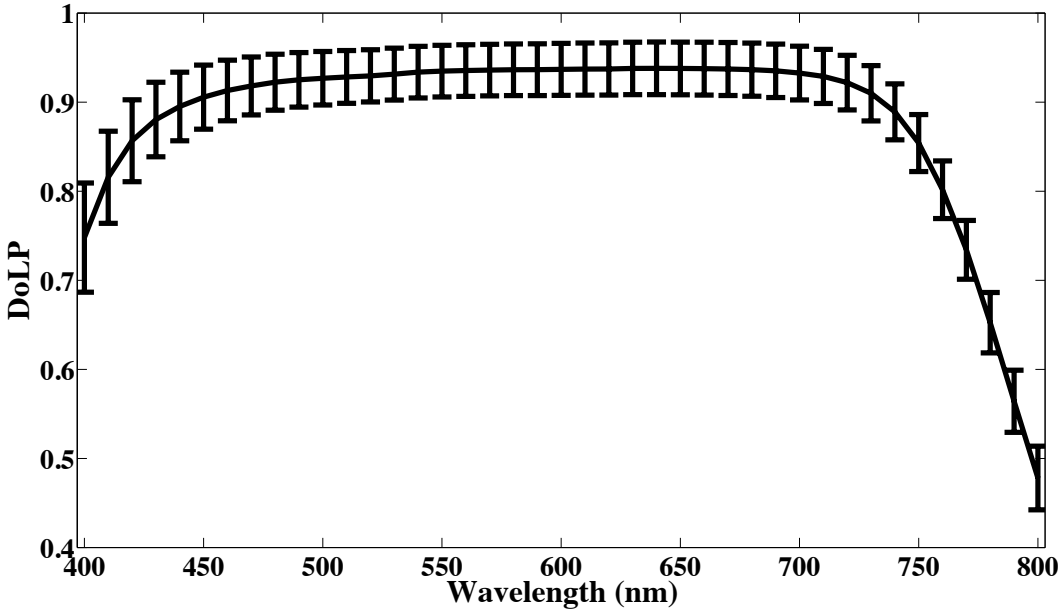

Figure 4.13: Degree of linear polarization over the visible spectrum. Bars indicate spatial standard derviation

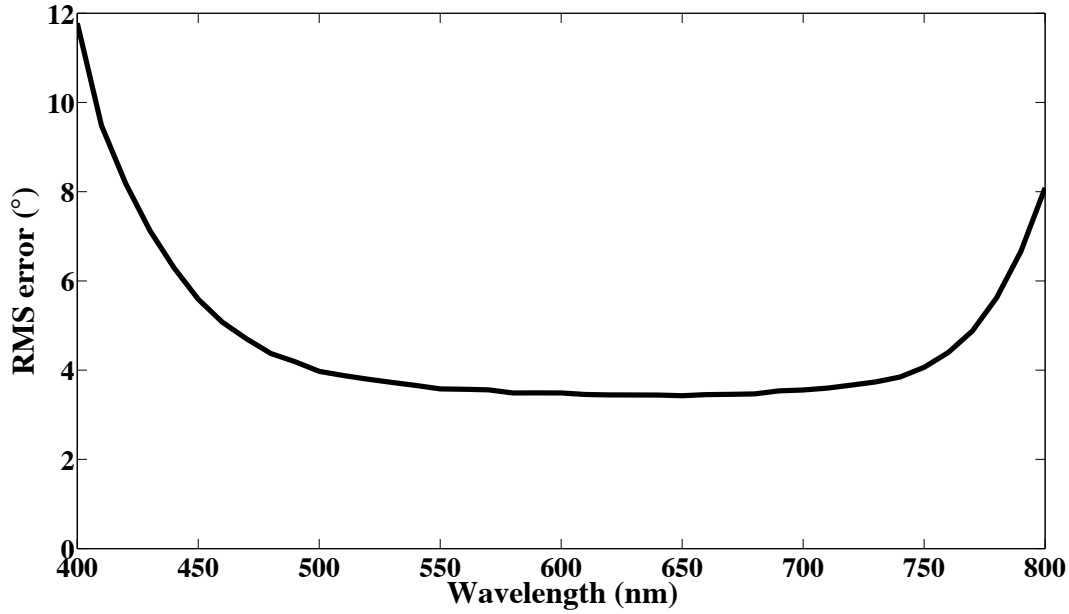

Figure 4.14: RMS error of AoP for visible wavelengths.

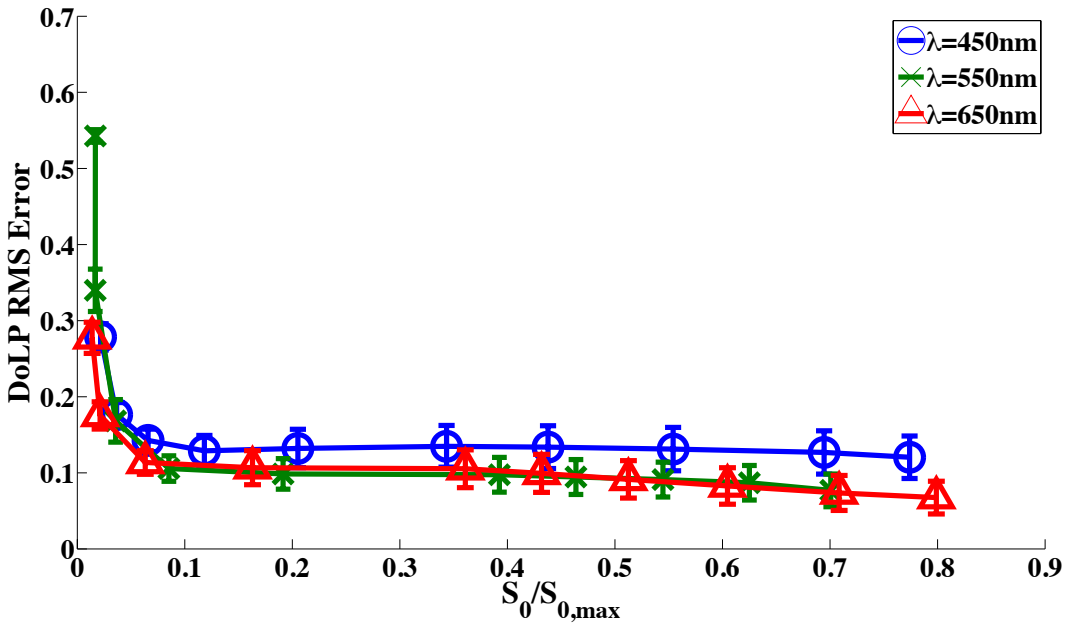

Figure 4.15: RMS error of DoLP for different wavelengths and intensities. Bars indicate spatial standard deviation.

In addition to the extinction ratio, the incident intensity can also impact the computed DoLP. Figure 4.15, taken from the data in the retarder experiment described in Subsection 4.2.2, shows the RMS error of the measured DoLP when compared to the reference, taken for different wavelengths and intensities. Figure 4.16 shows an example linear fit from the experiment, indicating that the output DoLP has a mostly linear response, with the mismatched filters introducing corruption at lower DoLPs. The spectral response of the DoLP tracks Fig. 4.13 closely, showing higher error for 450 nm and roughly the same error for 550 nm and 650 nm. The intensity affects the error primarily at very low intensities, due in part to the S_0 term in the denominator of Eq. (4.2). As the intensity gets smaller, S_0 gets closer to zero, inflating the DoLP. The SNR of the underlying pixels is also reduced at lower intensities (Fig. 4.17), reducing the contrast measured by S_1 and S_2 and increasing the error. At these lower intensities, the sensor is limited by thermal noise in the readout electronics. At higher intensities, the sensor is shot noise limited. The maximum SNR is about 40 dB, and the dynamic range is about 65 dB [2].

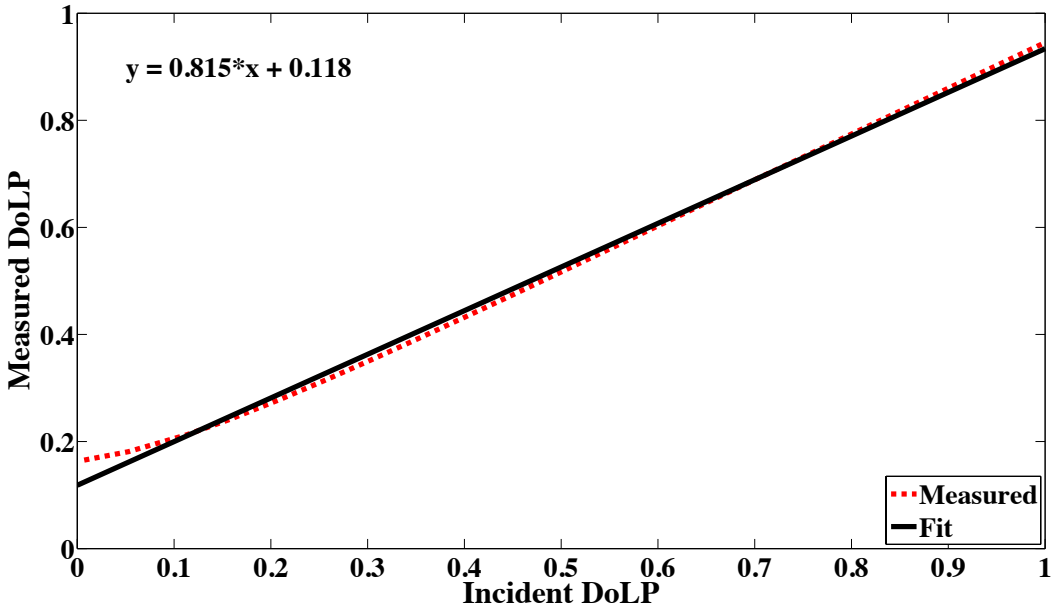

Figure 4.16: DoLP sensitivity, λ = 650 nm.

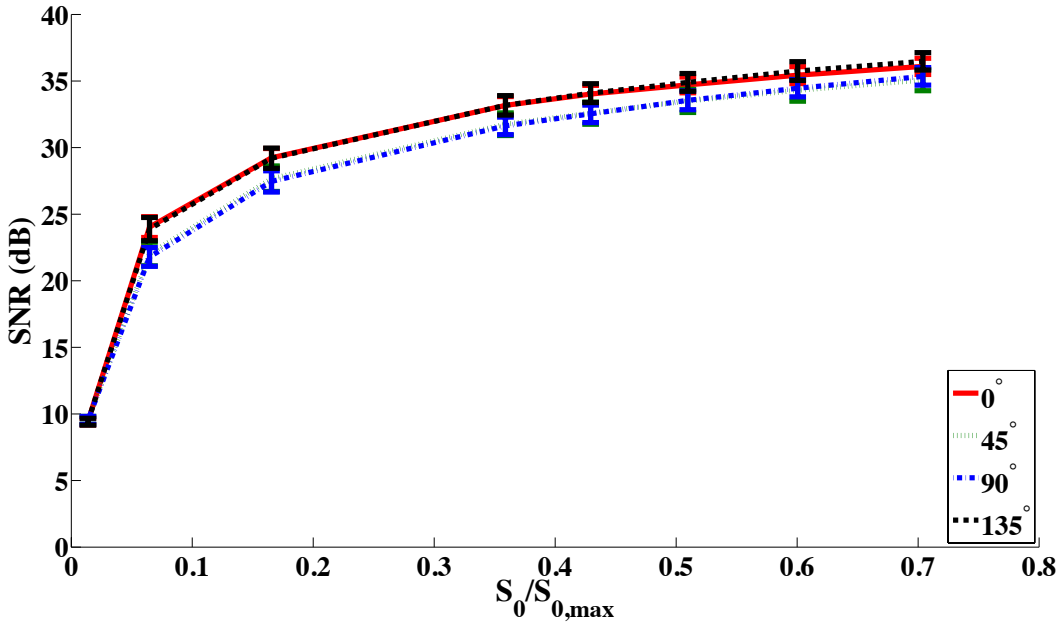

Figure 4.17: SNR of array, split by pixel orientation, λ = 650 nm. Bars indicate spatial standard deviation.

4.3.3 Impact of Divergent Light

The experiment described in Subsection 4.2.1 allows investigation of the effects of divergent light on the sensor. These effects have a great impact on the selection of a lens used in real world imaging. Shorter focal length lenses typically have wider fields-of- view, which means increased incident angles on the focal plane. For example, a lens with a field-of- view of 30° would introduce incident angles of ±15° on the periphery of the focal plane. Based on Figs. 4.18 and 4.19, such an orientation has appreciable error in both the DoLP and AoP. These effects mean the measured DoLP and AoP near the periphery are less reliable than those closer to the optical center. The aperture opening may also play a part, with smaller apertures leading to less divergent light. The reason for this degradation is primarily due to optical crosstalk, where light passes through the filter of one pixel but is registered by an adjacent pixel. Under these conditions, the intensity measured by a pixel is no longer modulated by a single filter, violating the assumption made in Eq. (4.1). Two fabrication techniques could work to mitigate this problem in the future. Backside illuminated pixels reduce the space between the filter and the photodiode and would therefore reduce the likelihood of crosstalk. Pixel matched microlenses [3], common in many current focal plane arrays, also reduce crosstalk by focusing more divergent light toward the photodiode.

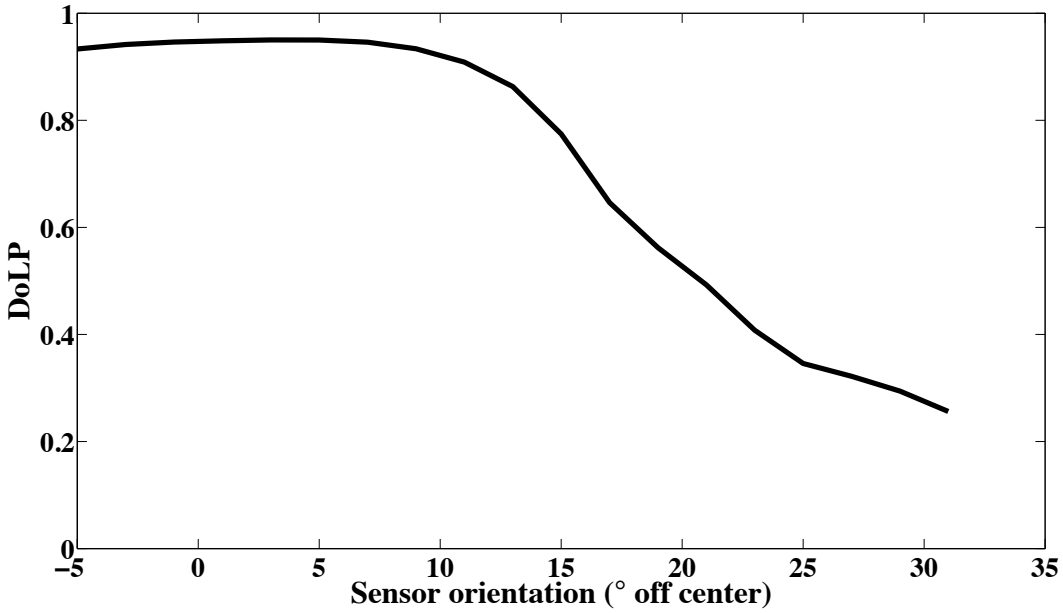

Figure 4.18: DoLP as sensor changes orientation with regard to incident light.

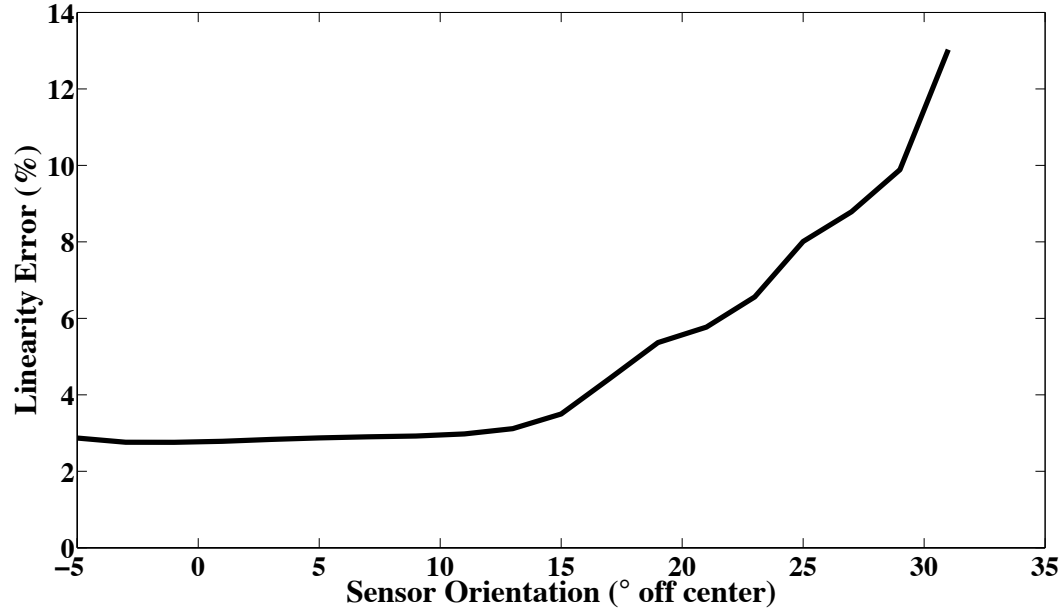

Figure 4.19: AoP error as sensor changes orientation with regard to incident light.

Further, due to mixing from optical crosstalk, the effective extinction ratios decrease. Figure 4.20 shows the average extinction ratios of the four filter orientations, as well as their spatial standard deviation, as the incident light enters at steeper angles. The rapid drop, even after 5° of divergence, clearly shows the impact of optical crosstalk.

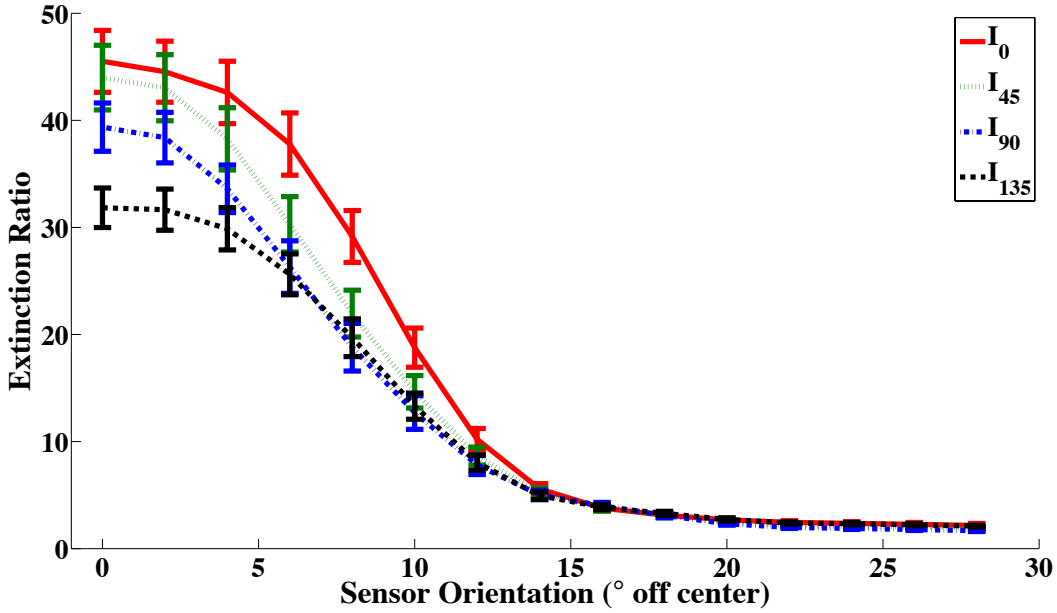

Figure 4.20: Extinction ratio as a function of camera orientation. Bars indicate spatial standard deviation.

4.4 Conclusion

Visible spectrum DoFP polarimeters allow the estimation of the DoLP and AoP at high spatial and temporal resolution in a compact, rigid design. A variety of factors, including the intensity, wavelength, and optical path of the incident light, influence the accuracy of this estimation. Presented here are a formal system of experiments designed to quantify these effects for a DoFP sensor. The experiments give a complete picture of the estimation accuracy of the DoLP and AoP. They illustrate the effects that mismatched analyzer filters have on the accuracy

of the DoLP and AoP estimation. They show how the estimations are functions of the spectrum of incident light, performing worse for shorter wavelengths but remaining relatively constant over the broader visible range. They also demonstrate how important collimation is to reducing optical crosstalk, showing that light divergence is a key limitation to DoLP and AoP estimation. They measured that this degradation from divergence directly impacts the choice of lens, with narrower fields-of-view contributing less error. Finally, they show that the sensor is less accurate for lower intensities, due to a lowered SNR. The experiments presented here allow for an objective means to evaluate and compare DoFP polarimeters. Table 4.1 summarizes the tested sensor's performance.

Number of pixels	1000 x 1000
Pixel Pitch	7.4 μm x 7.4 μm
Frames/s	40
Extinction Ratios	30 (λ = 460 nm) 47 (λ = 515 nm) 58 (λ = 625 nm)
Field-of-view	±ie°
DoLP RMS error	0.120 (λ = 450 nm) 0.077 (λ = 550 nm) 0.067 (λ = 650 nm)
AoP linearity	96.89% (λ = 450 nm) 98.01% (λ = 550 nm) 98.01% (λ = 650 nm)
Signal-to-noise ratio	40 dB
Dynamic range	65 dB
Well depth	20000 e^-
Readout noise	16 e^-
Fill factor	60 %

Table 4.1.Performance Summary of Tested DoFP Sensor

Chapter 5: Biomedical Applications of Polarization Sensors

The emergence of compact, fully integrated polarization imaging sensors has enabled rapid advancements in several biomedical areas. In this section, two biomedical applications are covered, soft tissue stress analysis and label-free optical neural recordings.

5.1 Real-time High-resolution Measurement of Collagen Alignment in Dynamically Loaded Soft Tissue [82]

The study of the biomechanics of tissue is an active area of research [83], [84]. Collagen fibers are the primary component providing structural support for most soft tissues, so observation of collagen alignment can provide insight to how tissues will behave under load and can yield clues to the overall health of the tissue [85], [86]. Such observations lead to a greater understanding of how tissues function in normal loading regimes and throughout damage/failure, knowledge that can be used to help speed recovery, and may even be used to guide the development of engineered replacement tissues. Further, measuring the microstructural arrangement of tissues during periods of loading and rest will lead to a better understanding of the structure-function relationships of a variety of tissue types across many different organisms.

A common method for evaluating collagen fiber alignment in soft tissues observes the change and direction of birefringence under different loading conditions. By illuminating thin, semi-translucent tissue sections between two rotating crossed polarizers, sets of images can be captured and analyzed to produce maps of the direction (i.e., orientation angle) and strength (i.e., relative birefringence) of collagen orientation in these tissue sections [87]–[89]. Alternately, the input light through the tissue may be circularly polarized, with observation through a rotating polarizer providing similar alignment and strain information [90]–[92]. While both techniques

create high resolution strain maps, they are unable to capture the dynamics of tissue alignment with high temporal resolution. Higher speed rotation of the filters increases the speed of image capture, however the tissue must remain static during each rotation period to negate any misregistration error. Further, rotating analyzer polarized light techniques require careful alignment of the rotating filters, which can be a time consuming process. In addition, current techniques are unable to perform real-time assessment of collagen alignment, as they require post-hoc analysis of image sets in order to generate maps of collagen fiber orientation and corresponding angle distributions.

We propose here a new method for measuring the microstructural organization in tissues that does not suffer from these shortcomings. Our method requires only circularly polarized input light, and we use a 1 megapixel, division of focal plane polarimeter to make our observations in real-time, i.e. at 30 frames-per-second. We show that this type of sensor allows real-time capture of collagen alignment dynamics at high spatial resolutions, which will be an extremely useful tool for further studies of tissue biomechanics. Our method is quick, simple, requires no moving optics, and thus does not require a static field of view during measurement.

5.1.1 Birefringence of Soft Tissue

Thin sections of collagen tissue show greater alignment when placed under strain. Since tissue is birefringent along the direction of strain, it can be approximated as a linear retarder whose fast axis is aligned in the direction of strain. The retardation of the tissue is also proportional to the amount of strain. A simple way to measure the birefringence is to observe the tissue through crossed linear polarizers [88]. Any birefringent part of the tissue introduces a phase delay between the x and y electric field components. This introduces an ellipticity in the polarization state, and thus illumination will appear through the set of crossed linear polarizers.

This illumination through crossed polarizes disappears when the polarizers are aligned with the major or minor axis of the birefringent portions of the tissue. Thus to find the true direction of alignment requires a rotation through 180 degrees to solve the ambiguity of which rotation angle corresponds to the major and minor axis. Using circularly polarized light as input requires rotation of only one linear polarizer (called the analyzer) and is sometimes used as an alternative [90].

Mathematically, we can describe this phenomena using the Mueller calculus shown in Eq. 5.1.1,

$$\begin{bmatrix} S_0 \\ S_1 \\ S_2 \\ S_3 \end{bmatrix} = \mathbf{M}_{\mathbf{rot}}(-2\theta)\mathbf{M}_{\mathbf{ret}}(\phi)\mathbf{M}_{\mathbf{rot}}(2\theta)\begin{bmatrix} 1 \\ 0 \\ 0 \\ 1 \end{bmatrix} = \begin{bmatrix} 1 \\ -\sin 2\theta \sin\phi \\ \cos 2\theta \sin\phi \\ \cos\phi \end{bmatrix} \qquad (5.1.1)$$

where $\mathbf{M}_{\mathbf{rot}}$ is the Mueller matrix for a rotation of θ with respect to the analyzer, and $\mathbf{M}_{\mathbf{ret}}$ is the Mueller matrix for a retarder with retardance ϕ when aligned with the analyzer. In this equation, the optical properties of the tissue retardance are captured by the $\mathbf{M}_{\mathbf{ret}}$ matrix. The rotation of the tissue with respect to the fast transmission axis is encapsulated by the two rotation matrices, which are used to transform the co-ordinate system of the retarder with respect to the observer's co-ordinate system. A polarization sensitive imaging sensor will capture the Stokes vector that emerges from this tissue (or a waveplate with retardance ϕ) and the goal is thus to solve for this rotation angle, θ, and for the retardance, ϕ. Solving for these two parameters, namely θ and ϕ requires multiple measurements of the Stokes parameters S_1 or S_2, which is typically accomplished by rotating an analyzer.

If both S_1 and S_2 are known, then this leads to computation of the Angle of Polarization (AoP), which describes the major axis of rotation of the polarized light. Equation 5.1.2 presents the necessary mathematical equations exploring the relationship between the measured angle of polarization and the angle of alignment, θ.

$$AoP = \frac{\tan^{-1}\left(\frac{S_2}{S_1}\right)}{2} = \frac{\tan^{-1}\left(\frac{\cos 2\theta \sin\phi}{-\sin 2\theta \sin\phi}\right)}{2} = \frac{\tan^{-1}(-\cot 2\theta)}{2} = -\frac{\tan^{-1}\left(\tan\left(90^\circ - 2\theta\right)\right)}{2} = -\frac{\left(90^\circ - 2\theta\right)}{2} = \theta - 45^\circ \quad (5.1.2)$$

The alignment of the tissue's fast axis is exactly 45 degrees off of the measured AoP angle. Further, Eq. 5.1.3 shows that the Degree of Linear Polarization (DoLP) is the sine of the retardance. This is because circularly polarized light has a DoLP of zero, so when the retardance is zero, the DoLP will be zero.

$$DoLP = \frac{\sqrt{S_1^2 + S_2^2}}{S_0} = \frac{\sqrt{(-\sin 2\theta \sin\phi)^2 + (\cos 2\theta \sin\phi)^2}}{1} = \frac{\sqrt{\left(\sin^2 2\theta + \cos^2 2\theta\right)\sin^2\phi}}{1} = \sin\phi \quad (5.1.3)$$

Conversely, if the retardance is exactly 90 degrees of phase, then since the input phase difference between the x and y components of the electric field are 90 degrees apart (the definition of circular polarization), the output phase difference will be 0 degrees (or 180), which makes the output light completely linearly polarized. Figure 5.1.1 provides an illustration of the optics used for light generation and analysis.

Since the inverse sine of the DoLP is the retardance, the change in DoLP is proportionally related to the changes in alignment placed on the tendon, as shown in Eq. 5.1.4. As the tendon is

$$\phi = \frac{2\pi b}{\lambda}\Delta n \qquad (5.1.4)$$

stretched, the organization of the fibers becomes more uniformly aligned in the direction of the stretching. This causes a change in both the refractive indices (Δn) and the thickness (b) of the tissue sample. The increased organization will also manifest itself as a decrease in the angular standard deviation.

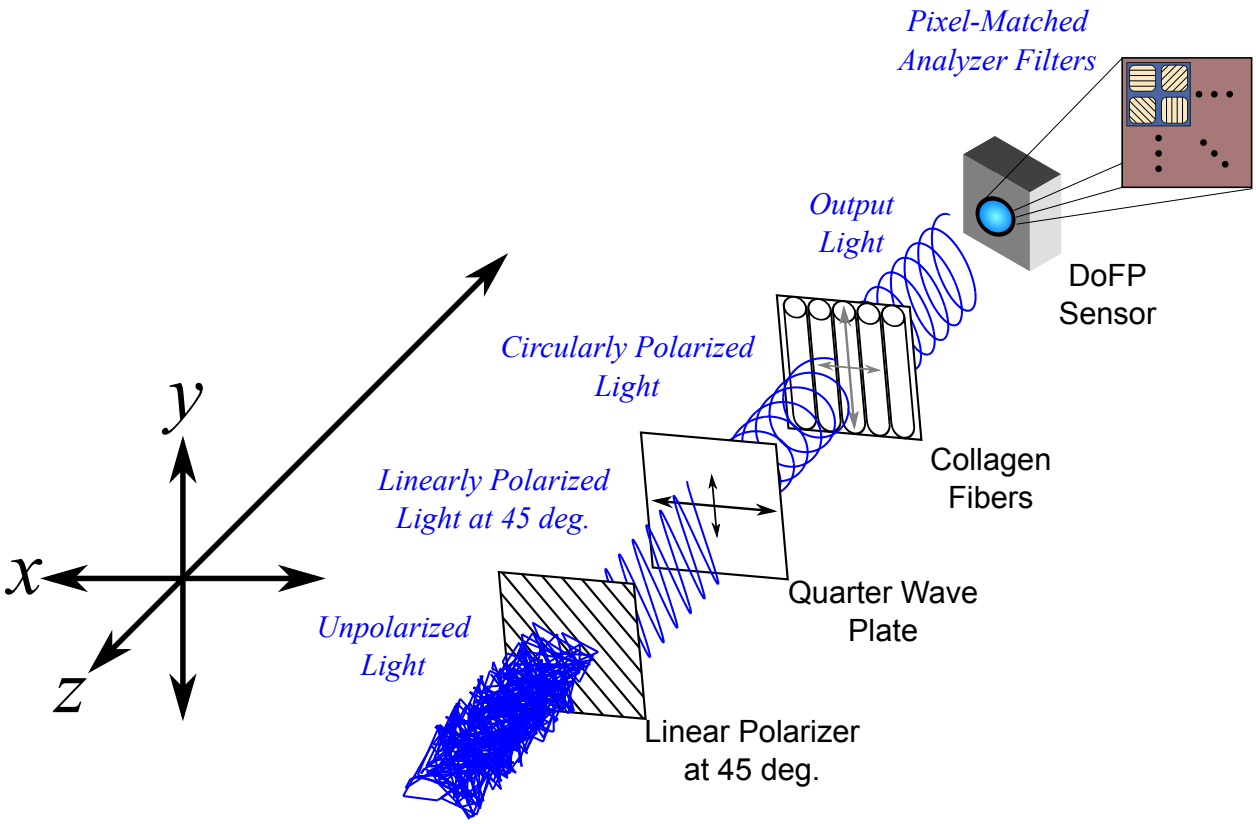

Figure 5.1.1: Optics to measure collagen alignment. The collagen retards the incident circularly polarized light along the direction of fiber alignment.

5.1.2 Sensor Architecture and Experimental Setup

Using circularly polarized input light, a sensor that can instantaneously capture the DoLP and AoP can therefore instantaneously capture the direction and strength of collagen fiber alignment in a tissue. Since this requires capturing the first three Stokes parameters at every frame simultaneously, this necessitates at least three measurements using three different

orientations of linear polarizers. A Division-of-Focal-Plane (DoFP) polarimeter accomplishes this using pixelated linear polarization filters monolithically integrated with an array of CCD imaging elements [2]. The sensor has a two by two neighborhood of pixel matched aluminum nanowire polarizers at 0, 45, 90, and 135 degree orientations. The polarizers are fabricated using interference lithography and reactive ion etching, and the nanostructures in the filter have a width of 70 nm, a pitch of 140 nm, and a thickness of 200 nm. Each of the filters is matched to the sensor pixel size of 7.4 μm^2 pixels, and have extinction ratios on the order of 50 to 60 [2]. Because of this architecture, the sensor captures all the necessary information to measure the DoLP (Eq. 5.1.3) and AoP (Eq. 5.1.2) in a single frame. This is due to the Stokes equation (Eq. 5.1.5), which relates the intensity I, measured by an analyzer that has a linear polarizer at rotation θ

$$I(\theta,\phi)=\frac{1}{2}\left(S_0+S_1\cos 2\theta+S_2\sin 2\theta\cos\phi+S_3\sin 2\theta\sin\phi\right) \quad (5.1.5)$$

degrees and retardance ϕ. Thus for the 0, 45, 90, and 135 degree filters in the DoFP sensor used in this design, the first three Stokes parameters are computed as $S_0 = I(0,0)+I(90,0)$, $S_1 = I(0,0)-I(90,0)$, $S_2=I(45,0)-I(135,0)$. Once the first three Stokes parameters are computed, the DoLP and AoP are calculated, according to Eqs. 5.1.2 and 5.1.3, and thus tissue alignment is quantified within each two by two neighborhood of filters, called a super-pixel. Our sensor is comprised of a symmetric grid of 500 by 500 of these super-pixels. To improve polarization accuracy, we use a per super-pixel calibration Mueller matrix [59]. Since each super-pixel is comprised of four different pixelated polarization filters, interpolation methods are employed to regain the lost spatial resolution and improve polarization accuracy [79], [93]. Bicubic methods measurably improve the modulation transfer function to detect spatial features up to 75% of the full sensor

resolution, while maintaining a low DoLP and AoP error when compared to an unpixelated image.

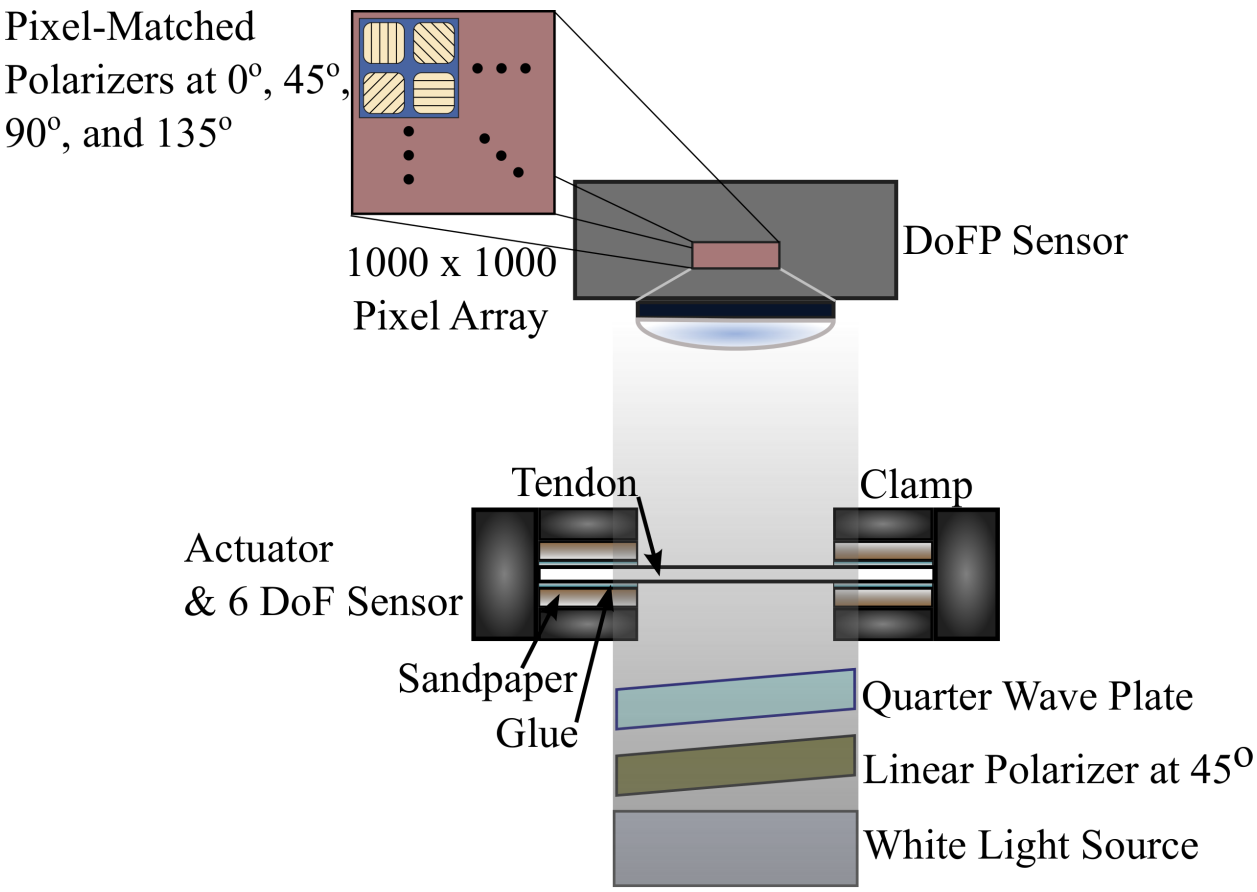

Figure 5.1.2: Experimental setup to measure collagen alignment.

To experimentally measure fiber orientation, we used the DoFP imager with a 16mm, fixed focus lens (Fujinon HF16HA-1B) to view a bovine flexor tendon mounted on a computer controlled actuator and six degrees-of-freedom (DoF) sensor stage in the setup shown in Figure 5.1.2. We input circularly polarized light using a linear polarizer aligned at 45 degrees (Gray Polarizing Film 38-491, Edmund Optics, Barrington,NJ) with the fast axis of an achromatic quarter wave plate (AWQP3, Bolder Vision Optik, Boulder, CO). We imaged a thin (~300 μm) section of bovine flexor tendon aligned with the camera, at -45 degrees to the camera, and

orthogonal to the camera. Figure 5.1.3 shows the DoLP on top (a-c), and the alignment (AoP) on the bottom (d-f). The images illustrate that with a single capture, the sensor is easily capable of accurately measuring the direction and strength of alignment in the tendon specimen.

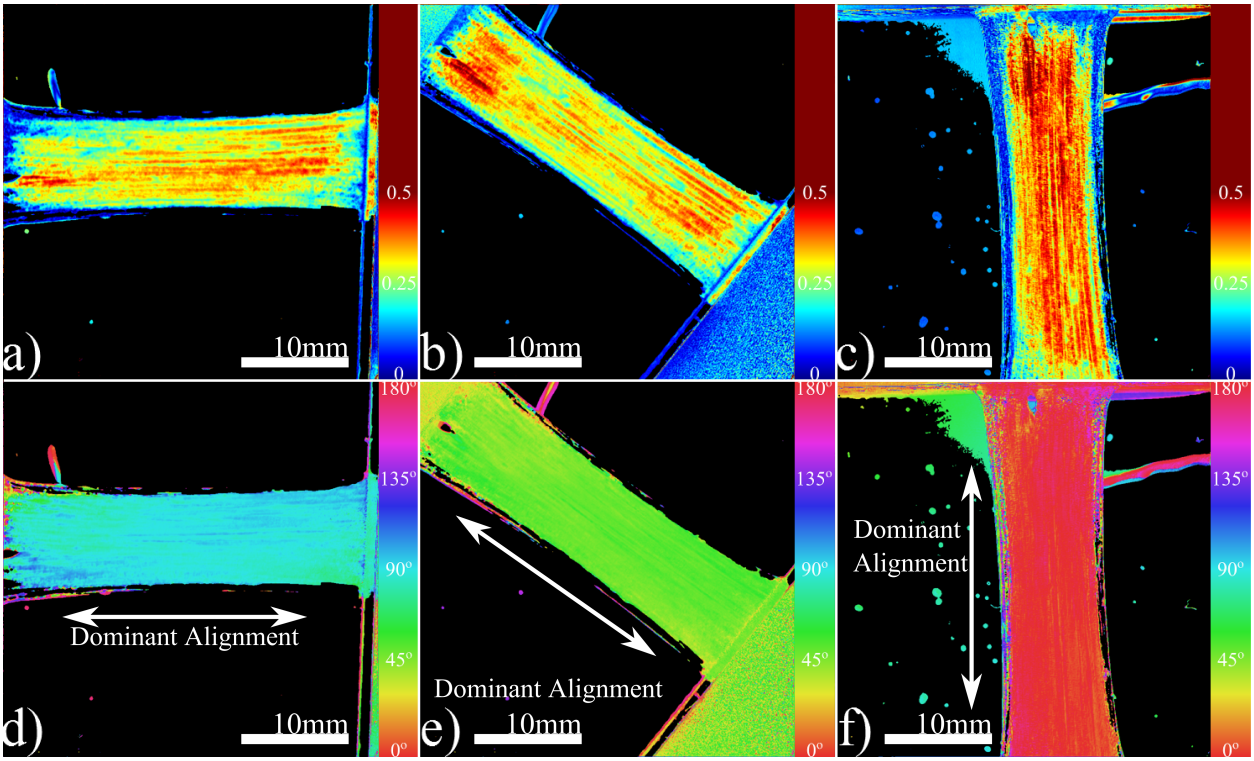

Figure 5.1.3: Tendon under load at different orientations to the sensor, DoLP (top,a-c) AoP (bottom, d-f). The DoLP color bars indicate linear polarization on a scale from 0 (blue) to red (0.5), while the AoP uses a cyclic color scheme to indicate the alignment angle with respect to the sensor.

To validate the new method, we conducted a second experiment comparing our sensor to the standard method of a rotating polarization filter (i.e. an analyzer) in front of a CCD camera with the same pixel pitch as the polarization CCD camera. (Newport 20LP-VIS-B mounted on a Thorlabs NR360 stage, imaged with an Imperx IGV-B1920W image sensor). Starting with a bovine flexor tendon sample subjected to a nominal pre-load, a step strain of 2.5% was applied and held for the duration of the measurements, where the displacement magnitude was computed relative to the gauge length of the sample (measured via digital calipers). We first imaged the

tendon using the rotating polarizer in 15 degree increments and computed the DoLP and AoP (top row, Fig. 5.1.4). While applying the same strain, we then repeated the measurement using our DoFP polarization sensor (bottom row, Fig. 5.1.4). Both image sensors have the same pixel size (7.4 μm by 7.4 μm), and we used the same lens. The results are very similar, except for the DoLP, which is lower for the rotating polarizer. This is due to the error in using a rotating element to measure a non-static scene. Because of significant stress-relaxation of tendon under step-strains, the force is never constant, even over small time periods. Figure 5.1.5 shows an example, where the measured force (shown in black) is not constant in the tissue over time. Using the DoFP sensor, complete measurements of the first three Stokes parameters take place at each green time point, whereas the rotating polarizer only samples an individual angle at each red time point. At a minimum, this requires three separate rotation angles, however significant changes in the force take place during the time of polarizer rotation. The constant downward drift results in differences that are contributed by changes in force, and not by the optical properties of the tissue. Our sensor, with its fixed optics and simultaneous capture of four polarization orientations, does not suffer from this error. This also gives our sensor the ability to sample the dynamics of sudden changes in tissue strain, as in the rapid ramping of the force at the start of the test.

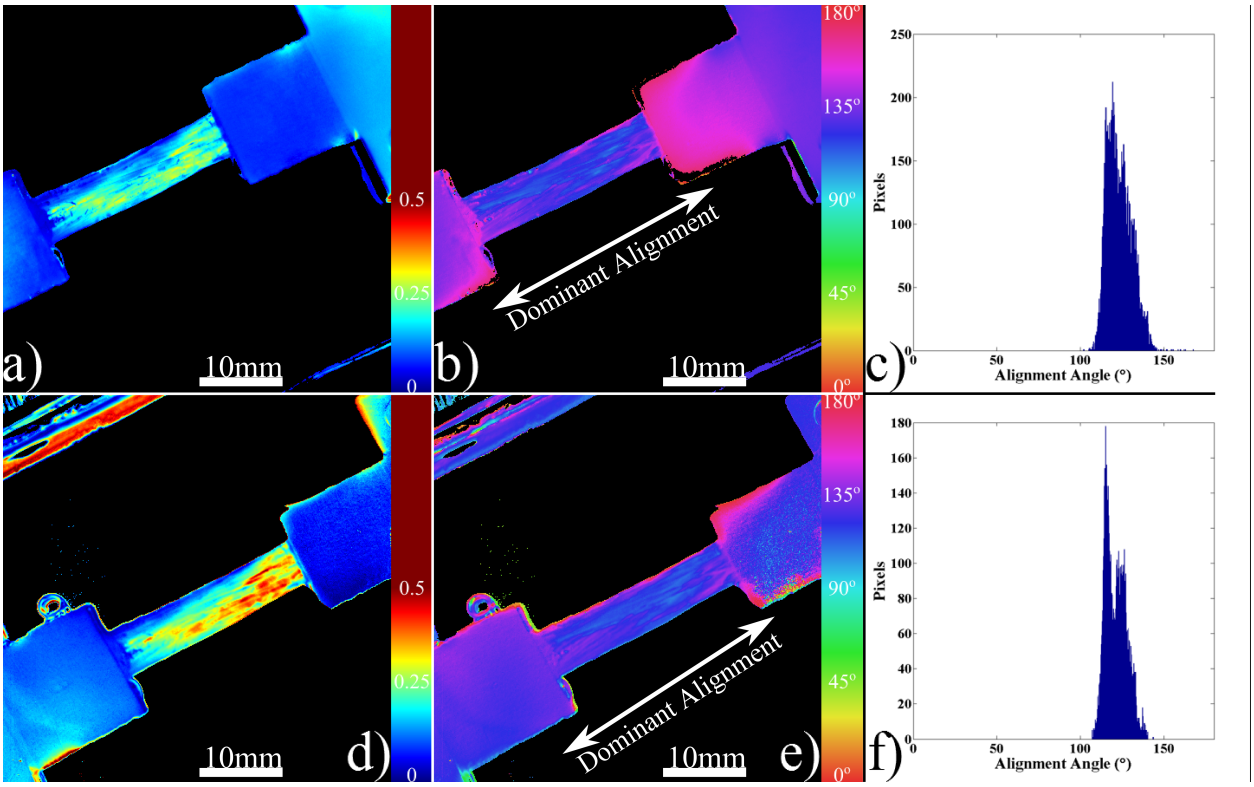

Figure 5.1.4: Measured DoLP (a,d), AoP (b,e), and spread in alignment (c,f) using (top row) a rotating polarizer, (bottom row) division-of-focal-plane polarimeter.. The rotating polarizer measured a dominant alignment of 118.9 degrees, with a spread of 7.05 degrees, with the DoFP sensor measuring a dominant alignment of 122.9 degrees and spread of 6.78 degrees.

Using the same tendon, we then used the DoFP sensor to further investigate measurement of these rapid dynamics, placing the tissue under cyclic loading conditions. We conducted three experiments, cyclically loading the tendon between 2-3% strain at rates of 0.5 Hz, 1 Hz, and 2 Hz. We computed the average DoLP and spatial angular deviation of the AoP over the area of the tendon. The results show that our sensor does very well at picking up the dynamics during loading and relaxation. Figure 5.1.6a compares the retardance and force at 0.5Hz, and Fig. 5.1.6b shows how the spread in the AoP changes during the cyclic load. Under conditions of high strain, the retardance is at the maximum, while the spread of the AoP cycles to the minimum, with the converse happening during periods of low strain. This behavior is expected as the fibers are more aligned when pulled. Figure 5.1.7 shows the same experiment at 2Hz,

demonstrating that our sensor also captures the fiber alignment dynamics at higher loading speeds. In Video 1, we have included a sample of our system capturing the cyclic load at 2Hz. The measurement speed is constrained only by the frame rate of the sensor (maximum frame rate of 30 frames per second), which places an upper bound on the frequency dynamics that the sensor can capture. The real-time nature of the sensor allows for a more thorough frequency analysis of the loading signals. Figure 5.1.8 shows the frequency spectrum of the force (a) and measured DoLP (b) at 2 Hz, and illustrates that our sensor captures the same frequencies as the reference up to the noise floor. In this case of cyclic loading, the frequency dynamics are fairly simple, but this illustrates the ability of our sensor to enable frequency analysis of more complex loading protocols which have not been possible with the utilization of division of time polarimeters. These could be protocols with more time variance, like higher speed step forces, rapid ramps to failure, and higher rates of cyclic loading, or different directions of loading, such as biaxial tension, compression and shear.

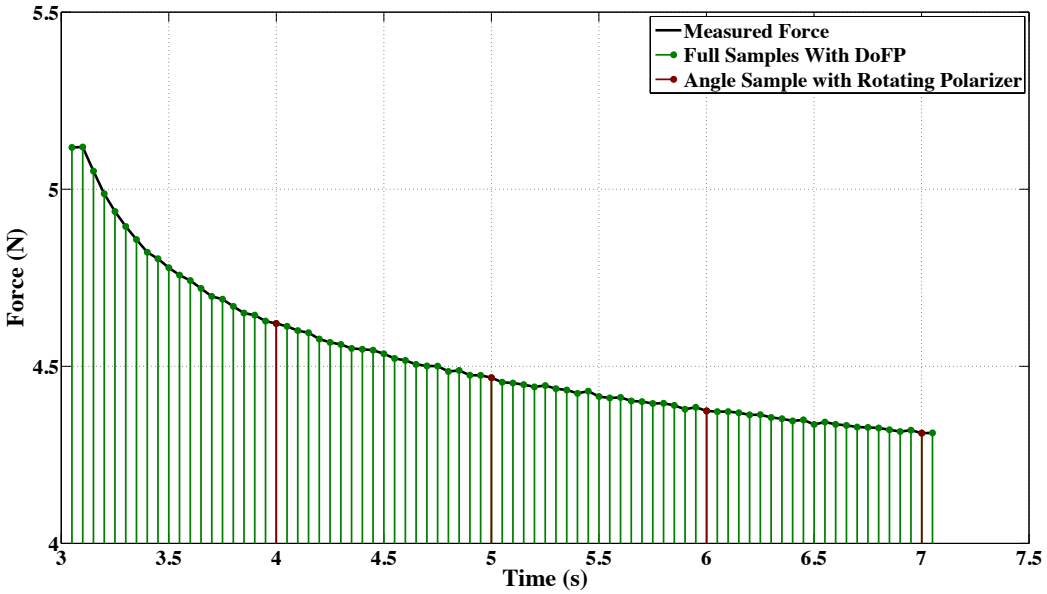

Figure 5.1.5: Timestamped sampling of measured force sampled by the DoFP sensor (green) and rotating polarizer (red). The DoFP sensor can compute the first three Stokes parameters at every green sample point, while the rotating polarizer method requires at a minimum three red sample points. The tissue load is not static during the time taken for these samples, introducing error in measurements using a rotating polarizer.

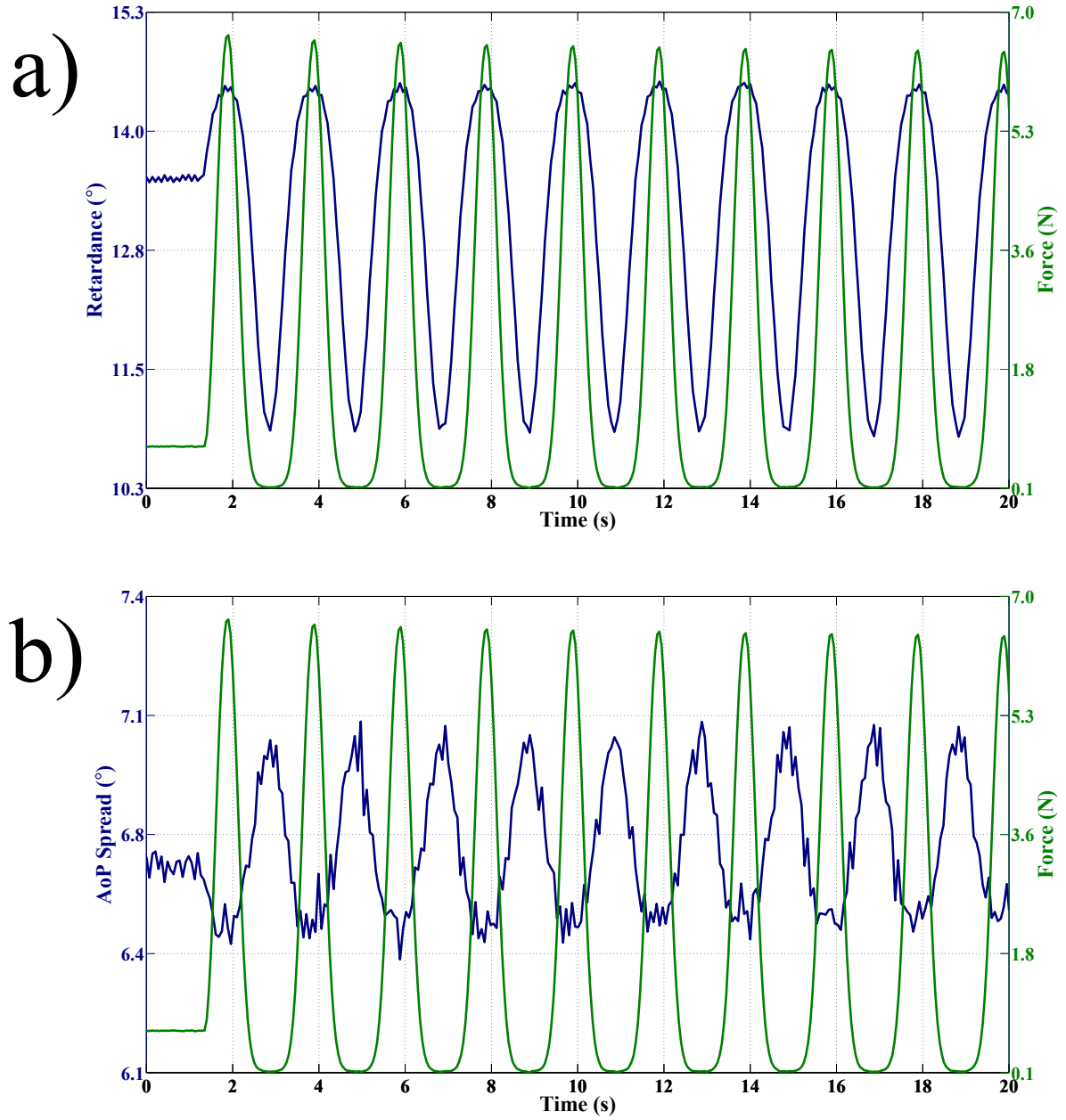

Figure 5.1.6: Measurement of cyclic loading at 0.5 Hz showing the change in retardance (a) and alignment spread (b) measured by our sensor for the tendon compared to the reference force measurement. The retardance is maximal when the strain is maximal, while the spread in the alignment is minimal at the maximum applied strain, due to higher alignment of the fibers under strain.

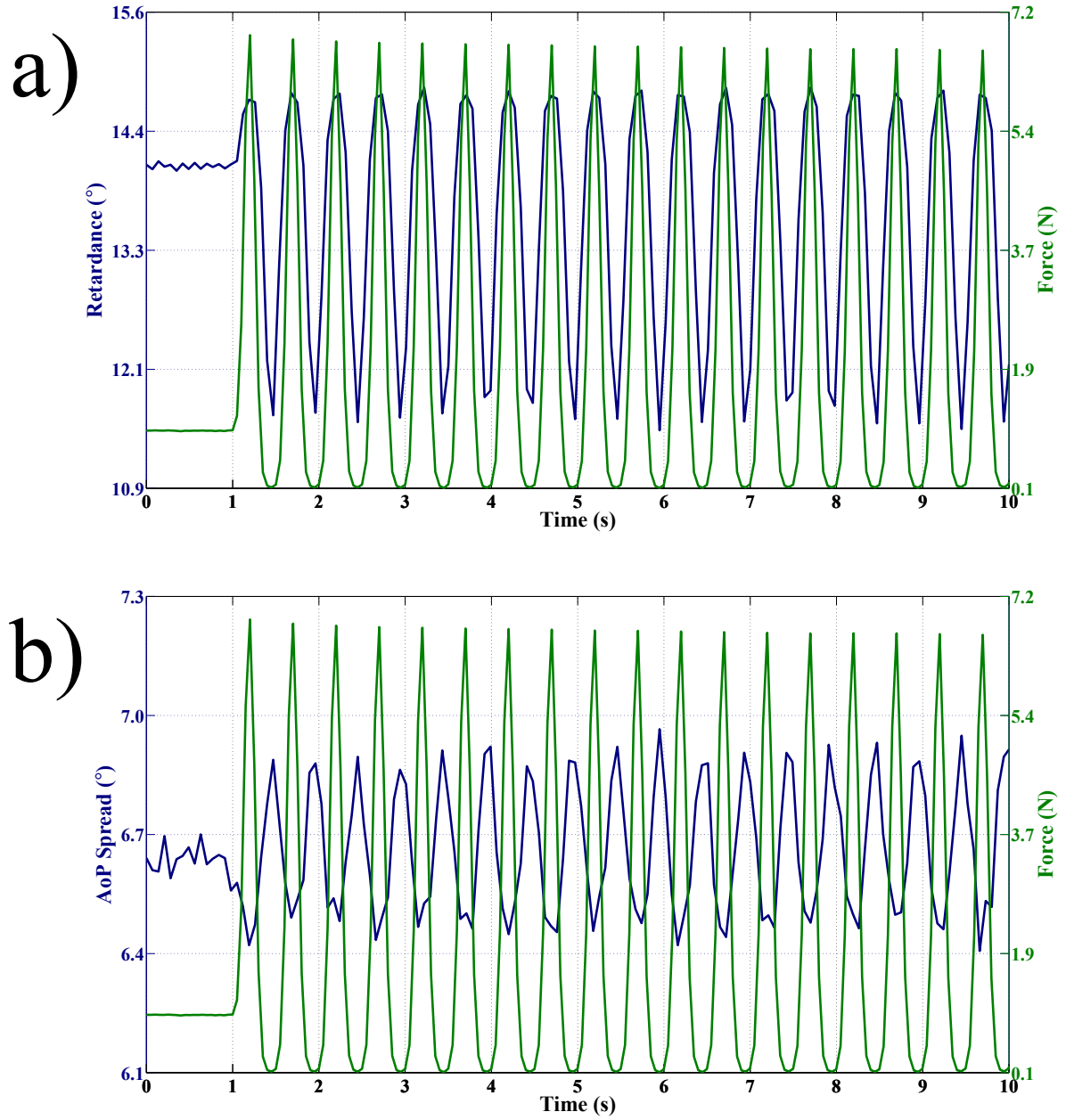

Figure 5.1.7: Measurement of cyclic loading at 2 Hz showing the change in retardance (a) and alignment spread (b) measured by our sensor for the tendon compared to the reference force measurement

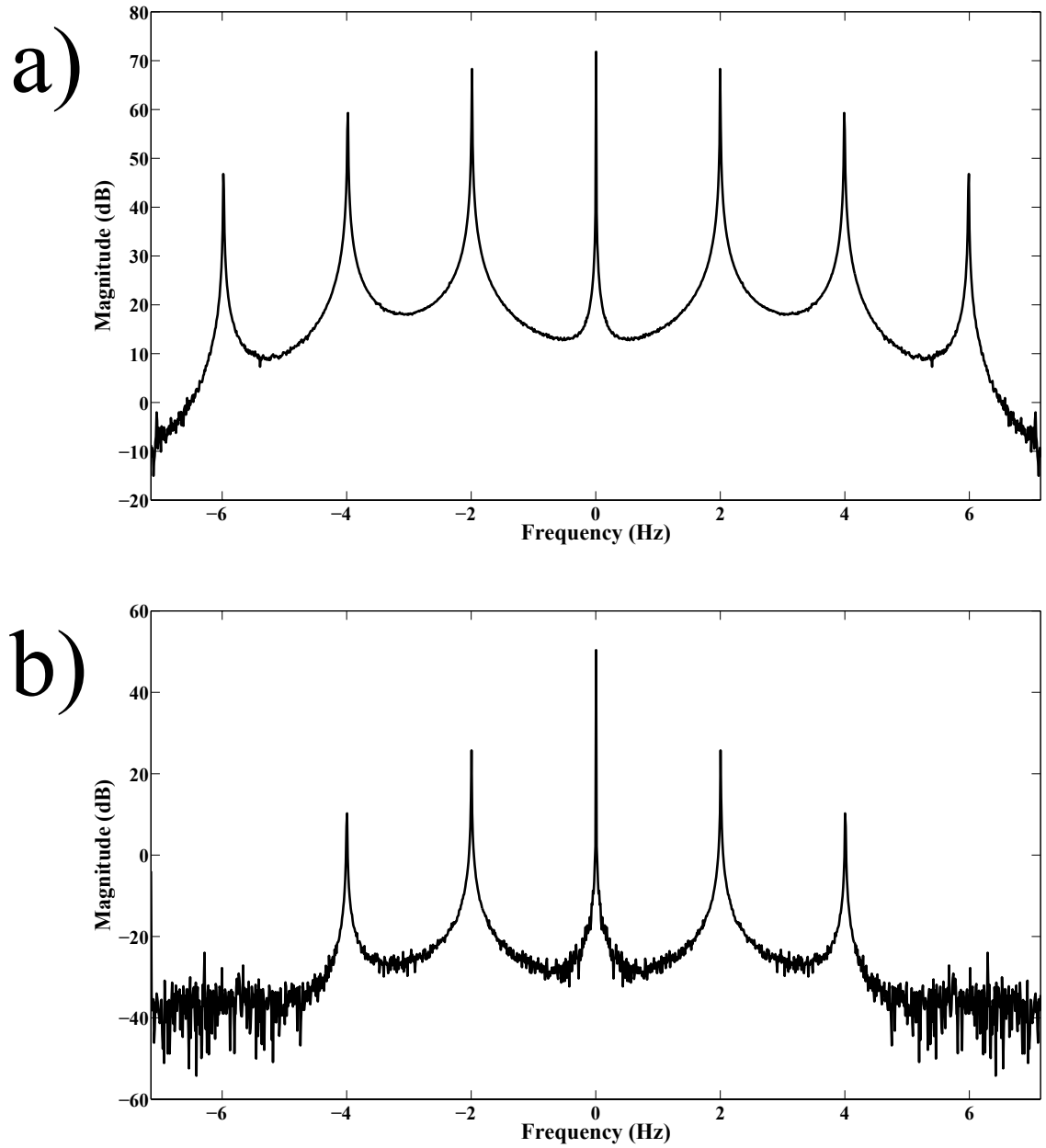

Figure 5.1.8: Frequency spectrum of measured force (a) and retardance (b) of cyclic loading at 2Hz.

5.1.3 Conclusion

We have presented an imaging modality that measures the direction and strength of fiber alignment in soft tissues with both high spatial and temporal resolution. Our system uses a new type of polarimeter designed with stationary optics, which, combined with circularly polarized

input, measures the retardance and alignment of tissue on a frame-by-frame, pixel-by-pixel basis. We successfully demonstrated our method on thin sections of bovine flexor tendon, and showed that our sensor compares favorably with the current methodology, while providing significant additional capabilities and metrics for future analysis.

5.2 In-Vivo Optical Neural Recordings Using Polarization Reflectance [11]

Imaging sensors have greatly advanced the field of neuroscience, especially through the use of fluorescent imaging techniques. These techniques have enabled the *in vivo* capture of neural activity from large ensembles of neurons over wide spatial areas. With Ca^{2+} probes or voltage-sensitive dyes, neuronal action potentials trigger a corresponding optical change. This may change the optical intensity, as when a photon is released upon a transition from an excited state to a ground state. It may also change the spectrum of light during neural activation [94]. Although fluorescent imaging has enabled a tremendous success in the neuroscience field, a number of problems impede further elucidation of neural activity. Many calcium markers require input excitation in the high-energy UV spectrum, which can cause cell damage over time. Additionally, fluorescent dyes may be directly toxic to the cell, or indirectly toxic by interacting with nearby molecules during excitation [95]. Fluorescent dyes also decrease in intensity over time, after repeated excitation and emission cycles, a process called *photobleaching*. Further, some structures in the cell intrinsically fluoresce, overwhelming the measurement of any weaker desired signals.

Two-photon excitation techniques mitigate some of these deficiencies. This technique requires the simultaneous excitation of two low-energy photons to produce a higher-energy fluorescent photon. Two-photon excitation typically focuses a high-power pulsed laser at the

recording image plane. Doing so reduces the background, as a signal requires the simultaneous excitation of two photons, thus increasing the signal-to-noise ratio (SNR) of the neural recording. Additionally, tightly focusing the input beam to increase spot intensity also significantly reduces background photobleaching. Since the excitation wavelength is usually in the near infrared, two-photon techniques allow imaging deeper into tissue than single photon techniques that require UV. These fluorescent techniques, however, can still result in photobleaching over time, reducing the potential for long-term recording experiments.

Alternate optical techniques exist for measuring neural activity. These methods capture the intrinsic changes of light scattered from neural cells without the use of molecular reporters. Because these techniques rely only on intrinsic signals, they will not result in photobleaching after repeated stimulus cycles, allowing for the possibility of long recording periods. Since the signals are optical, they also do not require the introduction of potentially destructive electrophysiology probes for measurement.

State-of-the-art techniques for using polarization to measure neural activity are based on *in vitro* observation of the birefringence change during stimulus. Isolated neural cells are placed between two crossed polarizers and are given an electrical stimulus while optical changes are recorded. During an action potential, the birefringence of the neuron changes, thus causing an intensity change through the crossed polarizer. Initial experiments were performed on squid giant axons, with the SNR of early detection methods limiting them to cultured neurons [96], [97]. More recent experiments have been able to go beyond cultured neurons and use those extracted from lobster (*Homarus americanus*) and crayfish (*Orconectes rusticus*) to show birefringence change during action potentials [98]. Further experiments on the lobster nerve show that the reflection of s-polarized light off the nerve through a p-polarized filter also exhibits an optical

intensity change during an action potential propagation [99]. Since the birefringence changes, it is also possible to use circularly polarized light [100] to detect action potentials. However, all of these in vitro methods have relied on isolated nerves, with most of these methods employing only a single photo detector. A polarization sensor that has multiple detectors, like the one presented here, could simultaneously capture populations of neurons in vivo.

5.2.1 Model of Label-free Neural Recording Using Polarization Reflectance

From the theory covered in section II-B, unpolarized light reflecting off of an object or tissue becomes polarized based on the incident angle and index of refraction. Therefore, if the incident lighting conditions remain the same but the index of refraction changes, this change manifests as a change in the reflected polarization state of light. Neurons during an action potential show a change in the index of refraction [101] and thus should also show a change in the reflected polarization.

Detection of this change can be hindered in the presence of scattering, which causes a decrease in intensity in the direction of propagation. Since neurons typically lay within tissue, the small intrinsic changes in optical intensity that accompany an action potential can be lost. Polarization signals can be more robust to scattering, as evidenced by the use of polarization to see farther in hazy environments [36]. This can be true in tissue as well, with the polarization signal persisting longer through multiple scattering events [102]. This means that detection of the intrinsic polarization signal change might be possible.

If a neuron resides in tissue, then unpolarized light will scatter on entrance to the tissue, reflect off of the neuron, and scatter back toward the camera. The light will be partially polarized upon reflection, and although this polarized reflection will scatter during propagation back to the

sensor, as a polarized reflection it will be less affected by the scattering, making detection possible with a real-time polarimeter.

5.2.2 Optical-based Neural Recording with the Bio-Inspired Polarization Imager

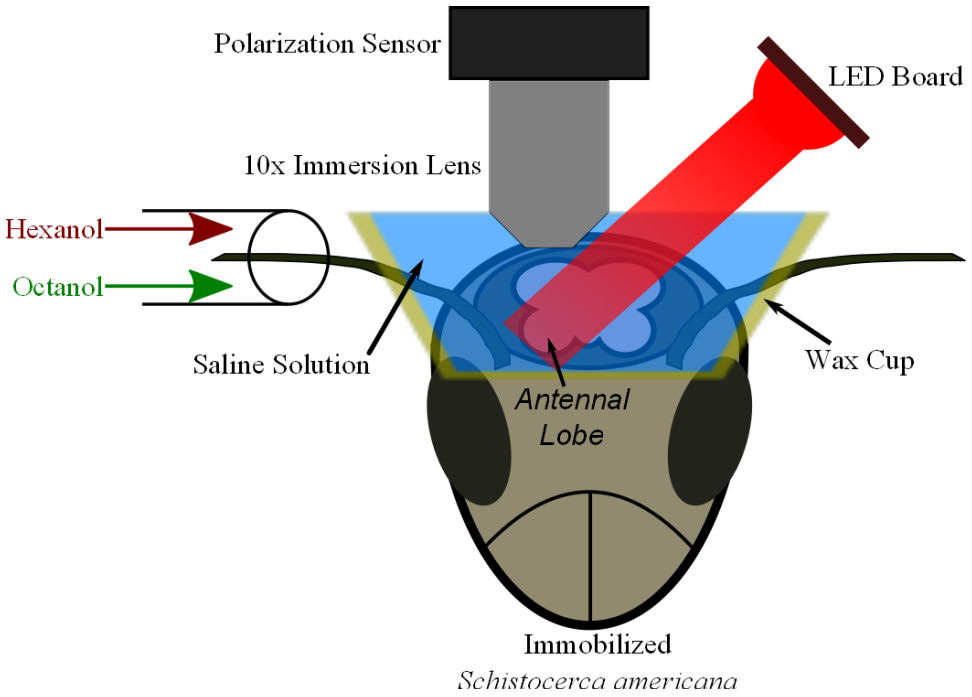

Figure 5.2.1: Experimental setup for in vivo polarization-based optical neural recording.

Figure 5.2.1 shows the setup for optical neural capture [103]. Detection of the optical neural activity was obtained from the antennal lobe of the locust (*Schistocerca americana*). The experiment required exposing the locust brain. To ensure the locust's viability, a wax cup formed a water-tight seal around the exposed area, holding a saline solution [104]. To minimize motion artifacts, the locust was immobilized on a floating optical table. Odors in airflow were introduced to the locust through a plastic tube placed around the antenna at a constant rate of 0.75 L/min. The two odors used in the experiment, 1% hexanol and 1% 2-octanol, were both diluted in

mineral oil. During the stimulation period, odors were introduced at a rate of 0.1 L/min. The airflow is aspirated through a charcoal filter at the same rate of flow around the antenna.

To image *in vivo* the locust's olfactory neurons, the bio-inspired current-mode CMOS polarization sensor was attached through a lens tube to an Olympus UMPLFLN10XW water-immersion objective with 10× magnification. The objective was placed in the saline solution and was focused on the surface of the antennal lobe area of the brain closest to the odor tube. As the focus is on the surface, the frame rate of the sensor in these experiments (20fps) allows detection of the aggregate response of populations of surface neurons. The light source used for the optical recording was a custom circuit board containing ten 625-nm center-wavelength LEDs, powered by a constant-current power supply. A microcontroller synchronized the video frames and a trigger used for introduction of the odor stimuli.

We used two different stimulation protocols for two different experiments. In the first experiment, odors were introduced for 4-s puffs at 60-s intervals. The odors were interspersed as two puffs of hexanol, two puffs of 2-octanol, and two puffs of both odors combined. The sequence was repeated five times. The second experiment used the same 4-s puffs in 60-s increments, but in this case the odors are introduced consecutively as ten hexanol puffs, ten 2-octanol puffs, and ten combined puffs.

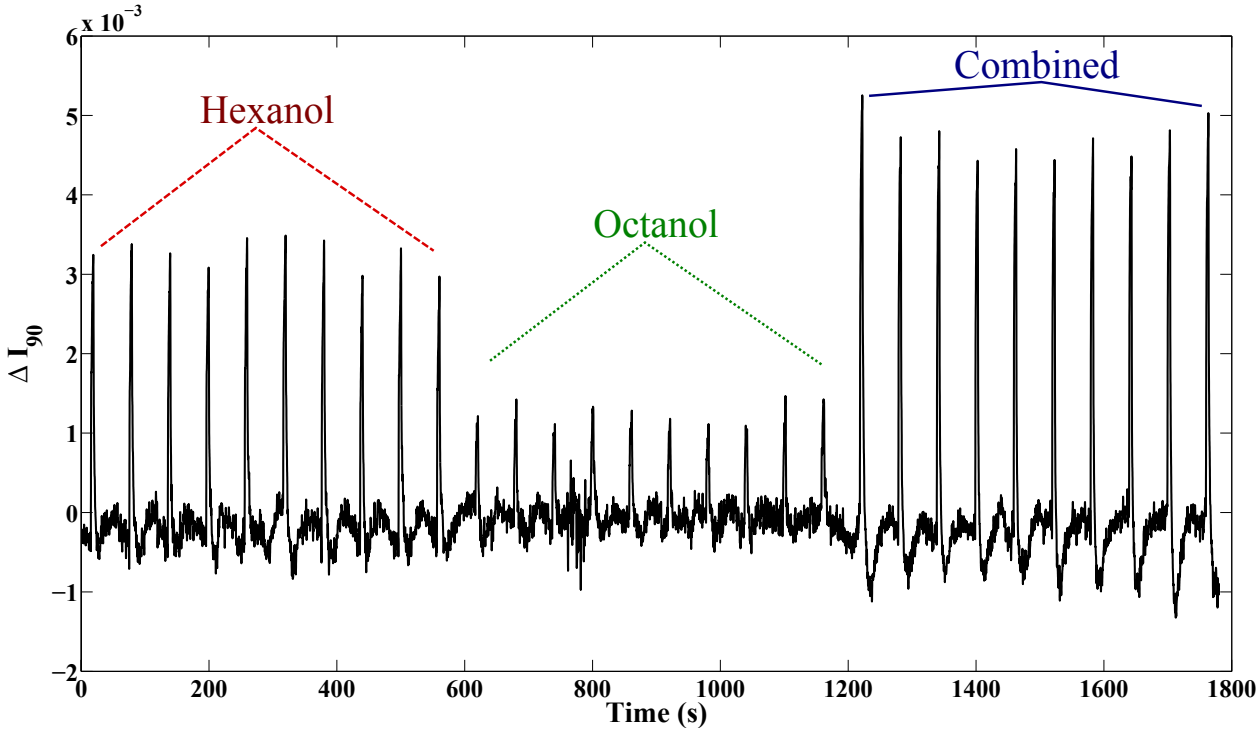

Figure 5.2.2: In vivo measurements from a population of neurons in the locust's antennal lobe. The locust antenna was exposed to series of 10 puffs of hexanol, octanol, or both combined, with each puff lasting for 4 s, followed by 56 s of no stimulus.

The data were filtered using a zero-phase bandpass filter to eliminate high-frequency noise and low-frequency drift. To improve the SNR of the neural signal, the data were also spatially filtered from an 11 × 11 region of pixels within the antennal lobe. Figure 5.2.2 shows the results of the second, 10-puff experiment. The average change for each puff of hexanol was 0.38% ± 0.02%; 2-octanol, 0.15% ± 0.02%; and combined odors, 0.45% ± 0.03%. The stronger response for hexanol over 2-octanol is consistent with electrophysiological data. This trend persisted even for highly interspersed sequences in the first, two-puff experiment (Figure 5.2.3): the average change for hexanol was 0.36% ± 0.06%; for 2-octanol, 0.16% ± 0.04%; and for the combined odor, 0.54% ± 0.02%.

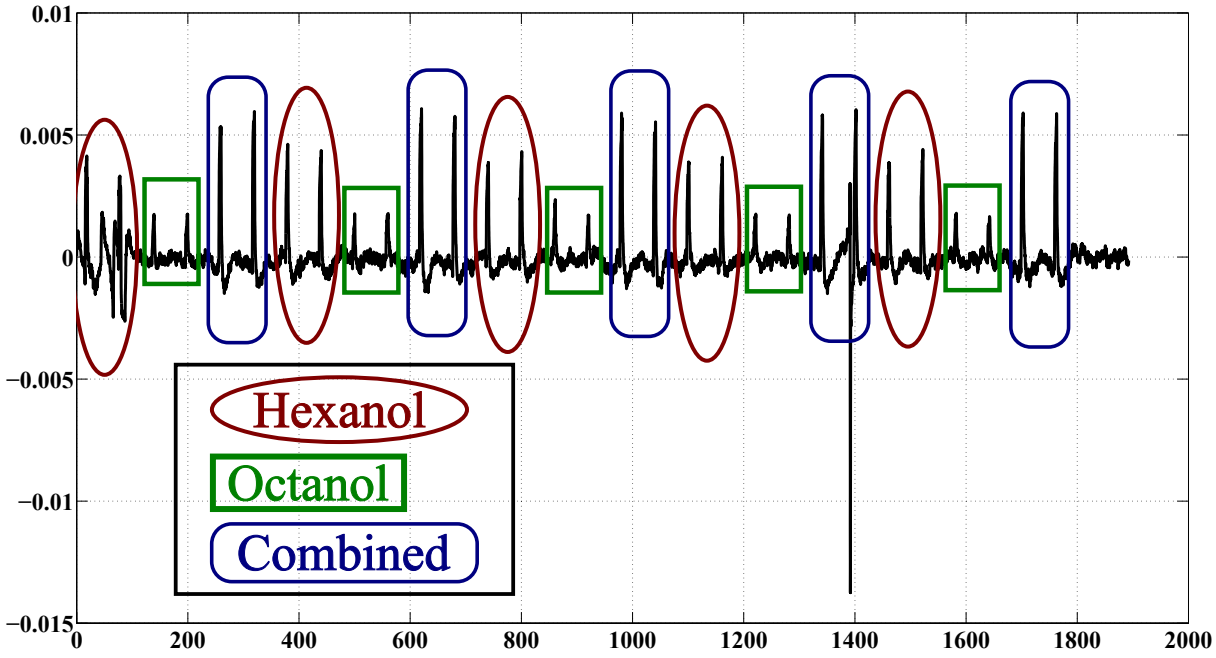

Figure 5.2.3: In vivo measurements from a population of neurons in the locust antennal lobe to highly interspersed odors during the first experiment, comprising two puffs per odor exposure

Figure 5.2.4 presents 2D maps of the neural activation pattern during stimulus presentation with the second protocol. The top row is the neural response to a hexanol puff, the middle row is the neural response to a 2-octanol puff, and the last row shows the neural response to a combination puff of both odors. The 8 different images per row depict the neural activity at a particular time interval indicated at the top of each image.

The activation maps show a response that spreads from the portion of the lobe closest to the antenna, and the source of odor, outward through the rest of the antennal lobe. The images show some similarity to an electroencephalogram, which measures the local field potential near an electrode. The maps show the measurement of the scattering of light changes from the activation of populations of neurons. It has been previously shown that these changes are proportional to the change in voltage potential during activation [97].

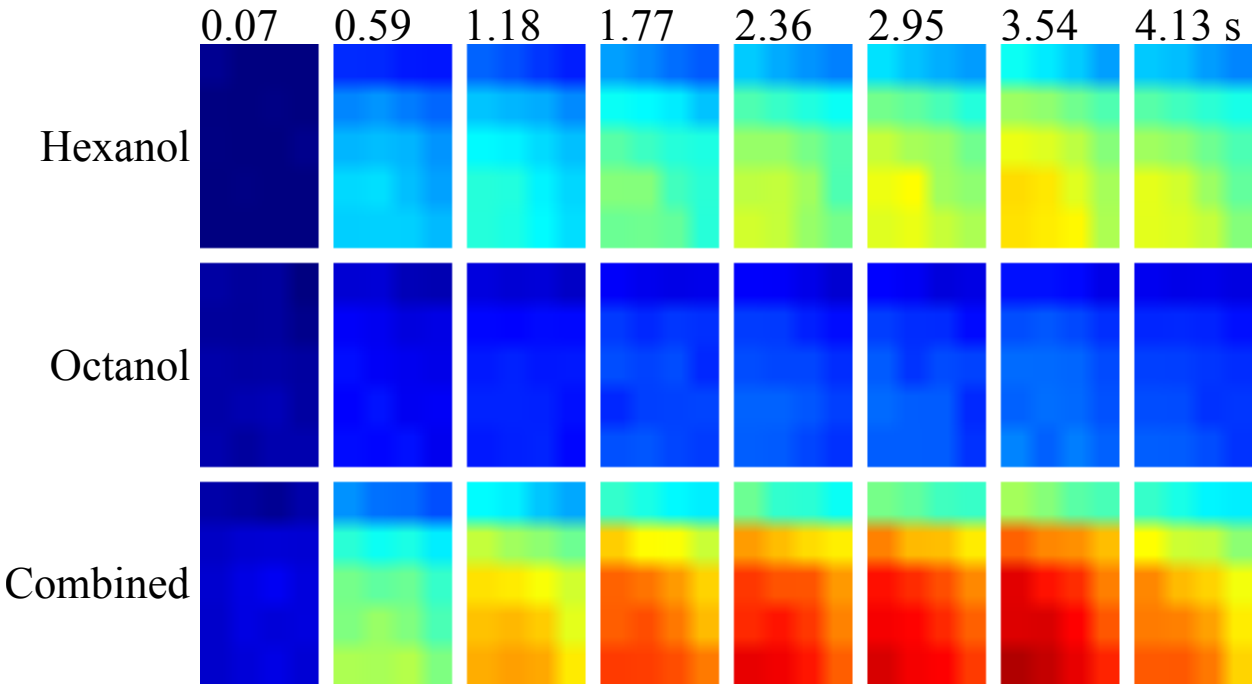

Figure 5.2.4: Spatial activation of neural activity across the locust's antennal lobe. Each 2D map is a dorsal view, with the left as lateral, right as medial, top as caudal, and bottom as rostral. The 8 images per row represent neural activity at particular time intervals indicated at top of each column.

5.3 Conclusion

A 220 by 128 custom current mode image sensor was designed, tested, and fabricated in 0.18 micron CMOS. The sensor has a dynamic range of 56 dB, an SNR of 43 dB, and an FPN of 0.1 %. Post-fabrication,aluminum nanowire polarization filters were deposited on the sensor enabling real time capture of the first three Stokes polarization parameters. The sensor was then used to measure, *in vivo*, the neural activity of a locust (*Schistocerca americana*). The sensor optically recorded differential neural responses to Hexanol, Octanol, and combined stimuli across the antenna lobe without the use of toxic fluorescent markers or damaging electrode arrays.

This new class of compact polarization imaging sensors is opening unprecedented opportunities in the advancement of the knowledge in neuroscience. The possibility of recording

neural activity from a large population of neurons with high temporal fidelity can help in understanding how information is processed in the olfactory system or other sensory systems in the brain. Such questions as how the primary coding dimensions, time and space, are used in biological signal processing can possibly be answered. These imaging sensors can ultimately lead to implantable neural recording devices based on measuring the optical intrinsic signals. The monolithic integration of optical filters with CMOS imaging arrays makes this sensor architecture the only viable solution for implantable devices in animal models, allowing the study of neural activity in awake, freely moving animals.

Further, these types of image sensors have also shown huge potential in studying tissue dynamics. For the first time, real-time, high resolution measurements of tissue dynamics have been recorded This imaging method opens up the possibility of using even more complex loading protocols that require high-speed, real-time measurements (e.g., step and impulse forces), much faster cyclic loading, or high-speed observation of tissue failure. This can lead to better understanding of the mechanical properties of connective tissues, yield insight into structure-function relationships in health and disease, and provide guidance for novel development of orthopedic structures and devices.

Chapter 6: Conclusion

Many modern polarimeters can easily capture the polarization state of light in a given scene. However, these sensors suffer from temporal or spatial resolution problems, have considerable bulk, and are prone to misalignment in field operations. Such issues have limited their usefulness to fields outside of physics and engineering. Therefore, a compact, high-resolution, real-time polarimeter that solves these problems has been developed [2]. This style of polarimeter uses a repeated pattern of polarization filters integrated directly onto the sensor, which allows for simultaneous capture within a small (2x2) pixel area. The complete integration of the filters with the image sensor also ensures a rigid optical setup, with minimal chance of misalignment during field use. Further, as the filter array size is the same as the underlying sensor, this type of polarimeter can be integrated into a relatively compact system, capable of deployment in situations where previous polarimeters would have been infeasible for use. Such a device can be used by specialists and non-specialists alike, potentially opening up the field of polarimetry to much wider use.

The compact, integrated polarimeter introduces new challenges both on the sensor design front, and the optical characterization front. The failure modes of previous polarimeter designs are well understood, however with the new technology comes the new need for understanding where integrated polarimeters fail both electrically and optically. Further, as the direct integration of the optics with the underlying sensor enables new compact designs, evaluation of the fundamental architecture of the sensor becomes a key design consideration. This dissertation has attempted to evaluate these shortcomings and design tradeoffs, in an attempt to develop sensors with the polarization sensitivity and form factor to enable new discoveries in a broad range of fields.

To explore these problems in integrated polarimeter design, this dissertation tried to first answer the question of which image sensor architecture is best suited for compact integrated polarimetry. To accomplish this, it presented a CMOS image sensor capable of operating in either voltage or current mode. It described the architecture of the sensor, including a detailed noise analysis of both reset and readout in both modes. It further illustrated the key advantages and disadvantages with Spectre simulations and measurements from the fabricated sensor. This sensor is further enhanced through the addition of pixelated polarizers, which formed a complete, compact, division-of-focal-plane, polarimeter that operates in current mode.

Secondly, this dissertation presented a complete optical and electrical characterization of an integrated, division-of-focal-plane polarimeter. Using a series of electrical and optical tests derived from theory, it allowed for a complete evaluation of a division-of-focal-plane sensor's performance. These tests evaluated the sensor for spectral characteristics, polarization accuracy, and sensitivity to crosstalk. The tests can potentially serve as standard for evaluation of division-of-focal-plane sensors.

Finally, with the realization of compact, real-time, integrated polarimeters comes the application of these sensors to new areas of research. This dissertation presented two new applications in the biomedical field that are enabled by such a sensor. The first detailed a new method to do dynamic analysis of soft tissue in real-time and at high resolution. Using active illumination, the division-of-focal-plane polarimeter could measure the strength of tissue alignment and the amount of applied strain to soft biological tissues. An example was presented using a bovine flexor tendon, showing how the new method reduced error compared to the standard method. While demonstrated on a simple tissue and load example, the method has the potential to greatly advance the field of tissue analysis. Researchers are no longer limited by

complicated optical setups and alignment issues, nor are they constrained in their selection of loading protocols, as the sensor allows for completely integrated real-time capture.

Secondly, this dissertation presented a new, marker free method for optically measuring neural activity. The real-time nature of these types of sensors has now enabled, for the first time, a method for measuring the intrinsic neural activity of an organism *in vivo*. Using relatively simple optics consisting of only an immersion microscope lens and optical tubing, the sensor was able to detect a significant change in the reflected polarization when two stimulant odors of hexanol and octanol were introduced to a locust. This represents a potential new method of neural capture that does not require damaging electrodes or potentially toxic fluorophores.

References/Bibliography/Works Cited

[1] B. E. Bayer, *Color imaging array*, vol. US3971065. Eastman Kodak Company, 1976.

[2] V. Gruev, R. Perkins, and T. York, "CCD polarization imaging sensor with aluminum nanowire optical filters," *Opt Express*, vol. 18, no. 18, pp. 19087–19094, Aug. 2010.

[3] J. Nakamura, Ed., *Image Sensors and Signal Processing for Digital Still Cameras*. CRC Press, 2006.

[4] E. R. Fossum, "CMOS image sensors: electronic camera-on-a-chip," *Electron Devices IEEE Trans. On*, vol. 44, no. 10, pp. 1689–1698, 1997.

[5] A. El Gamal and H. Eltoukhy, "CMOS image sensors," *Circuits Devices Mag. IEEE*, vol. 21, no. 3, pp. 6–20, 2005.

[6] R. M. Philipp, D. Orr, V. Gruev, J. Van der Spiegel, and R. Etienne-Cummings, "Linear Current-Mode Active Pixel Sensor," *Solid-State Circuits IEEE J. Of*, vol. 42, no. 11, pp. 2482–2491, Nov. 2007.

[7] G. P. Nordin, J. T. Meier, P. C. Deguzman, and M. W. Jones, "Micropolarizer array for infrared imaging polarimetry," *J. Opt. Soc. Am. A*, vol. 16, no. 5, pp. 1168–1174, 1999.

[8] T. Tokuda, H. Yamada, K. Sasagawa, and J. Ohta, "Polarization-Analyzing CMOS Image Sensor With Monolithically Embedded Polarizer for Microchemistry Systems," *Biomed. Circuits Syst. IEEE Trans. On*, vol. 3, no. 5, pp. 259–266, 2009.

[9] P. J. W. Noble, "Self-scanned silicon image detector arrays," *Electron Devices IEEE Trans. On*, vol. 15, no. 4, pp. 202–209, Apr. 1968.

[10] J. Ahn, K. Lee, Y. Kim, H. Jeong, B. Kim, H. Kim, J. Park, T. Jung, W. Park, T. Lee, E. Park, S. Choi, G. Choi, H. Park, Y. Choi, S. Lee, Y. Kim, Y. J. Jung, D. Park, S. Nah, Y. Oh, M. Kim, Y. Lee, Y. Chung, I. Hisanori, J. Im, D. K. J. Lee, B. Yim, G. Lee, H. Kown, S. Choi, J. Lee, D. Jang, Y. Kim, T. C. Kim, G. Hiroshige, C.-Y. Choi, D. Lee, and G. Han, "7.1 A 1/4-inch 8Mpixel CMOS image sensor with 3D backside-illuminated 1.12 #x03BC;m pixel with front-side deep-trench isolation and vertical transfer gate," in *Solid-State Circuits Conference Digest of Technical Papers (ISSCC), 2014 IEEE International*, 2014, pp. 124–125.

[11] T. York, S. B. Powell, S. Gao, L. Kahan, T. Charanya, D. Saha, N. W. Roberts, T. W. Cronin, J. Marshall, S. Achilefu, S. P. Lake, B. Raman, and V. Gruev, "Bioinspired Polarization Imaging Sensors: From Circuits and Optics to Signal Processing Algorithms and Biomedical Applications," *Proc. IEEE*, vol. 102, no. 10, pp. 1450–1469, Oct. 2014. © 2014 IEEE. Reprinted, with permission

[12] V. Gruev and R. Etienne-Cummings, "Implementation of steerable spatiotemporal image filters on the focal plane," *Circuits Syst. II Analog Digit. Signal Process. IEEE Trans. On*, vol. 49, no. 4, pp. 233–244, Apr. 2002.

[13] V. Gruev, J. Van der Spiegel, and N. Engheta, "Dual-tier thin film polymer polarization imaging sensor," *Opt. Express*, vol. 18, no. 18, pp. 19292–19303, 2010.

[14] V. Gruev, Z. Yang, J. Van der Spiegel, and R. Etienne-Cummings, "Current mode image sensor with two transistors per pixel," *Circuits Syst. Regul. Pap. IEEE Trans. On*, vol. 57, no. 6, pp. 1154–1165, 2010.

[15] E. R. Fossum and D. B. Hondongwa, "A Review of the Pinned Photodiode for CCD and CMOS Image Sensors," *Electron Devices Soc. IEEE J. Of*, vol. 2, no. 3, pp. 33–43, May 2014.

[16] H. Tian, B. Fowler, and A. Gamal, “Analysis of temporal noise in CMOS photodiode active pixel sensor,” *Solid-State Circuits IEEE J. Of*, vol. 36, no. 1, pp. 92–101, Jan. 2001.
[17] G. G. Stokes, “On The Composition and Resolution of Streams of Polarized Light from different Sources,” *Trans. Camb. Philos. Soc.*, vol. 9, 1852.
[18] H. Mueller, “The Foundation of Optics,” *J. Opt. Soc. Am.*, vol. 38, no. 7, p. 661, 1948.
[19] R. Schwind, “Polarization vision in water insects and insects living on a moist substrate,” *J. Comp. Physiol. A*, vol. 169, no. 5, pp. 531–540, 1991.
[20] F. Lebhardt, J. Koch, and B. Ronacher, “The polarization compass dominates over idiothetic cues in path integration of desert ants,” *J. Exp. Biol.*, vol. 215, no. 3, pp. 526–535, 2012.
[21] C. Evangelista, P. Kraft, M. Dacke, T. Labhart, and M. V. Srinivasan, “Honeybee navigation: critically examining the role of the polarization compass,” *Philos. Trans. R. Soc. B Biol. Sci.*, vol. 369, no. 1636, 2014.
[22] R. Muheim, J. B. Phillips, and S. Ã…kesson, “Polarized Light Cues Underlie Compass Calibration in Migratory Songbirds,” *Science*, vol. 313, no. 5788, pp. 837–839, 2006.
[23] R. Muheim, J. B. Phillips, and M. E. Deutschlander, “White-throated sparrows calibrate their magnetic compass by polarized light cues during both autumn and spring migration,” *J. Exp. Biol.*, vol. 212, no. 21, pp. 3466–3472, 2009.
[24] Y. Liu, T. York, W. Akers, G. Sudlow, V. Gruev, and S. Achilefu, “Complementary fluorescence-polarization microscopy using division-of-focal-plane polarization imaging sensor,” *J. Biomed. Opt.*, vol. 17, no. 11, pp. 116001–116001, 2012.
[25] H. H. Thoen, M. J. How, T.-H. Chiou, and J. Marshall, “A Different Form of Color Vision in Mantis Shrimp,” *Science*, vol. 343, no. 6169, pp. 411–413, 2014.
[26] C. A. Mead and M. A. Mahowald, “A silicon model of early visual processing,” *Neural Netw.*, vol. 1, no. 1, pp. 91–97, 1988.
[27] E. Culurciello, R. Etienne-Cummings, and K. A. Boahen, “A biomorphic digital image sensor,” *Solid-State Circuits IEEE J. Of*, vol. 38, no. 2, pp. 281–294, 2003.
[28] P. Lichtsteiner, C. Posch, and T. Delbruck, “A 128 $\times$ 128 120 dB 15 µs Latency Asynchronous Temporal Contrast Vision Sensor,” *Solid-State Circuits IEEE J. Of*, vol. 43, no. 2, pp. 566–576, Feb. 2008.
[29] C. Posch, D. Matolin, and R. Wohlgenannt, “A QVGA 143 dB Dynamic Range Frame-Free PWM Image Sensor With Lossless Pixel-Level Video Compression and Time-Domain CDS,” *Solid-State Circuits IEEE J. Of*, vol. 46, no. 1, pp. 259–275, 2011.
[30] R. Berner and T. Delbruck, “Event-based color change pixel in standard CMOS,” in *Circuits and Systems (ISCAS), Proceedings of 2010 IEEE International Symposium on*, 2010, pp. 349–352.
[31] J. A. Leero-Bardallo, D. H. Bryn, and P. Hafliger, “Bio-inspired asynchronous pixel event tri-color vision sensor,” in *Biomedical Circuits and Systems Conference (BioCAS), 2011 IEEE*, 2011, pp. 253–256.
[32] Y. M. Song, Y. Xie, V. Malyarchuk, J. Xiao, I. Jung, K.-J. Choi, Z. Liu, H. Park, C. Lu, R.-H. Kim, R. Li, K. B. Crozier, Y. Huang, and J. A. Rogers, “Digital cameras with designs inspired by the arthropod eye,” *Nature*, vol. 497, no. 7447, pp. 95–99, 2013.
[33] D. Drazen, P. Lichtsteiner, P. HÃ¤fliger, T. DelbrÃ¼ck, and A. Jensen, “Toward real-time particle tracking using an event-based dynamic vision sensor,” *Exp. Fluids*, vol. 51, no. 5, pp. 1465–1469, 2011.

[34] J. S. Tyo, D. L. Goldstein, D. B. Chenault, and J. A. Shaw, “Review of passive imaging polarimetry for remote sensing applications,” *Appl Opt*, vol. 45, no. 22, pp. 5453–5469, 2006.
[35] H. Cong Phuoc, A. Robles-Kelly, and E. Hancock, “Shape and refractive index recovery from single-view polarisation images,” in *Computer Vision and Pattern Recognition (CVPR), 2010 IEEE Conference on*, 2010, pp. 1229–1236.
[36] S. Shwartz, E. Namer, and Y. Y. Schechner, “Blind Haze Separation,” in *Computer Vision and Pattern Recognition, 2006 IEEE Computer Society Conference on*, 2006, vol. 2, pp. 1984–1991.
[37] J. Reckfort, H. Wiese, M. Dohmen, D. GrÃ¤ssel, U. Pietrzyk, K. Zilles, K. Amunts, and M. Axer, “Extracting the inclination angle of nerve fibers within the human brain with 3D-PLI independent of system properties,” in *Proc. of SPIE*, 2013, vol. 8873, p. 88730F–88730F–10.
[38] D. Chenault, J. Foster, J. Pezzaniti, J. Harchanko, T. Aycock, and A. Clark, “Polarimetric sensor systems for airborne ISR,” in *Proc. of SPIE*, 2014, vol. 9076, p. 90760K–90760K–9.
[39] W. Stürzl and N. Carey, “A Fisheye Camera System for Polarisation Detection on UAVs,” in *Computer Vision – ECCV 2012. Workshops and Demonstrations*, vol. 7584, A. Fusiello, V. Murino, and R. Cucchiara, Eds. Springer Berlin Heidelberg, 2012, pp. 431–440.
[40] J. L. Pezzaniti, D. Chenault, K. Gurton, and M. Felton, “Detection of obscured targets with IR polarimetric imaging,” in *Proc. of SPIE*, 2014, vol. 9072, p. 90721D–90721D–12.
[41] K. J. Voss and N. Souaidia, “POLRADS: polarization radiance distribution measurement system,” *Opt. Express*, vol. 18, no. 19, pp. 19672–19680, 2010.
[42] L. B. Wolff, T. A. Mancini, P. Pouliquen, and A. G. Andreou, “Liquid crystal polarization camera,” *Robot. Autom. IEEE Trans. On*, vol. 13, no. 2, pp. 195–203, 1997.
[43] A. G. Andreou and Z. K. Kalayjian, “Polarization imaging: principles and integrated polarimeters,” *Sens. J. IEEE*, vol. 2, no. 6, pp. 566–576, 2002.
[44] V. Gruev, J. Van der Spiegel, and N. Engheta, “Image sensor with focal plane polarization sensitivity,” in *Circuits and Systems, 2008. ISCAS 2008. IEEE International Symposium on*, 2008, pp. 1028–1031.
[45] G. Myhre, W.-L. Hsu, A. Peinado, C. LaCasse, N. Brock, R. A. Chipman, and S. Pau, “Liquid crystal polymer full-stokes division of focal plane polarimeter,” *Opt. Express*, vol. 20, no. 25, pp. 27393–27409, 2012.
[46] W.-L. Hsu, G. Myhre, K. Balakrishnan, N. Brock, M. Ibn-Elhaj, and S. Pau, “Full-Stokes imaging polarimeter using an array of elliptical polarizer,” *Opt. Express*, vol. 22, no. 3, pp. 3063–3074, 2014.
[47] S. B. Powell and V. Gruev, “Underwater polarization camera for real-time and high definition imaging,” in *Proc. of SPIE*, 2014, vol. 9099.
[48] N. Shashar, C. Milbury, and R. Hanlon, “Polarization Vision in Cephalopods: Neuroanatomical and Behavioral Features that Illustrate Aspects of Form and Function,” *Mar. Freshw. Behav. Physiol.*, vol. 35, no. 1–2, pp. 57–68, 2002.
[49] M. Momeni and A. H. Titus, “An analog VLSI chip emulating polarization vision of octopus retina,” *Neural Netw. IEEE Trans. On*, vol. 17, no. 1, pp. 222–232, 2006.

[50] X. Wu, Z. Xiaojin, A. Bermak, and F. Boussaid, “An AER based CMOS polarization image sensor with photo-aligned micropolarizer array,” in *Quality Electronic Design, 2009. ASQED 2009. 1st Asia Symposium on*, 2009, pp. 126–130.
[51] N. J. Marshall, M. F. Land, C. A. King, and T. W. Cronin, “The Compound Eyes of Mantis Shrimps (Crustacea, Hoplocarida, Stomatopoda). I. Compound Eye Structure: The Detection of Polarized Light,” *Philos. Trans. R. Soc. Lond. B. Biol. Sci.*, vol. 334, no. 1269, pp. 33–56, 1991.
[52] V. Gruev, “Fabrication of a dual-layer aluminum nanowires polarization filter array,” *Opt. Express*, vol. 19, no. 24, pp. 24361–24369, 2011.
[53] J. J. Wang, F. Walters, X. Liu, P. Sciortino, and X. Deng, “High-performance, large area, deep ultraviolet to infrared polarizers based on 40 nm line/78 nm space nanowire grids,” *Appl. Phys. Lett.*, vol. 90, no. 6, p. -, 2007.
[54] Y. Zhao, M. A. Belkin, and A. Alù, “Twisted optical metamaterials for planarized ultrathin broadband circular polarizers,” *Nat. Commun.*, vol. 3, p. 870, May 2012.
[55] J. J. Peltzer, P. D. Flammer, T. E. Furtak, R. T. Collins, and R. E. Hollingsworth, “Ultra-high extinction ratio micropolarizers using plasmonic lenses,” *Opt. Express*, vol. 19, no. 19, pp. 18072–18079, 2011.
[56] A. S. Sedra, “The current conveyor: history and progress,” in *Circuits and Systems, 1989., IEEE International Symposium on*, 1989, pp. 1567–1571 vol.3.
[57] T. Fang and A. Bermak, “Low-power and high-speed current-mode CMOS imager with 1T biasing scheme,” in *Sensors, 2010 IEEE*, 2010, pp. 1653–1656.
[58] R. Njuguna and V. Gruev, “Current-Mode CMOS Imaging Sensor With Velocity Saturation Mode of Operation and Feedback Mechanism,” *Sens. J. IEEE*, vol. 14, no. 3, pp. 710–721, 2014.
[59] S. B. Powell and V. Gruev, “Calibration methods for division-of-focal-plane polarimeters,” *Opt Express*, vol. 21, no. 18, pp. 21039–21055, Sep. 2013.
[60] T. York and V. Gruev, “Characterization of a visible spectrum division-of-focal-plane polarimeter,” *Appl. Opt.*, vol. 51, no. 22, pp. 5392–5400, 2012. This chapter was published in Applied Optics and is made available with the permission of OSA. The paper can be found at the following URL on the OSA website: http://www.opticsinfobase.org/ao/abstract.cfm?URI=ao-51-22-5392. Systematic or multiple reproduction or distribution to multiple locations via electronic or other means is prohibited and is subject to penalties under law.
[61] E. Salomatina-Motts, V. Neel, and A. Yaroslavskaya, “Multimodal polarization system for imaging skin cancer,” *Opt. Spectrosc.*, vol. 107, no. 6, pp. 884–890, 2009.
[62] M. Anastasiadou, A. D. Martino, D. Clement, F. Liége, B. Laude-Boulesteix, N. Quang, J. Dreyfuss, B. Huynh, A. Nazac, L. Schwartz, and H. Cohen, “Polarimetric imaging for the diagnosis of cervical cancer,” *Phys Status Solidi C*, vol. 5, no. 5, pp. 1423–1426, 2008.
[63] T. V. T. Krishna, C. D. Creusere, and D. G. Voelz, “Passive Polarimetric Imagery-Based Material Classification Robust to Illumination Source Position and Viewpoint,” *Image Process. IEEE Trans. On*, vol. 20, no. 1, pp. 288 –292, Jan. 2011.
[64] H. Chen and L. B. Wolff, “Polarization Phase-Based Method For Material Classification In Computer Vision,” *Int. J. Comput. Vis.*, vol. 28, no. 1, pp. 73–83, 1998.
[65] M. Sarkar, D. San Segundo Bello, C. van Hoof, and A. Theuwissen, “Integrated Polarization Analyzing CMOS Image Sensor for Material Classification,” *Sens. J. IEEE*, vol. 11, no. 8, pp. 1692 –1703, Aug. 2011.

[66] S.-S. Lin, K. M. Yemelyanov, J. Edward N. Pugh, and N. Engheta, "Polarization-based and specular-reflection-based noncontact latent fingerprint imaging and lifting," *J Opt Soc Am A*, vol. 23, no. 9, pp. 2137–2153, 2006.
[67] D. Miyazaki, R. T. Tan, K. Hara, and K. Ikeuchi, "Polarization-based inverse rendering from a single view," *Comput. Vis. 2003 Proc. Ninth IEEE Int. Conf. On*, pp. 982 –987 vol.2, Oct. 2003.
[68] D. Goldstein, *Polarized Light*, 3rd ed. CRC Press, 2011.
[69] J. L. Pezzaniti, D. Chenault, M. Roche, J. Reinhardt, J. P. Pezzaniti, and H. Schultz, "Four camera complete Stokes imaging polarimeter," in *Polarization: Measurement, Analysis, and Remote Sensing VIII*, Orlando, FL, USA, 2008, vol. 6972, p. 69720J.
[70] J. L. Pezzaniti and D. B. Chenault, "A division of aperture MWIR imaging polarimeter," in *Polarization Science and Remote Sensing II*, San Diego, CA, USA, 2005, vol. 5888, p. 58880V.
[71] P. Bhandari, K. J. Voss, and L. Logan, "An instrument to measure the downwelling polarized radiance distribution in the ocean," *Opt Express*, vol. 19, no. 18, pp. 17609–17620, Aug. 2011.
[72] T. Tokuda, S. Sato, H. Yamada, K. Sasagawa, and J. Ohta, "Polarisation-analysing CMOS photosensor with monolithically embedded wire grid polariser," *Electron. Lett.*, vol. 45, no. 4, pp. 228 –230, Feb. 2009.
[73] Z. Xiaojin, F. Boussaid, A. Bermak, and V. G. Chigrinov, "Thin Photo-Patterned Micropolarizer Array for CMOS Image Sensors," *Photonics Technol. Lett. IEEE*, vol. 21, no. 12, pp. 805–807, 2009.
[74] S. Shishido, T. Noda, K. Sasagawa, T. Tokuda, and J. Ohta, "Polarization Analyzing Image Sensor with On-Chip Metal Wire Grid Polarizer in 65-nm Standard Complementary Metal Oxide Semiconductor Process," *Jpn. J. Appl. Phys.*, vol. 50, no. 4, p. 04DL01, 2011.
[75] D. A. Miller, D. W. Wilson, and E. L. Dereniak, "Novel design and alignment of wire-grid diffraction gratings on a visible focal plane array," *Opt. Eng.*, vol. 51, no. 1, p. 014001, 2012.
[76] J. S. Tyo, C. F. LaCasse, and B. M. Ratliff, "Total elimination of sampling errors in polarization imagery obtained with integrated microgrid polarimeters," *Opt. Lett.*, vol. 34, no. 20, pp. 3187–3189, 2009.
[77] B. M. Ratliff, C. F. LaCasse, and J. S. Tyo, "Interpolation strategies for reducing IFOV artifacts in microgrid polarimeter imagery," *Opt. Express*, vol. 17, no. 11, pp. 9112–9125, 2009.
[78] S. Gao and V. Gruev, "Bilinear and bicubic interpolation methods for division of focal plane polarimeters," *Opt. Express*, vol. 19, no. 27, pp. 26161–26173, 2011.
[79] S. Gao and V. Gruev, "Gradient-based interpolation method for division-of-focal-plane polarimeters," *Opt. Express*, vol. 21, no. 1, pp. 1137–1151, 2013.
[80] T. York and V. Gruev, "Calibration method for division of focal plane polarimeters in the optical and near-infrared regime," in *Infrared Technology and Applications XXXVII*, Orlando, Florida, USA, 2011, vol. 8012, p. 80120H.
[81] D. L. Bowers, J. K. Boger, L. D. Wellems, S. E. Ortega, M. P. Fetrow, J. E. Hubbs, W. T. Black, B. M. Ratliff, and J. S. Tyo, "Unpolarized calibration and nonuniformity correction for long-wave infrared microgrid imaging polarimeters," *Opt. Eng.*, vol. 47, no. 4, p. 046403, 2008.

[82] T. York, L. Kahan, S. P. Lake, and V. Gruev, “Real-time high-resolution measurement of collagen alignment in dynamically loaded soft tissue,” *J. Biomed. Opt.*, vol. 19, no. 6, pp. 066011–066011, 2014.
[83] D. L. Butler, S. A. Goldstein, and F. Guilak, “Functional Tissue Engineering: The Role of Biomechanics,” *J. Biomech. Eng.*, vol. 122, no. 6, pp. 570–575, Jul. 2000.
[84] D. L. Butler, S. A. Goldstein, R. E. Guldberg, X. E. Guo, R. Kamm, C. T. Laurencin, L. V. McIntire, V. C. Mow, R. M. Nerem, R. L. Sah, L. J. Soslowsky, R. L. Spilker, and R. T. Tranquillo, “The impact of biomechanics in tissue engineering and regenerative medicine,” *Tissue Eng. Part B Rev.*, vol. 15, no. 4, pp. 477–484, 2009.
[85] Y. Fung, *Biomechanics: mechanical properties of living tissues*, 2nd ed. Springer-Verlag, New York, 1993.
[86] J. D. Humphrey, “Review Paper: Continuum biomechanics of soft biological tissues,” *Proc. R. Soc. Lond. Ser. Math. Phys. Eng. Sci.*, vol. 459, no. 2029, pp. 3–46, 2003.
[87] J. P. Dickey, B. R. Hewlett, G. A. Dumas, and D. A. Bednar, “Measuring Collagen Fiber Orientation: A Two-Dimensional Quantitative Macroscopic Technique,” *J. Biomech. Eng.*, vol. 120, no. 4, pp. 537–540, Aug. 1998.
[88] S. Thomopoulos, G. R. Williams, J. A. Gimbel, M. Favata, and L. J. Soslowsky, “Variation of biomechanical, structural, and compositional properties along the tendon to bone insertion site,” *J. Orthop. Res.*, vol. 21, no. 3, pp. 413–419, 2003.
[89] S. P. Lake, K. S. Miller, D. M. Elliott, and L. J. Soslowsky, “Effect of fiber distribution and realignment on the nonlinear and inhomogeneous mechanical properties of human supraspinatus tendon under longitudinal tensile loading,” *J. Orthop. Res.*, vol. 27, no. 12, pp. 1596–1602, 2009.
[90] T. Tower, M. Neidert, and R. Tranquillo, “Fiber Alignment Imaging During Mechanical Testing of Soft Tissues,” *Ann. Biomed. Eng.*, vol. 30, no. 10, pp. 1221–1233, 2002.
[91] K. P. Quinn and B. A. Winkelstein, “Altered collagen fiber kinematics define the onset of localized ligament damage during loading,” *J. Appl. Physiol.*, vol. 105, no. 6, pp. 1881–1888, 2008.
[92] S. Lake and V. Barocas, “Mechanical and Structural Contribution of Non-Fibrillar Matrix in Uniaxial Tension: A Collagen-Agarose Co-Gel Model,” *Ann. Biomed. Eng.*, vol. 39, no. 7, pp. 1891–1903, 2011.
[93] X. Xu, M. Kulkarni, A. Nehorai, and V. Gruev, “A correlation-based interpolation algorithm for division-of-focal-plane polarization sensors,” 2012, vol. 8364, p. 83640L–83640L–8.
[94] M. Scanziani and M. Hausser, “Electrophysiology in the age of light,” *Nature*, vol. 461, no. 7266, pp. 930–939, 2009.
[95] B. E. Cohen, “Biological imaging: Beyond fluorescence,” *Nature*, vol. 467, no. 7314, pp. 407–408, 2010.
[96] L. B. Cohen, B. Hille, and R. D. Keynes, “Light scattering and birefringence changes during activity in the electric organ of Electrophorus electricus,” *J. Physiol.*, vol. 203, no. 2, pp. 489–509, 1969.
[97] R. Stepnoski, A. LaPorta, F. Raccuia-Behling, G. Blonder, R. Slusher, and D. Kleinfeld, “Noninvasive detection of changes in membrane potential in cultured neurons by light scattering,” *Proc. Natl. Acad. Sci.*, vol. 88, no. 21, pp. 9382–9386, 1991.

[98] K. M. Carter, J. S. George, and D. M. Rector, “Simultaneous birefringence and scattered light measurements reveal anatomical features in isolated crustacean nerve,” *J. Neurosci. Methods*, vol. 135, no. 1, pp. 9–16, 2004.
[99] J. L. Schei, M. D. McCluskey, A. J. Foust, X.-C. Yao, and D. M. Rector, “Action potential propagation imaged with high temporal resolution near-infrared video microscopy and polarized light,” *Neuroimage*, vol. 40, no. 3, pp. 1034–1043, 2008.
[100] R.-W. Lu, Q.-X. Zhang, and X.-C. Yao, “Circular polarization intrinsic optical signal recording of stimulus-evoked neural activity,” *Opt. Lett.*, vol. 36, no. 10, pp. 1866–1868, 2011.
[101] D. Kleinfeld and A. LaPorta, “Detection of action potentials in vitro by changes in refractive index,” *Light Scatt. Imaging Neural Tissue Funct. Humana Press Totowa N. J.*, 2003.
[102] X. Wang and L. V. Wang, “Propagation of polarized light in birefringent turbid media: A Monte Carlo study,” *J. Biomed. Opt.*, vol. 7, no. 3, pp. 279–290, 2002.
[103] T. York, V. Gruev, D. Saha, and B. Raman, “A 220 #x00D7; 128 120 mW 60 frames/s current mode polarization imager for in vivo optical neural recording,” in *Circuits and Systems (ISCAS), 2014 IEEE International Symposium on*, 2014, pp. 1849–1852.
[104] D. Saha, K. Leong, N. Katta, and B. Raman, “Multi-unit Recording Methods to Characterize Neural Activity in the Locust (Schistocerca Americana) Olfactory Circuits,” *J. Vis. Exp.*, no. 71, p. e50139, 2013.

.

Appendix

A.1. Extended Data from Polarization Measurements

A.1.1 Data from 460 nm LED Incident Light

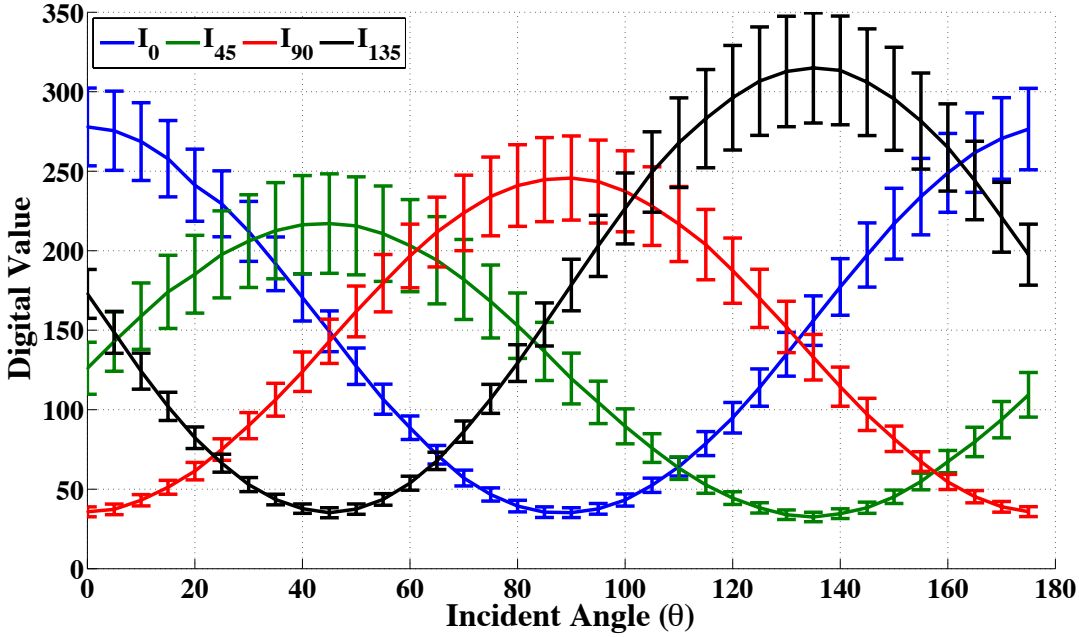

Figure A1.1.1 Data measured from rotating polarizer at 460nm LED board input, 3.4V, 0.25A, averaged across the array (bars indicate spatial standard deviation)

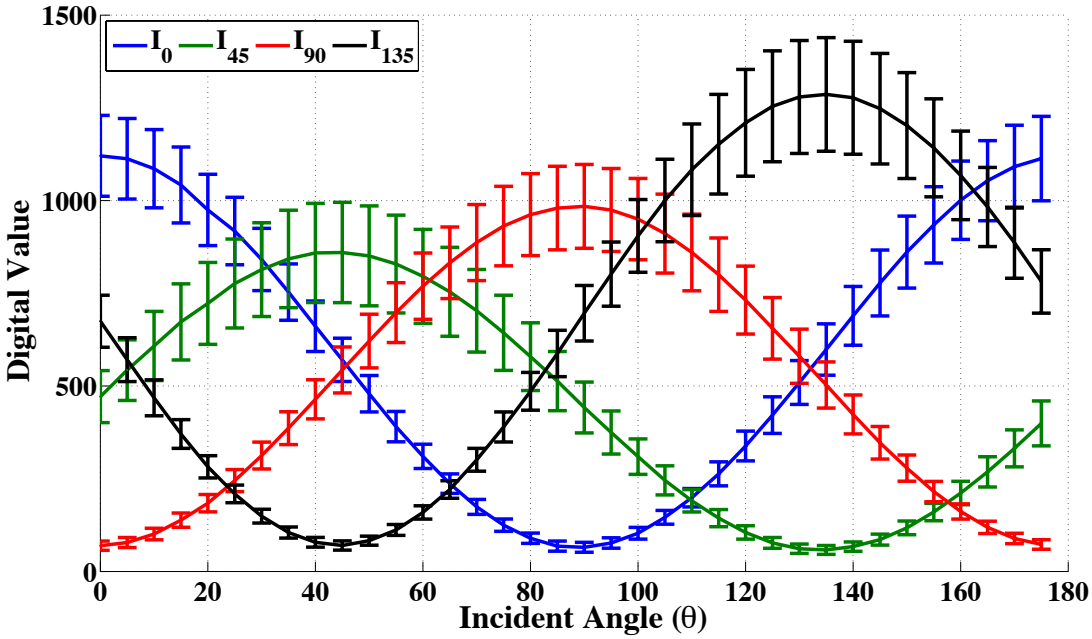

Figure A1.1.2. Data measured from rotating polarizer at 460nm LED board input, 3.4V, 1.25A, averaged across the array (bars indicate spatial standard deviation)

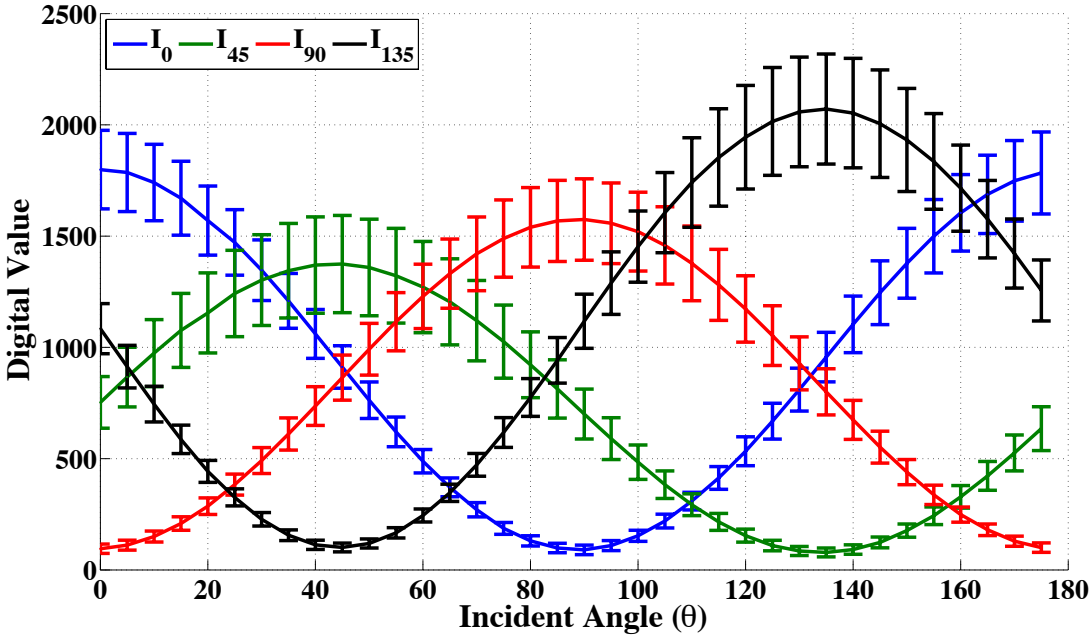

Figure A1.1.3. Data measured from rotating polarizer at 460nm LED board input, 3.4V, 2.25A, averaged across the array (bars indicate spatial standard deviation)

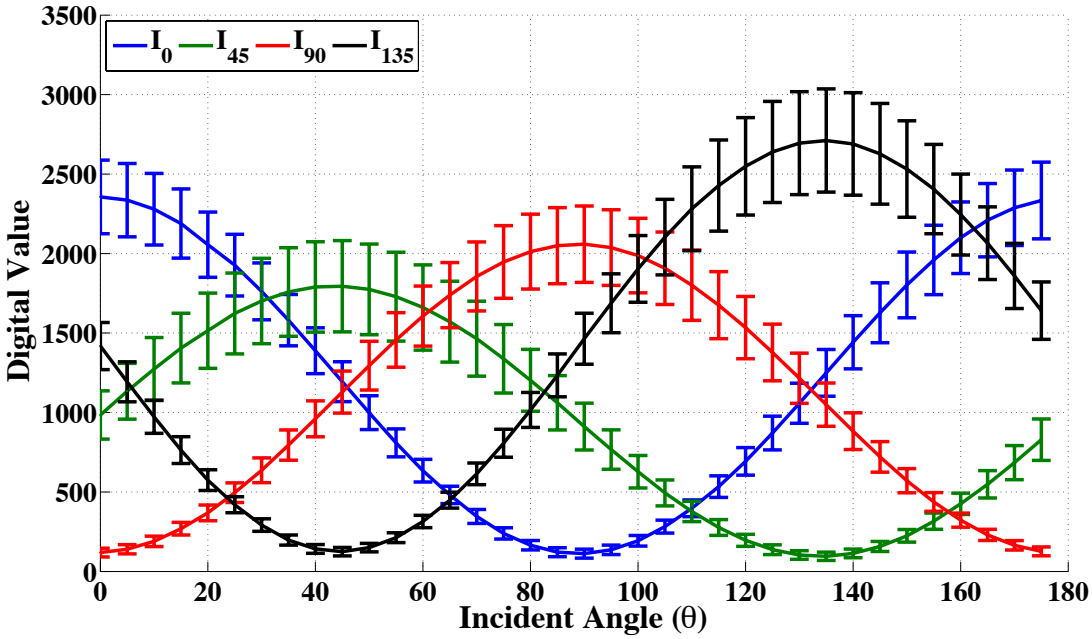

Figure A1.1.4. Data measured from rotating polarizer at 460nm LED board input, 3.4V, 3.25A, averaged across the array (bars indicate spatial standard deviation)

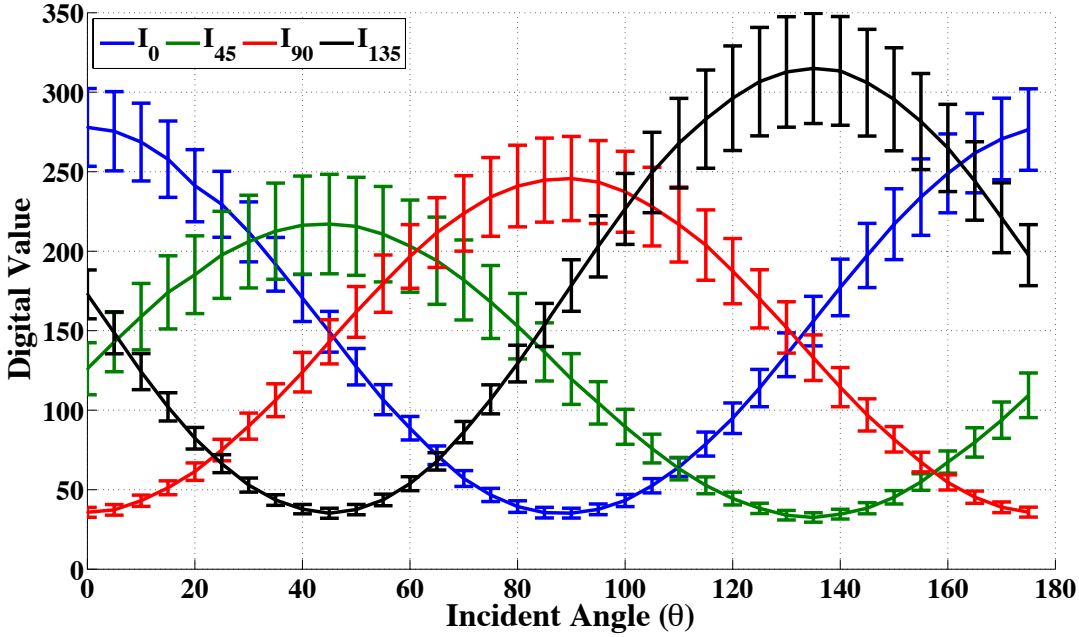

Figure A1.1.5 Data measured from rotating polarizer at 460nm LED board input, 3.4V, 4.25A, averaged across the array (bars indicate spatial standard deviation)

Figures A1.1.1-5 show the average value across the pixel array for a rotating polarizer at varying LED intensities for a nominal LED wavelength of 460nm. The error bars are the spatial

standard deviation across the array. The filter response shows consistency with Malus' Law for rotating polarizers.

A.1.2 Data from 515nm LED Incident Light

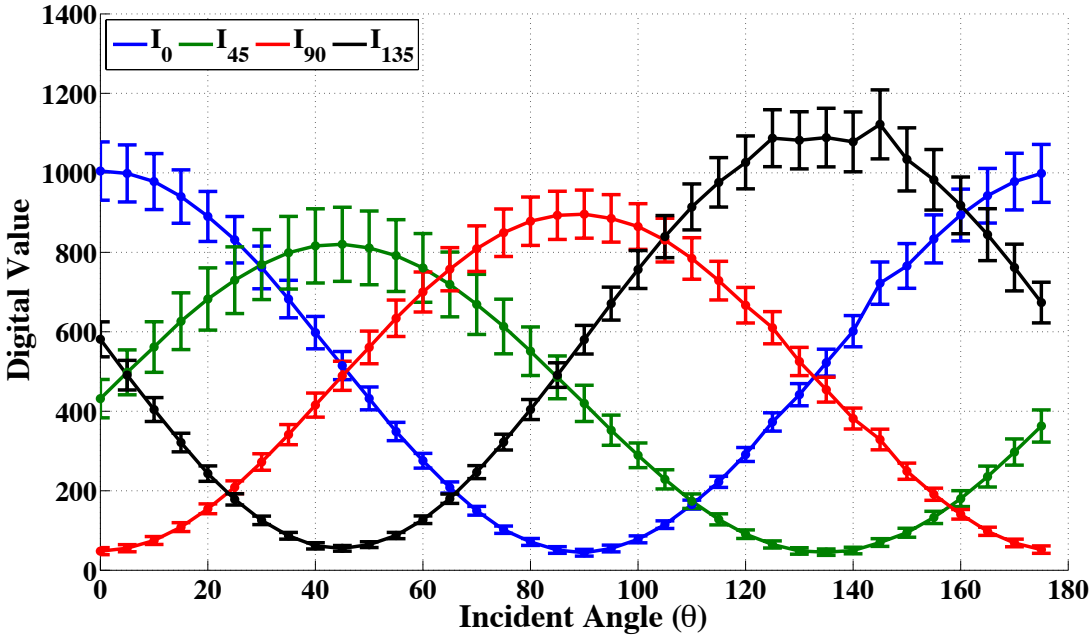

Figure A1.2.1. Data measured from rotating polarizer at 515nm LED board input, 3.4V, 1.0A, averaged across the array (bars indicate spatial standard deviation)

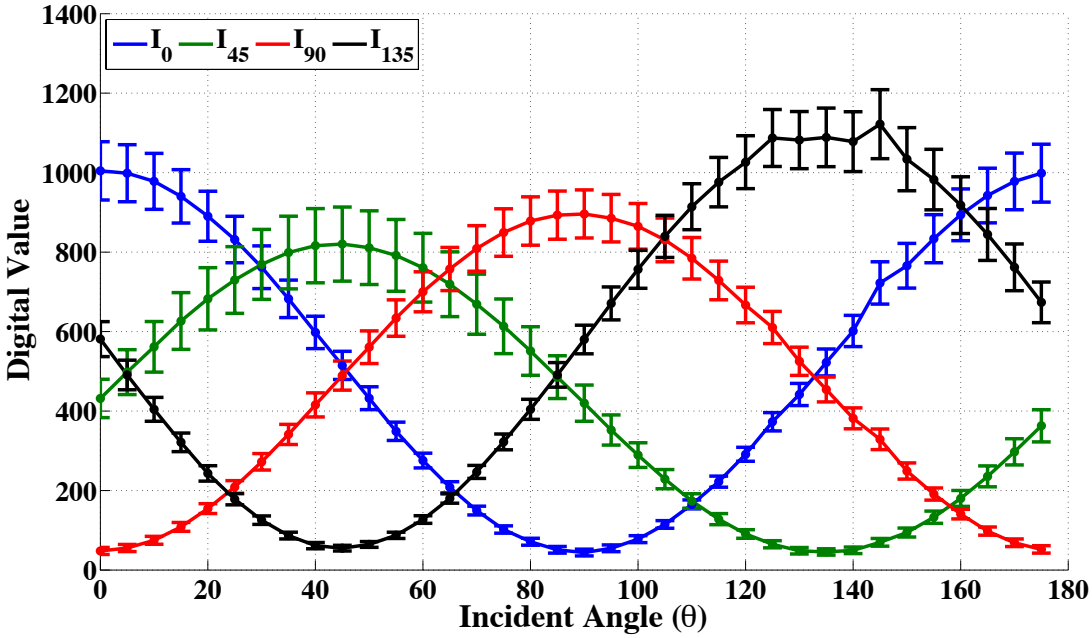

Figure A1.2.2. Data measured from rotating polarizer at 515nm LED board input, 3.4V, 2.0A, averaged across the array (bars indicate spatial standard deviation)

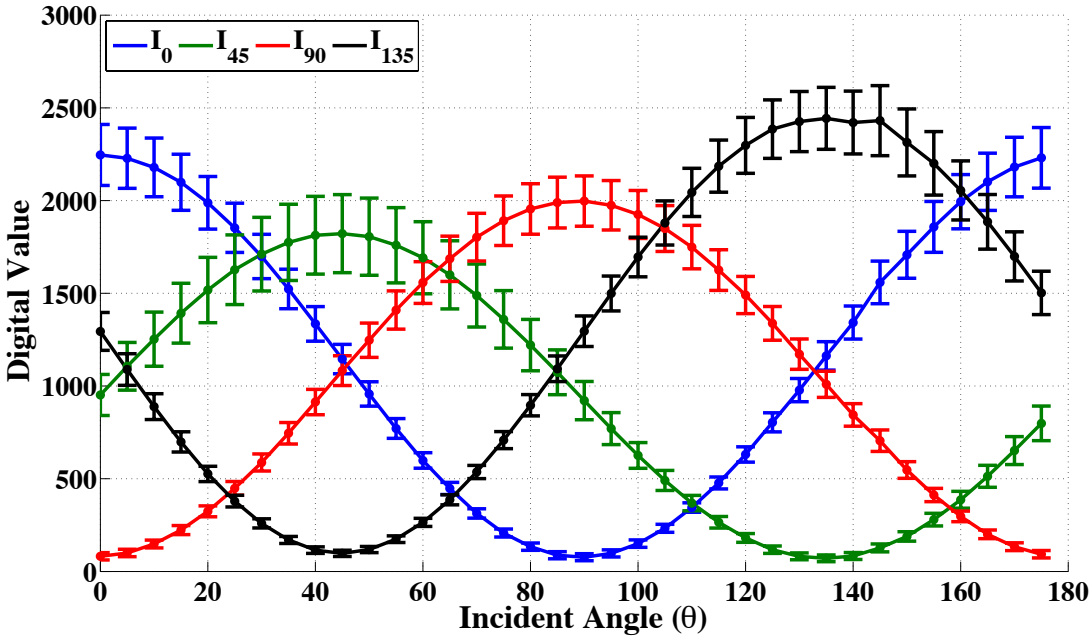

Figure A1.2.3. Data measured from rotating polarizer at 515nm LED board input, 3.4V, 3.0A, averaged across the array (bars indicate spatial standard deviation)

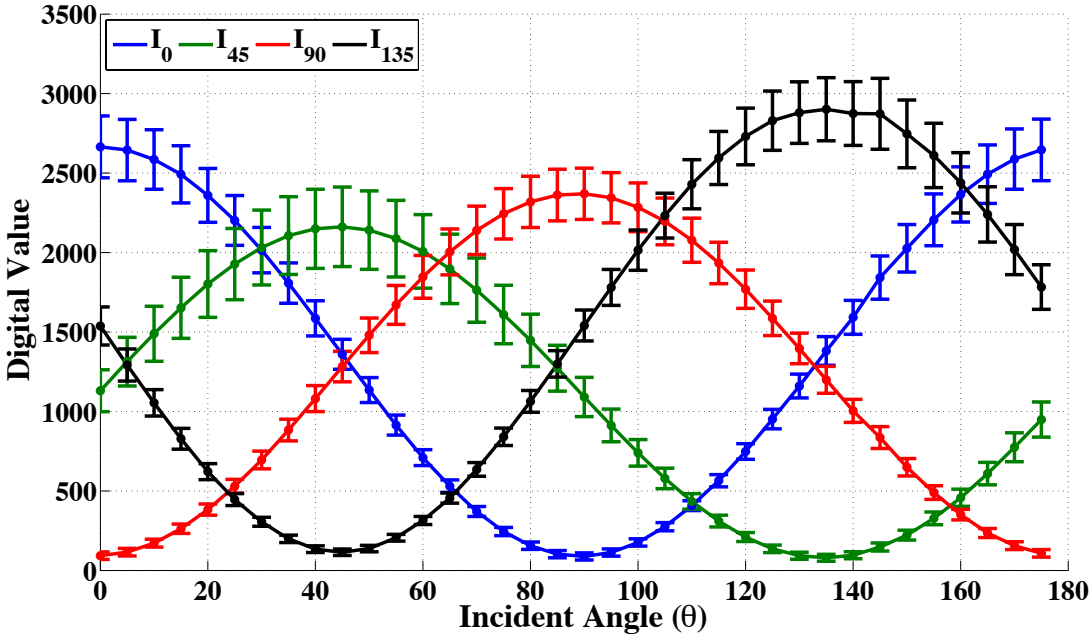

Figure A1.2.4. Data measured from rotating polarizer at 515nm LED board input, 3.4V, 4.0A, averaged across the array (bars indicate spatial standard deviation)

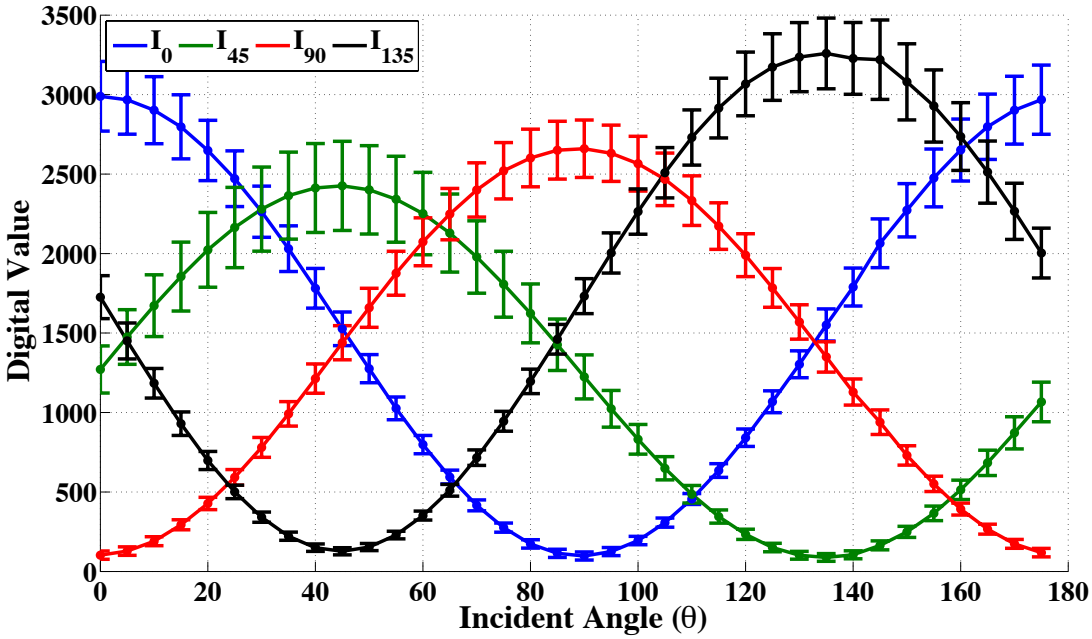

Figure A1.2.5. Data measured from rotating polarizer at 515nm LED board input, 3.4V, 5.0A, averaged across the array (bars indicate spatial standard deviation)

Figures A1.2.1-5 show the average value across the pixel array for a rotating polarizer at varying LED intensities for a nominal LED wavelength of 515nm. The error bars are the spatial standard deviation across the array. The filter response shows consistency with Malus' Law for rotating polarizers.

A.1.3 Data from 625nm LED Incident Light

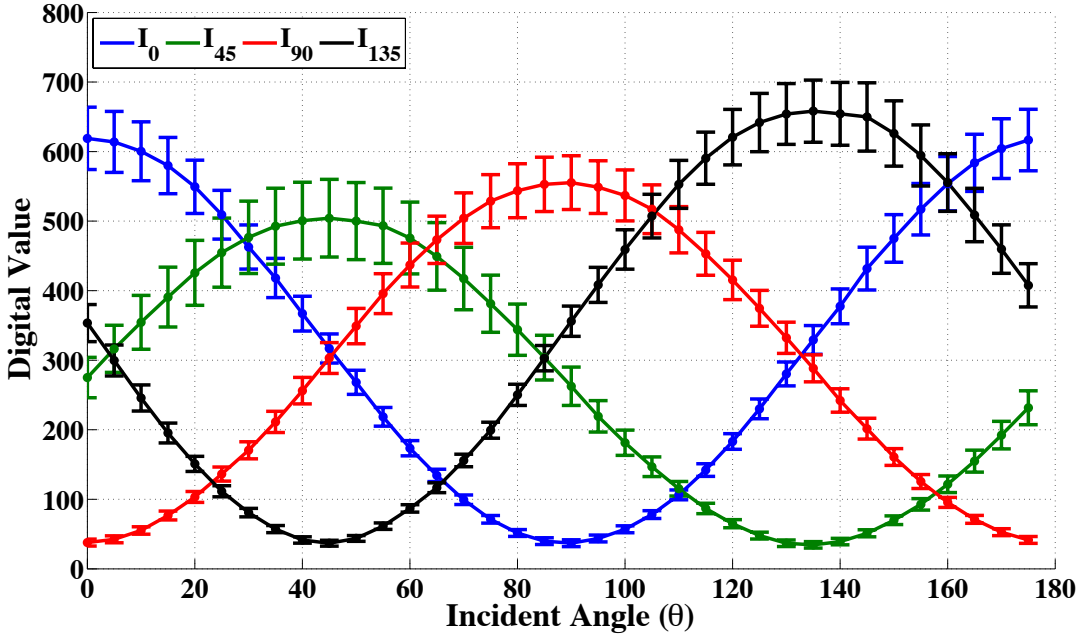

Figure A1.3.1. Data measured from rotating polarizer at 625nm LED board input, 2.3V, 1.0A, averaged across the array (bars indicate spatial standard deviation)

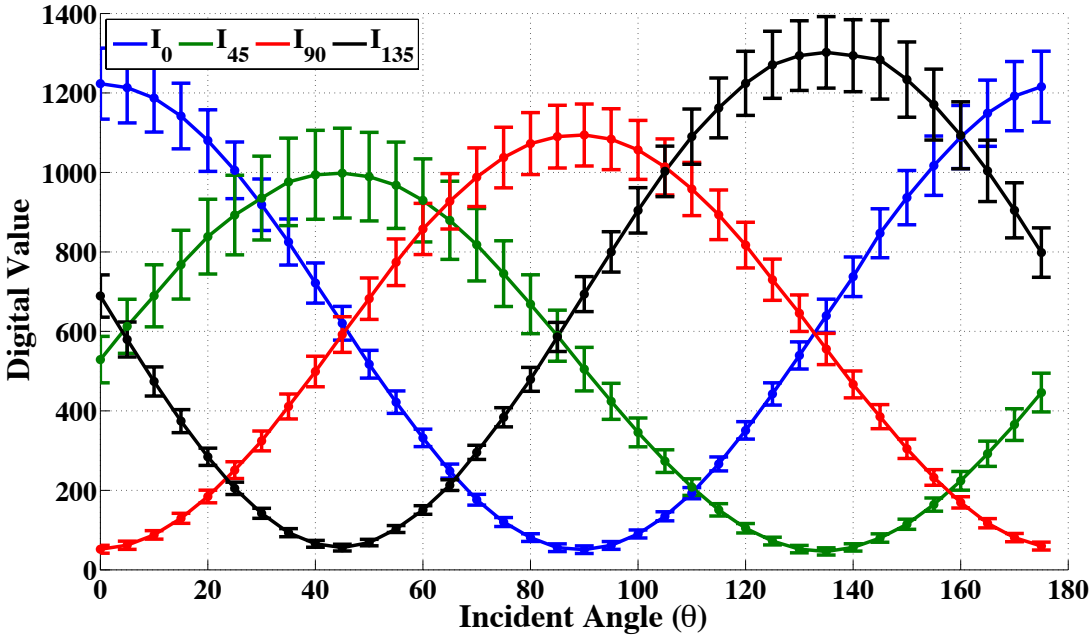

Figure A1.3.2. Data measured from rotating polarizer at 625nm LED board input, 2.3V, 2.0A, averaged across the array (bars indicate spatial standard deviation)

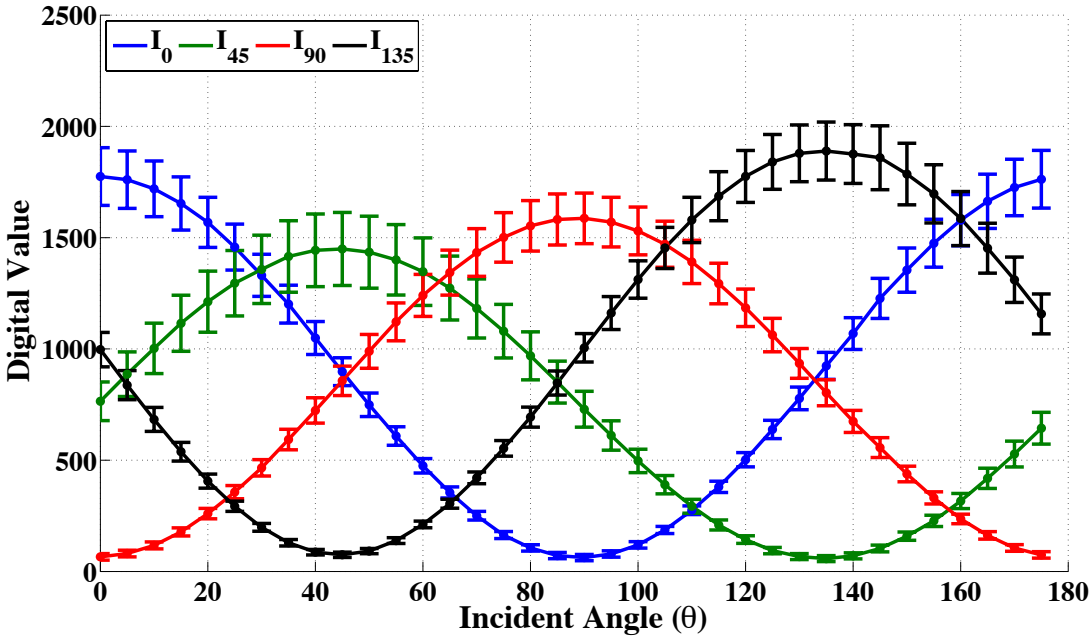

Figure A1.3.3. Data measured from rotating polarizer at 625nm LED board input, 2.3V, 3.0A, averaged across the array (bars indicate spatial standard deviation)

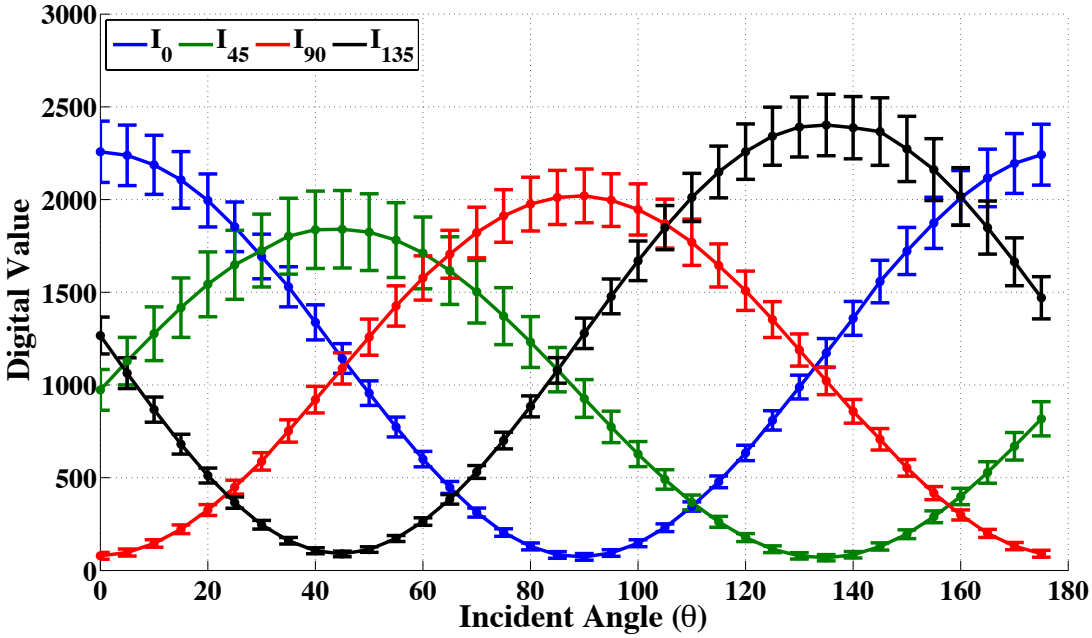

Figure A1.3.4. Data measured from rotating polarizer at 625nm LED board input, 2.3V, 4.0A, averaged across the array (bars indicate spatial standard deviation)

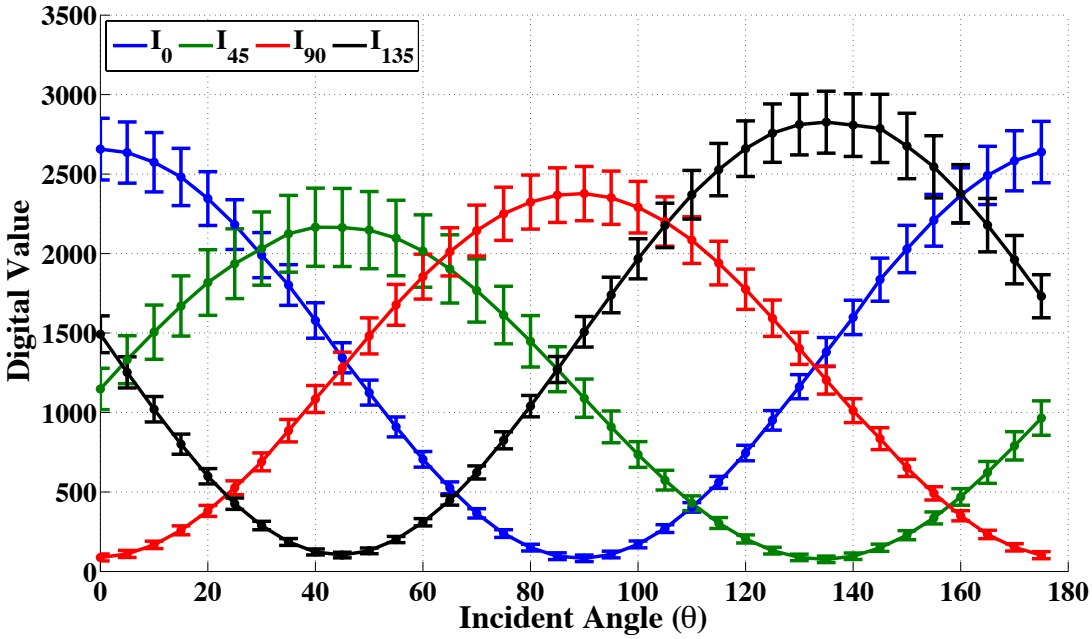

Figure A1.3.5. Data measured from rotating polarizer at 625nm LED board input, 2.3V, 5.0A, averaged across the array (bars indicate spatial standard deviation)

Figures A1.3.1-5 show the average value across the pixel array for a rotating polarizer at varying LED intensities for a nominal LED wavelength of 625nm. The error bars are the spatial standard deviation across the array. The filter response shows consistency with Malus' Law for rotating polarizers.